



Acquisition Directorate

Research & Development Center

UAS Characterization of Oil in Ice

Volume I: Laboratory Results

Distribution Statement A: Approved for public release; distribution is unlimited.

February 2022



Homeland Security

NOTICE

This document is disseminated under the sponsorship of the Department of Homeland Security in the interest of information exchange.

For use outside the United States Government, the Government assumes no liability for its contents or use thereof.

The United States Government does not endorse products or manufacturers. Trade or manufacturers' names appear herein solely because they are considered essential to the objective of this report.



Mr. Al Arsenault
Technical Director
United States Coast Guard
Research & Development Center
1 Chelsea Street
New London, CT 06320



UAS Characterization of Oil in Ice – Volume I: Laboratory Results

Technical Report Documentation Page

1. Report No.		2. Government Accession Number		3. Recipient's Catalog No.	
4. Title and Subtitle UAS Characterization of Oil in Ice – Volume I: Laboratory Results				5. Report Date February 2022	
				6. Performing Organization Code Project No. 4711	
7. Author(s) Oscar Garcia-Pineda, Alexander Balsley, Lisa DiPinto, Nancy Kinner and Paul Panetta				8. Performing Report No. RDC UDI #1910	
9. Performing Organization Name and Address U.S. Coast Guard Research and Development Center 1 Chelsea Street New London, CT 06320		NOAA Office of Response & Restoration 1305 East West Hwy Building 4 Silver Spring, MD 20910		10. Work Unit No. (TRAIS)	
				11. Contract or Grant No. 70Z0FT20KPE2N0100	
12. Sponsoring Organization Name and Address COMMANDANT (CG-MER) US COAST GUARD STOP 7516 2703 MARTIN LUTHER KING JR AVE SE WASHINGTON, DC 20593				13. Type of Report & Period Covered Final	
				14. Sponsoring Agency Code Commandant (CG-MER) US Coast Guard Stop 7516 Washington, DC 20593	
15. Supplementary Notes The R&D Center's technical point of contact is Mr. Alexander Balsley, 860-865-0474, email: Alexander.Balsley@uscg.mil					
16. Abstract (MAXIMUM 200 WORDS) The U.S. Coast Guard Research and Development Center and the National Oceanic and Atmospheric Administration executed an experiment on remote sensing of fresh (non-emulsified) and emulsified oil in ice at the Cold Regions Research and Engineering Laboratory. Multispectral sensors mounted on an Unmanned Aircraft System (UAS) identified different levels of oil thickness and differentiated between emulsified and non-emulsified oil under simulated Arctic conditions. Non-linear thermal imagery was able to segment and classify areas of ice cover. A multispectral sensor differentiated emulsions between 10 µm and 50 µm. Apparent temperature measurements could be converted to oil thickness over the range of 50 µm to 5,000 µm using a logarithmic function. The minimum detection limit of the thermal sensor for the oil was between 50 µm and 100 µm. Acoustic sensors on a remotely operated vehicle (ROV) were shown to perform well with measuring thicker oil slicks (greater than 1,000 µm). The experiments provide a foundation for further research to implement a processing routine that can be applied to field operations to detect ice cover and oil thicknesses under different environmental conditions and ice densities.					
17. Key Words Multispectral, Arctic, emulsion, thermal, oil, ice, thickness, unmanned aircraft system, remotely operated vehicle, acoustic, remote sensing, sensor, data processing, imagery			18. Distribution Statement Distribution Statement A: Approved for public release; distribution is unlimited.		
19. Security Class (This Report) UNCLAS//Public		20. Security Class (This Page) UNCLAS//Public		21. No of Pages 90	22. Price



(This page intentionally left blank.)



EXECUTIVE SUMMARY

The U.S. Coast Guard Research and Development Center (USCG RDC) and the National Oceanic and Atmospheric Administration (NOAA) executed an experiment on remote sensing of oil in ice at the United States Army Corps of Engineers Geophysical Research Facility (GRF) of the Cold Regions Research and Engineering Laboratory (CRREL) in Hanover, New Hampshire. Multispectral sensors mounted on an Unmanned Aircraft System (UAS) identified different levels of oil thickness and differentiated between fresh (non-emulsified) and emulsified oil under simulated Arctic conditions. A 0.3 m (1 ft) layer of ice, formed in the Geophysical Research Facility tank (18.2 m (60 ft) x 6.7 m (22 ft) x 2.1 m (7 ft)), had twelve 1m x 1m (3.3ft x 3.3ft) holes cut into it. These holes were filled with different amounts of smaller, broken ice pieces and different thicknesses of non-emulsified or emulsified Alaska North Slope (ANS) oil. The experiment consisted of a series of UAS flights in which remote sensing data was collected by the multispectral and thermal sensors onboard the aircraft. RDC and NOAA carried out additional experiments to compare synchronous observations from the UAS and below-the-water-level acoustic sensor mounted on an ROV.

The experiments showed that visual, infrared, and multispectral imagery can be used to discern between clean ice and ice covered by oil. Non-linear thermal imagery can be used to segment and classify areas of ice cover. When oil thickness was between 10 μm and 50 μm , the multispectral sensor began to differentiate between emulsified and non-emulsified oil. For an oil thickness range of 50 μm to 5,000 μm , one can use apparent temperature measurements to determine oil thickness using a logarithmic function. The minimum detection limit of the thermal sensor for the oil was between 50 μm and 100 μm .

The CRREL experiments provide a foundation for further research to implement a processing routine that can be applied to field operations to detect ice cover and oil thicknesses under different environmental conditions and ice densities. FOSCs will be equipped with future protocols to assess the recovery of oil in a spill. The findings will be applicable not only for UAS platforms, but for any platform capable of holding these sensors (higher altitude airplanes, satellites). Deploying a large UAS with all the integrated sensors was possible at CRREL, however, performing these types of operations in the field could be challenging with the current UAS technology. Volume II of this report contains supplemental laboratory data that includes imageries and other raw data that the project team collected to serve as potential resources for future research work.

Future research, including USCG RDC-planned experiments in the Great Lakes and Alaska, may determine: UAS requirements needed to withstand and operate in Arctic conditions; how multi-spectral imaging detects different types of oil products; streamlined calibration protocols, workflow, and data processing; easy-to-interpret work products for the Federal On-Scene Coordinator; and uncertainty bounds for oil thickness.



(This page intentionally left blank.)



TABLE OF CONTENTS

EXECUTIVE SUMMARY v

LIST OF FIGURES ix

LIST OF TABLES xii

LIST OF ACRONYMS, ABBREVIATIONS, AND SYMBOLS..... xiii

1 INTRODUCTION..... 1

1.1 State-of-the-Art Oil Spill Remote Sensing..... 2

1.1.1 Current Sensors for Oil Spill Response Operations..... 2

1.2 Remote Sensing of Oil in Arctic Conditions..... 9

1.3 Project Design 9

1.4 Equipment and Working Area Configuration 11

1.5 Effect of Daily Temperature and Illumination of Sensor Operation..... 15

1.6 Physical Thickness Measurements: Tube Sampling 16

1.7 Acoustic Sensors 18

2 EXPERIMENTAL DESIGN 19

3 RESULTS AND DISCUSSION 23

3.1 Multispectral and Thermal Imagery 23

3.1.1 Multispectral Differentiation of Non-Emulsified Oil and Emulsified Oil..... 23

3.1.2 Thermal Analysis of the Oil Thickness 27

3.1.3 24-Hour Time Lapse of Multispectral and Thermal Imagery..... 38

3.1.4 Synchronous and Comparison of Observations from Aerial (UAS) and Underwater (ROV).. 42

3.2 Minimum Detection Limit 45

3.2.1 Minimum Detection Limit of Oil in Cold Waters without Ice 46

3.2.2 Minimum Detection Limit of Oil in Cold Waters with Ice 46

3.3 Algorithms for Oil Thickness Detection 49

3.3.1 Algorithms for Oil Thickness in Cold Water without Ice..... 49

3.3.2 Algorithms for Oil Thickness in Cold Water with Ice..... 49

3.4 Ice Cover Adjustment Effect on Oil Thickness and Volume Estimates 53

3.5 Workflow and Data Processing to Obtain Oil Thickness 59

3.6 Methods for Calculating Oil Thickness in Ice Infested Waters 60

3.6.1 Method 1. Using *In Situ* Physical Measurements of Oil Thickness 61

3.6.2 Method 2. Using Totes Containing Known Oil Thicknesses 65

3.6.3 Comparing Methods 1 and 2..... 68

4 CONCLUSIONS..... 68

4.1 Differences between Analyzing Oil Thickness in Temperate and Arctic Waters..... 69

4.2 Use of UAS for Arctic Oil Spill Response..... 71

5 RECOMMENDATIONS..... 72

5 REFERENCES CITED 73



(This page intentionally left blank.)



LIST OF FIGURES

Figure 1. Oil thickness classifications.	3
Figure 2. Controlled experiments for oil thickness determination using multispectral and thermal sensors. ..	5
Figure 3. USF oil tank experiment set up. a) Multi-band cameras and a thermal camera mounted on a tripod frame to collect images of the oil-on-water in the two tanks. (b) and (c) are two identical tanks filled with Tampa Bay water, where the same volume of b) crude oil and c) emulsified oil are put on the water surface using syringes.	5
Figure 4. Synchronous thermal and visual imagery of floating oil from the Santa Barbara seep sites. The left and right panels are thermal image and synoptic photograph, respectively, of the same area.	6
Figure 5. Multispectral classification of oil.	8
Figure 6. Ground view of the GRF tank with ice squares (1m x 1m) and black plastic totes for oil thickness calibration.	10
Figure 7. Target thicknesses of each tote for reference of spectral and thermal reflectance.	10
Figure 8. Left: Screens displaying the thermal and visual data in real time from the UAS. Right: Control base station that monitored the telemetry of the UAS.	11
Figure 9. UAS aircraft used for the experiment.	11
Figure 10. Sensors mounted on the landing gear of the UAS.	12
Figure 11. Close up for each of the squares with corresponding ice cover before oil was added to the squares.	13
Figure 12. Adding controlled amounts of oil into squares to produce established thickness layers.	13
Figure 13. Aerial view of the tank setup before oil was added to the squares.	14
Figure 14. Setup for time-lapse study. Left: A-Frame with cameras; Right: setup of the totes with different thicknesses and oil types.	15
Figure 15. View from the top of the A-Frame for the daily temperature and illumination effect experiments.	16
Figure 16. Tube sampler measuring oil thickness.	16
Figure 17. Processing the tube samples for oil thickness.	17
Figure 18. Example of sample processing for the tube sampler with emulsified (50/50) oil at 50 μm	18
Figure 19. Oil Line: 98, 76, 90, 96 pixels with an average of 90 pixels. Line Thickness: 791 μm . Reference: 512 pixels (4,500 μm).	18
Figure 20. Example raw data from independent channels (475 nm, 560 nm, 668 nm, 717 nm, and 840 nm) wavelength for the multispectral.	20
Figure 21. Example predetermined algorithms using the multispectral sensor data.	21
Figure 22. Ground level photographs taken when Flight 2 was occurring.	22
Figure 23. Emulsified vs non-emulsified oil detection using multispectral sensors (500 μm thickness, 75% ice cover).	24
Figure 24. Emulsified and non-emulsified oil (500 μm , 75% ice cover).	25
Figure 25. Emulsified vs. non-emulsified oil (200 μm , 75% ice cover).	26
Figure 26. Emulsified vs non-emulsified oil (100 μm , 50% ice cover).	27
Figure 27. Aerial view of the GRF tank with the 1m x 1m squares with 10 μm of oil and different amounts of ice and the totes with different thicknesses of oil.	28
Figure 28. Non-linear bi-color thermal imaging showing apparent temperature of squares with increasing amounts of ice percent cover. Left and right columns are emulsified and non-emulsified oil, respectively.	30



LIST OF FIGURES (Continued)

Figure 29. Visual vs. non-linear bi-color thermal images taken at 13.7 m (45 ft) (200 μm thickness, 0-5% ice cover). Apparent temperatures for non-emulsified oil..... 31

Figure 30. Comparison of visual vs. thermal images on higher quantities of oil. 32

Figure 31. These measurements show the maximum (red triangle), minimum (blue triangle), and average of the apparent temperatures inside the totes (Boxes 1 through 9). 33

Figure 32. Comparison of maximum, minimum, and average of apparent temperature observations for the totes vs. oil thickness during Flight 4 at 8:34am under overcast skies and limited solar radiation. 34

Figure 33. Apparent temperature change vs oil thickness for Flight 7 at 11:34am under overcast skies, but with more solar radiation. 35

Figure 34. Thermal view of the highest contrast in apparent temperature between the 2,000 μm thick oil and ice for Flight 9 during sun exposure. 36

Figure 35. Analysis of apparent oil temperatures from non-emulsified oil vs emulsified oil. Early morning flight at 07:45am. 37

Figure 36. Example of difference in imagery obtained from the visual versus thermal sensors. The top photo is a visual RGB image in which little can be discerned much about the variation in oil thickness as opposed to the apparent temperature data in the bottom image. 39

Figure 37. Thermal readings from the 24-hour time lapse of oil thicknesses for the totes. Each point is the average of apparent temperature readings every 15 minutes. 40

Figure 38. Apparent temperature readings of non-emulsified oil over a 24-hour time lapse. 41

Figure 39. Apparent temperature of non-emulsified vs 50:50 oil-water vs 30:70 oil-water emulsion..... 42

Figure 40. The upper right square was used for comparison of synchronous data collected by the UAS and ROV. This square corresponds to 5% ice cover with 2 L of oil on it. 43

Figure 41. Statistics from the thermal data including the frequency of sheen thicknesses for the test square. 43

Figure 42. ROV-based acoustic measurements of the thickness of oil in 5% ice covered square with target thickness of 2,000 μm. 44

Figure 43. Comparison of the acoustic sensor thickness estimates and Water Mapping’s tube sampler for a range of oil thicknesses. 45

Figure 44. Aerial view from the squares set with 50 μm of oil. 46

Figure 45. Thermal contrast detected when oil thickness reached 100 μm. 47

Figure 46. Multispectral analysis of 10 μm of oil. There was no detection of change at this level. 48

Figure 47. Multispectral analysis of 50 μm of oil..... 48

Figure 48. Higher magnification of the 25% ice cover using multispectral image of 50 μm emulsified oil. 49

Figure 49. Apparent temperature variability due to ice cover. 50

Figure 50. Oil distribution on squares during Flight 8 with 1,000 μm of emulsified (left) and non-emulsified (right) columns of oil for each panel..... 51

Figure 51. Apparent temperatures derived from thermal images of squares containing 1,000 mL of emulsified (left) and non-emulsified (right) oil with different ice cover from Flight 8. 52

Figure 52. Apparent temperature vs. oil thickness using Flight 8 data and the oil totes of known thickness.53

Figure 53. Linear temperature of the ice and oiled surface in the GRF tank. Totes with no ice show much warmer than 1m x 1m squares with oil and ice. 54

Figure 54. Ice pixels converted to zero, the yellow square shows the 1m x 1m cell with 25% ice cover and 1,000 μm. 54



LIST OF FIGURES (Continued)

Figure 55. Apparent temperatures inside each pixel in the 1m x 1m square with 25% ice cover and 1,000 μm . The right panel is a magnified image of the light blue square on the left panel to show the apparent temperature values. 55

Figure 56. The volume of oil per thermal image pixel (m^3). The right panel is a magnified image of the light blue square on the left panel to show the apparent temperature values..... 56

Figure 57. Estimated thickness of oil per pixel; maximum thickness calculated was 2,157 μm . The right panel is a magnified image of the light blue square on the left panel to show the apparent temperature values. 57

Figure 58. Adjusted thicknesses (μm) per pixel on a 1m x 1m square using the actual 16% ice coverage. Histogram inset in shows the frequency distribution of the oil thicknesses. 58

Figure 59. Cells with 50% and 75% of ice cover where ice melted to 39% and 63%, respectively. 59

Figure 60. Top view from the multispectral imaging of a 1m x 1m square while the project team collected physical measurements of multiple thicknesses. 61

Figure 61. 1m x 1m square with 1,000 μm of oil on ice and 50% ice cover. 62

Figure 62. Pixels on the thermal image that have been converted to thickness values. 63

Figure 63. Oil thickness (color scale in micrometers) inside the iced square..... 64

Figure 64. Physical measurement of oil thickness for the oil/ice thickness algorithm..... 65

Figure 65. Thermal image over a 1m x 1m square with 1,000 mL of oil. Non-emulsified oil with layers of thicknesses of 100 μm , 200 μm , 500 μm , 1,000 μm , and 5,000 μm (respectively from left to right)..... 66

Figure 66. Apparent temperature change vs thickness. 67

Figure 67. Calculated oil thicknesses from adjusted values of apparent temperatures. 67

Figure 68. Ohmsett (left) vs. CRREL (right) experimental conditions. 70



LIST OF TABLES

Table 1. Five levels of oil appearances 3
Table 2. Sensors used to detect oil on water and ice. 9
Table 3. Test conditions at CRREL. 14
Table 4. Combination of a target oil type (emulsified [ratio], non-emulsified) and oil thickness monitored in the 1m x 1m squares, using the tube samplers..... 17
Table 5. UAS flights made during CRREL experiments..... 19
Table 6. Comparison of acoustic and thermal sensor thickness estimates for 2,000 μm and 5% ice..... 44
Table 7. Comparison of the acoustic sensor thickness estimates and Water Mapping’s tube sampler for a range of oil thicknesses..... 45



LIST OF ACRONYMS, ABBREVIATIONS, AND SYMBOLS

ADAC	Arctic Domain Awareness Center
ANS	Alaska North Slope crude
ARA	Applied Research Associates
ATI	Apparent Thermal Inertia
AUV	Autonomous Underwater Vehicle
AVHPR	Advanced Very High-Resolution Radiometer
AVIRIS	Airborne Visual Infrared Imaging Spectrometer
BSEE	Bureau of Safety and Environmental Enforcement
COP	Common operating picture
COTS	Commercial Off-the-Shelf
CRREL	Cold Regions Research and Engineering Laboratory
DWH	Deepwater Horizon
DIVER	Data Integration and Visualization Exploration and Reporting
EPA	Environmental Protection Agency
ERMA	Environmental Response Management Application
FLIR	Forward Looking Infrared
FOSC	Federal On-Scene Coordinator
GNOME	General NOAA Operational Modeling Environment
GOM	Gulf of Mexico
GRF	Geophysical Research Facility
IR	Infrared
L	Liter
LIDAR	Light Detection and Ranging
LWIR	Long-Wave Infrared
m	Meter
µm	Micrometer
mL	Milliliter
mm	Millimeter
MC20	Taylor Energy/Mississippi Canyon 20
MODIS	Moderate Resolution Imaging Spectroradiometer
MWIR	Mid-Infrared
NASA	National Aeronautics and Space Administration
NIR	Near infrared
nm	Nanometer
NOAA	National Oceanic and Atmospheric Administration
Ohmsett	Oil and Hazardous Materials Simulated Environmental Test Tank
OWOIIA	Open Water Oil Identification Job Aid for Aerial Observation
QA	Quality Assurance
RGB	Red, Green, Blue
RDC	Research and Development Center
ROV	Remotely Operated Vehicle



LIST OF ACRONYMS, ABBREVIATIONS, AND SYMBOLS (Continued)

SAR	Synthetic Aperture Radar
SSC	Scientific Support Coordinator
SWIR	Shot-Wave Infrared
TI	Thermal Inertia
TVOC	Total Volatile Organic Compounds
UAS	Unmanned Aircraft System
UV	Ultraviolet
USCG	United States Coast Guard
USF	University of South Florida
USGS	U.S. Geological Survey
VOCs	Volatile Organic Compounds
VTOL	Vertical Takeoff and Landing
WHOI	Woods Hole Oceanographic Institute
WM	Water Mapping, LLC



The scientific results and conclusions, as well as any views or opinions expressed herein, are those of the author(s) and do not necessarily reflect the views of NOAA or the Department of Commerce.



(This page intentionally left blank.)



1 INTRODUCTION

Responding to an oil spill is challenging in any coastal or offshore environment. However, responses in ice infested waters present even greater challenges for oil detection, fate and transport modeling, and environmental characterization, all of which are necessary to support operational response decisions made by Federal On-Scene Coordinators (FOSCs). In this context, there are estimated 30 billion barrels of undiscovered oil in the U.S. Arctic, most of it under the Chukchi and Beaufort Seas (National Research Council, 2016). At the same time, activities such as oil exploration and production, as well as maritime shipping are increasing in the Arctic region. Surface and subsurface oil releases (e.g., pipeline incidents) occasionally occur in ice infested waters, requiring Federal and State Agencies to implement timely responses for source abatement and cleanup, in the interest of minimizing resource impacts. The National Oceanic and Atmospheric Administration (NOAA) provides scientific support to the United States Coast Guard (USCG), including developing and advancing technologies that would help the agencies to be better prepared in the case of an oil spill emergency.

NOAA, the Bureau of Safety and Environmental Enforcement (BSEE), Woods Hole Oceanographic Institution (WHOI), the Environmental Protection Agency (EPA), and Water Mapping, LLC (WM) carried out research in coordination with the USCG Director of Emergency Management (CG-5RI) and others that resulted in improved characterization of floating non-emulsified oil and emulsions using remote sensing techniques for response and damage assessment operations. Specifically, researchers paired Unmanned Aircraft System (UAS) remote sensing with simultaneous *in situ* field measurements for oil slick thickness and water column concentration to calibrate and verify the remote sensing data products. A variety of evolving sampling tools, remote sensing platforms and sensor packages (e.g., satellite, fixed wing aircraft, UAS, Autonomous Underwater Vehicles (AUVs), Remotely Operated Vehicles (ROVs)) have synoptically sampled and characterized floating oil and the associated water column conditions in the northern Gulf of Mexico and the oil seep area near Santa Barbara, CA. Foundational work continues to advance the agencies' ability to conduct oil spill detection and surveillance in response to oil spills in temperate waters, but without the complications of ice and cold temperatures. The USCG Research and Development Center (RDC), in collaboration with NOAA's Office of Response and Restoration (ORR), which provides scientific support to the USCG for incident responses, recognized the lack of similar research and surveillance capabilities in ice-infested waters.

This project was established to evaluate the ability of existing technology, tested in temperate waters, to perform in ice-infested water. The objective was to develop methods to more efficiently and effectively detect and characterize surface oil in cold seawater environments during and following incidents to inform decisions about the effectiveness of surface and subsurface response actions. NOAA created workflows to allow for transfer of data and related information products into common operating platforms (COPs) such as NOAA's Environmental Response Management Application (ERMA), managed through systems such as the Data Integration and Visualization Exploration and Reporting (DIVER) and for use in commonly used fate and trajectory models such as the General NOAA Operational Modeling Environment (GNOME).

The project team executed controlled experiments in collaboration with the U.S. Army Corps of Engineers at the Cold Regions Research and Engineering Laboratory (CRREL) in Hanover, NH. The team evaluated the effect of temperature and percent cover on the efficacy of oil (non-emulsified or emulsified) detection by a suite of passive and active UAS sensors in a broken ice environment. The team also determined workflow



and standard operating procedures (Image Processing Algorithms) for the UAS and sensors for oil detection in ice infested waters advancing capabilities for rapid data product development.

Building on findings from CRREL, the project team will execute field trials that would expand the capabilities of spill responders to use remote sensing tools to direct assets in the more complex and challenging arctic environments.

1.1 State-of-the-Art Oil Spill Remote Sensing

The science of monitoring oil spills using remote sensing has been well established for more than a decade. The processes by which oil is detected by passive or active sensors, which is mainly dependent on the physical properties of hydrocarbons, is well-understood. In recent years, new technology (e.g., UAS) has changed how oil spills are monitored. While the fundamental scientific concepts of remote sensing of oil spills are the same, the technology to apply them has improved, leading to significant new possibilities for refined detection.

During the Deepwater Horizon (DWH) oil spill in 2010, the vast majority of the monitoring was based on satellite remote sensing. At that time, after a satellite image was acquired, it often took one to two days to make the data available to the spill response community. Once the images were available, interpretation of the data was often debated and challenged, requiring several days for a consensus to be reached on the detection and interpretation of oil in the image. This time delay became and continued to be a crucial issue when using remote sensing as a response tool. Since then, research by USCG, BSEE, NOAA, multiple partners from other agencies, and the private sector, improved remote sensing technology so that it can provide real and near-real time support for the accurate detection of oil spills.

Technological highlights from recent years include the advancement of platforms/sensing technology and the development of efficient workflows for data integration. For example, responders have used UAS in oil spill response operations since 2015. Drones are used for detection, mapping, tactical response, and assessment of oil spills at real and near-real timescales. UAS can augment information from larger platforms including high-altitude airplanes and satellites. As an example, during an oil spill experiment funded by BSEE in 2017, a product derived from a Synthetic Aperture Radar (SAR) satellite image (map of the detected spill) was delivered to a response vessel within 41 minutes after the satellite acquired it. UAS-detected targets were used to calibrate the satellite product (Garcia-Pineda et al., 2019). The number of satellites available for oil spill monitoring has increased at least one order of magnitude over the last few years. As a result, there are many platforms that stand to benefit from improved workflows. A workflow is a review of the imagery collected along with additional data (e.g., weather conditions).

1.1.1 Current Sensors for Oil Spill Response Operations

There are three types of sensors likely to be used for remote sensing during Arctic oil spill response: 1) visual high resolution (optical), 2) thermal (infrared), and 3) multispectral (Garcia-Pineda, 2019). There are other sensors that may detect oil, such as Light Detection and Ranging (LIDAR) and Synthetic Aperture Radar (SAR), but they are not typically used. Newer LIDAR sensors are commercially available and can be mounted and used from UAS, however, responders do not regularly use them because of the complexity of their hardware operation and data handling. Synthetic Aperture Radar (SAR) satellite sensors are used extensively for remote sensing technology of oil spills in non-Arctic waters. However, since ice alters the

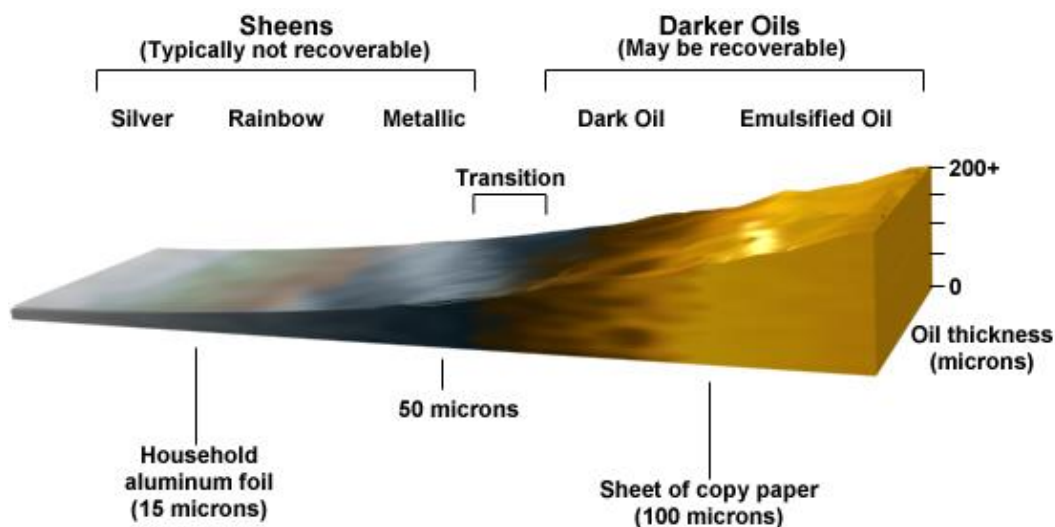


UAS Characterization of Oil in Ice – Volume I: Laboratory Results

geometry of sea surface, they are less useful. With higher resolution and multi-polarized sensors, radar and SAR could overcome this constraint.

1.1.1.1 Optical Sensors

High resolution photography and video have made visual-optical sensors the most used technology for oil spill assessment. The term ‘visual’ comes from the fact that these sensors capture light from the electromagnetic spectrum at the same range as the human eye. Physical properties of the hydrocarbons are directly related to how a floating layer of oil will change its aspect (color and appearance) based on its thickness (Figure 1). The reflection of visible light off oil produces silver sheens, rainbow sheens, metallic, dark, discontinuous true oil color, and true oil color (Table 1). All of these terms refer to how the floating oil ‘looks’ based on its thickness (NOAA-OWOIJ, 2016); Garcia-Pineda et al., 2019; Leifer, 2012; bonnagreement.org/publications).



(Source: Open Water Oil Identification Job Aid for aerial observation (OWOIJ))

Figure 1. Oil thickness classifications.

Table 1. Five levels of oil appearances

Five levels of oil appearances are distinguished in code detailed in the following table:

Code	Description - appearance	Layer thickness interval (µm)	Litres per Km ²
1	Sheen	0.04 to 0.30	40 – 300
2	Rainbow	0.3 to 5.0	300 – 5000
3	Metallic	5.0 to 50	5000 – 50 000
4	Discontinuous True Oil Colour	50 to 200	50 000 – 200 000
5	Continuous True Oil Colour	More than 200	More than 200 000

(Source: OWOIJ)

The capacity of visual sensors to identify these levels of oil thickness makes visual sensors the most applicable and practical for oil spill assessment in non-Arctic and Arctic waters. Geotagged photographs can be used to geo-reference the position, scale, size, distribution, and location of the oil spill elements. Optical sensors can be used for data collection in nadir mode (i.e., looking straight down) or for mapping in oblique



mode. Furthermore, video collection provides awareness of the scale of the spill in reference to the surrounding environment.

1.1.1.2 *Thermal Infrared Sensors*

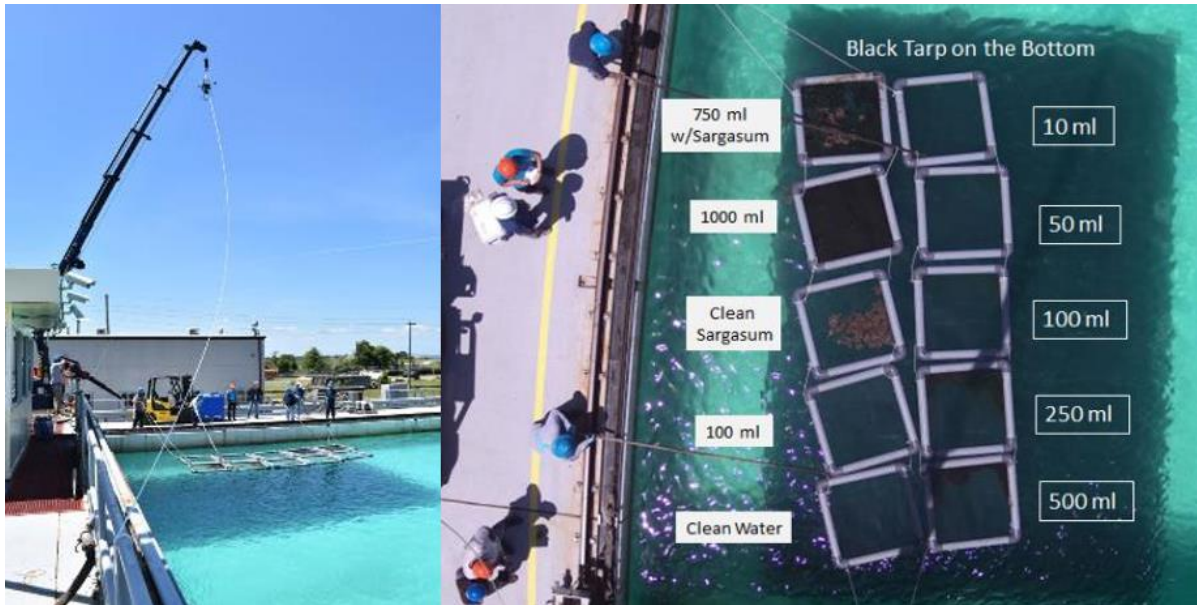
The infrared spectrum for thermal sensors ranges from 1 μm to 1,000 μm , although it can be further separated into three distinct wavebands: ‘Short’, ‘Mid’, and ‘Long’. Infrared (IR) thermal sensors can operate at all three ranges. The short-wave infrared (SWIR) covers the range of 0.9 to 1.7 μm . Because of the high cost of these sensors, there has been limited research on oil spill applications. The spectral atmospheric absorption properties of water vapor and carbon dioxide limit the range of mid-infrared (MWIR) for outdoor applications to 2 to 5.5 μm . BSEE has funded research on this range for oil spill applications (Garcia-Pineda 2019). However, this type of sensor is not commercially available. The most common infrared sensor is the ‘Long-wave Infrared’ (LWIR) (Range = 7 to 14 μm), where atmospheric influences play only a minor role. This is the thermal sensor most commonly used for oil spill research and response operations.

Thermal remote sensing has been used to detect oil slicks on non-Arctic waters during a number of experiments (Garcia-Pineda et al., 2019; Lu et al., 2018; Asanuma et al., 1986; Cross, 1992; Salisbury et al., 1993; Tseng and Chiu, 1994; Cai et al., 2007; Inman et al., 2010). During the Persian Gulf War in 1991, Tseng and Chiu (1994) used infrared imagery on oil slicks with a minimum thickness of 150 μm . They found that the presence of oil showed readings of 2-3 $^{\circ}\text{C}$ higher than those of background water during the daytime and 2 $^{\circ}\text{C}$ lower at night. Satellite imagery collected by the Advanced Very High Resolution Radiometer (AVHRR) aboard the NOAA polar-orbiting satellite determined that these temperature differences were due to solar insolation and the surface heat flux. This effect was confirmed during the DWH oil spill using thermal sensors onboard of the NASA Moderate Resolution Imaging Spectroradiometer (MODIS) satellite.

The use of thermal sensors for determining oil thicknesses has been demonstrated in multiple field and lab-controlled studies (e.g., Lu et al., 2018; Garcia-Pineda, 2019). Oil spill thicknesses have been mimicked in a controlled setting of temperature environment (non-Arctic) at BSEE’s National Oil Spill Response and Renewable Energy Test Facility (Ohmsett) tank using 1m x 1m squares (Figure 2) as well as indoors and outdoors at a University of South Florida’s (USF) marine laboratory (Figure 3) and Water Mapping’s indoor laboratory.



UAS Characterization of Oil in Ice – Volume I: Laboratory Results



(Source: Garcia-Pineda et al., 2019)

Figure 2. Controlled experiments for oil thickness determination using multispectral and thermal sensors.



(Source: Garcia-Pineda et al., 2019)

Figure 3. USF oil tank experiment set up. a) Multi-band cameras and a thermal camera mounted on a tripod frame to collect images of the oil-on-water in the two tanks. (b) and (c) are two identical tanks filled with Tampa Bay water, where the same volume of b) crude oil and c) emulsified oil are put on the water surface using syringes.



1.1.1.2.1 Detection of Oil with Thermal Imagery

Due to oil's specific emissivity properties, thermal remote sensing may have a low detection limit for thickness of oil slicks in non-Arctic waters (Lu Y et al., 2018; Salisbury et al., 1993; Solberg, 2012). In non-Arctic waters (e.g., Santa Barbara seeps, MC20 in the Gulf of Mexico), thermal sensors have been configured to detect oil sheens from thicknesses above the rainbow level with a metallic aspect ($>5 \mu\text{m}$) (Garcia-Pineda et al., 2019) (Figure 4). Synoptic imaging allows comparison of the relative (apparent) temperature variation among the different oil thicknesses (discussed further in Section 1.1.1.2.2). Box 1 on the right side in Figure 4 (corresponding to emulsions) captures apparent colder temperatures between 6.67°C (44°F) and 3.83°C (38.9°F). Box 2 in the center (corresponding to transitioning rainbow sheen to metallic) captures temperatures from 7.06°C (44.7°F) to 8.28°C (46.9°F). The red and blue triangles in the inset boxes indicate the point of warmest and coldest apparent temperatures, respectively.

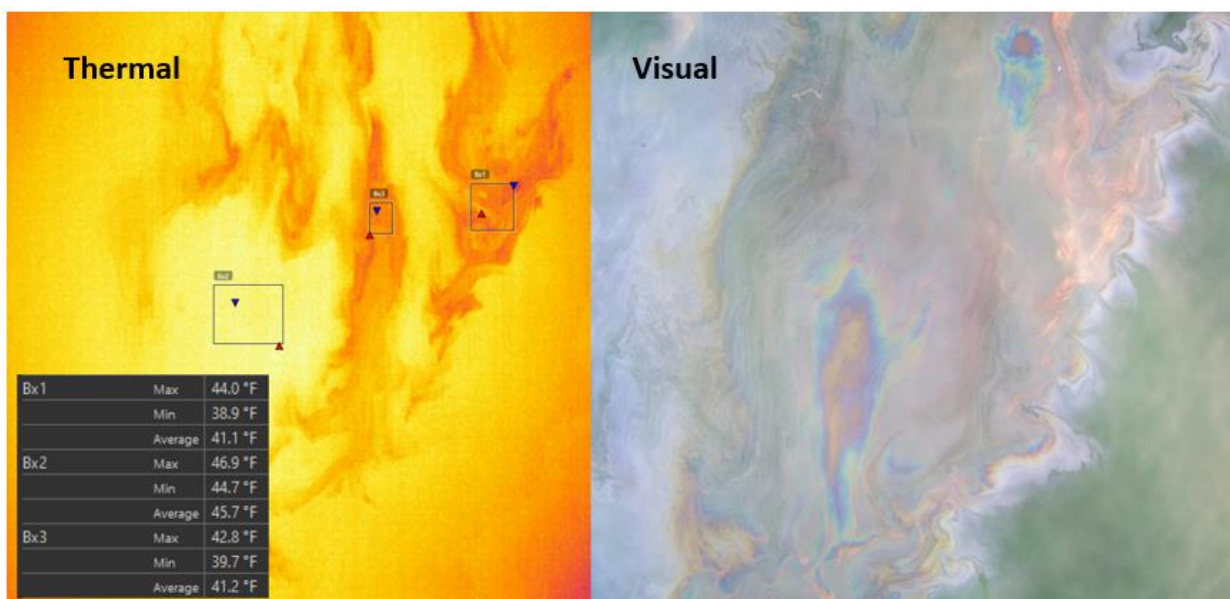


Figure 4. Synchronous thermal and visual imagery of floating oil from the Santa Barbara seep sites. The left and right panels are thermal image and synoptic photograph, respectively, of the same area.

Other research has reported much higher detection levels. For example, Fingas & Brown (1997a, 1997b) reported that thermal sensors are not suitable for the detection of oil slicks thinner than $20 \mu\text{m}$ because the changes in the surface temperature are below the detection limits of the sensors. In this same context, Lu et al. (2018) developed a ground-based experiment (warm waters) in which they found that their minimum detection level was $40 \mu\text{m}$. They concluded that the optimal time for imaging the differences on thermal reflectivity is noon because of the high solar radiation. However, there are difficulties with the sun being at such a high angle because it creates very intense glare, complicating the acquisition of noise-free imagery (i.e., sun-glint glare).

The emissivity of the oil changes the surface-air heat transfer in non-ice conditions and consequently, the thermal contrast between the slick and the background water, which is displayed in the image. Therefore, the minimum detection level for oil thicknesses with thermal imagery depends on sensor radiometric resolution (sensitivity) and test conditions: from $>5 \mu\text{m}$ (Garcia-Pineda et al., 2019) (Figure 4), $20 \mu\text{m}$ (Fingas and Brown, 1997), and $>40 \mu\text{m}$ (Lu et al., 2018). All of these thicknesses are non-actionable sheens (non-recoverable) (Figure 1).

Little is known or published about the maximum level of thickness that can be detected by the thermal sensors. Hypothetically, oil thickness should reach a level above which the radiative heat transfer would be the same (i.e., saturation of the heat signal) and differences between oil thicknesses would be indistinguishable.

1.1.1.2 Thermal Imaging Process

Thermal Inertia (TI) is a physical property of materials describing their resistance to temperature change; Apparent Thermal Inertia (ATI) is an approximation of thermal inertia. As oil thickness changes, so does its emissivity, TI, and conductivity. Non-emulsified crude oil is an insulator and reduces the reflectivity of thermal radiation. As oil starts to emulsify, its conductivity and heat signature change because hydrocarbons bond with water and salt particles. Similarly, illumination conditions (e.g., atmospheric status, time of the day, sun angle, cloud cover, air temperature) must be considered when interpreting thermal imagery.

Calibrated thermal sensors mounted on UAS (e.g., used for controlled experiments or in the field) provide a temperature scale of the oil features captured on the images. When using these sensors, a nominal level of emissivity is set for the entire image. These temperatures are ‘apparent’ and should only be used as a scale or reference among the features captured on the image. (Note: These temperatures may be interpreted as actual [real] temperatures if the exact level of emissivity, ATI, and conductivity of the material are captured on each pixel which rarely happens). As a result, thermal readings are only directly comparable within the image. Similarly, if illumination conditions change within one image or among images, collected at different times, temperature readings computed by calibrated sensors will have an offset. This is another reason why these temperatures are considered ‘apparent’ and should be only used as a reference within the same image.

To date, there have been no studies of oil spill thickness with thermal sensors in the presence of ice and how this would complicate the interpretation of the thermal imagery.

1.1.1.3 Multispectral Imaging

Researchers performed extensive studies of imaging oil spills with multispectral sensors since the DWH spill. Clark et al. (2010) developed a method for studying and characterizing oil emulsification and mapping thicknesses using NASA’s hyperspectral sensor Airborne Visual Infrared Imaging Spectrometer (AVIRIS). With the introduction of multispectral sensors on satellites, several studies were conducted to identify thicker patches of oil emulsions using MODIS (Hu et al., 2018). Newer and better satellites with higher spatial resolution (e.g., Worldview 2-3) have been used to map recent oil spills in the Gulf of Mexico, bays (Lake Washington, LA) and offshore at the Gulf of Mexico (GOM) MC20 spill site (Garcia et al., 2018).

1.1.1.3.1 Physics behind Detection of Oil with Multispectral Sensors

Similar to thermal imaging of oil, spectrophotometers can be used to measure the reflectance of oil and emulsions at different wavelengths within the electromagnetic spectrum. Crude oil has strong absorption in the short wavelengths; the absorption decays exponentially towards longer wavelengths (Byfield, 1998). When oil is emulsified, the oil–water particles have strong scattering at all wavelengths. This effect is manifested in the red-Near Infrared (NIR)-Shortwave Infrared (SWIR) wavelengths (Clark et al., 2010) because of water molecules’ negligible scattering in these ranges.

Despite many attempts to determine reflectance response to oil-on-water (e.g., Otremba and Piskozub, 2001 & 2003; Otremba et al., 2013), in practice it has been very difficult to develop inversion algorithms to classify oil type (e.g., crude vs. emulsified oil) and quantify thickness using the oil’s reflectance spectra.



UAS Characterization of Oil in Ice – Volume I: Laboratory Results

In 2014, Water Mapping, LLC and the U.S. Geological Survey (USGS) conducted spectroscopy experiments with emulsions from the DWH and MC20 sites. These studies were complemented with experiments at Ohmsett (2016, 2018, 2019) and controlled studies at USF in which multispectral cameras used combinations of channels to differentiate between non-emulsified and emulsified oil (Garcia-Pineda 2019). Figure 5 shows the data processing workflow for using multispectral images for characterizing oil thicknesses and differentiating fresh crude oil from emulsions. A combination of multispectral channels (i.e., Near infrared (840 nm), Red (668 nm), and Green (560 nm)) forms of a ‘False Composite’ image to differentiate between oil and emulsified oil. In the upper left is a true color view from the grid of 1m x 1m (3.3ft x 3.3ft) squares at the Ohmsett tank set with different thicknesses. Note the similarity between the squares from true color (visual) imagery. Upper right is false composite image from the multispectral sensor; gradual differences can be distinguished among the squares based on the amount of emulsified oil.

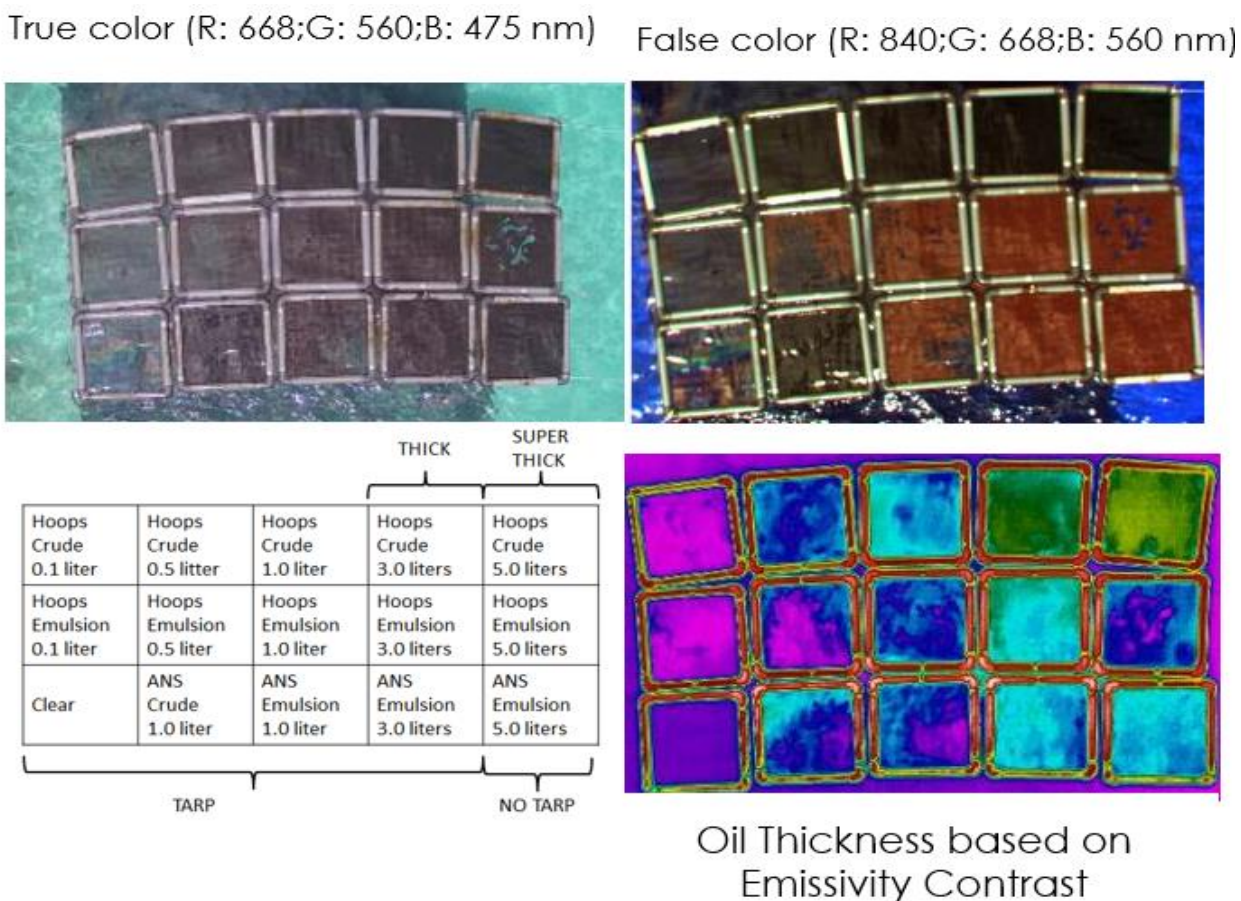


Figure 5. Multispectral classification of oil.

A recent study at the Lake Washington, LA oil spill showed the potential for using multispectral UAS imaging to determine the impact of oil on vegetation and marshes. When this oil spill occurred, layers of floating oil were deposited on the marsh during high tides. Multispectral imaging was used as a tool for the assessment of the oil’s impact on the ecosystem after the spill. (Garcia-Pineda et al., 2019).

1.1.1.4 Baseline of Multispectral Imaging for Oil Spill Imaging

Multispectral sensors capture images on independent channels of the electromagnetic spectrum. By combining these channels and performing band mathematical operations among them, information can be



extracted regarding detection of floating oil and its state (non-emulsified vs. emulsified oil). Integration of these sensors on UAS has been accomplished effectively numerous times in controlled setting conditions and the field (Garcia-Pineda 2019).

1.2 Remote Sensing of Oil in Arctic Conditions

Remote sensing in ice infested conditions depends not only on the physical and chemical properties of the oil, but also the thermal and spectral properties of ice. Therefore, detection of ‘oil on water’ is not easily translatable to ‘oil on water plus ice’. Ice will affect the temperature and the geometry of the surface of the water (and therefore its aspect) which are the main elements for the detection of the oil itself. Floating ice creates physical barriers to oil spreading and transport. In ice-free water, wind greater than 2 m/s creates capillary and gravity waves. Ice may obstruct the direct contact of the wind over the water’s surface.

Responders commonly use multiple sensors to detect oil on water and ice. These sensors can be mounted on different platforms and used at sea level (vessels), low altitude (drones), high altitude (airplanes), or space (satellites) and rely on different mechanisms to detect the oil (Table 2).

Table 2. Sensors used to detect oil on water and ice.

Sensor	Detection of Oil Mechanism	Application on Arctic Conditions
Visual / Optical	Detects the reflected visible light as physical and chemical properties of oil absorb parts of the electromagnetic spectrum.	Contrast between oil and surroundings (ice, snow, water) for detection of oil extent and estimated layer thickness classification.
Multispectral	Multiple bands of sensors with defined channels of wavelengths will capture hydrocarbon signals depending on absorbance/reflectance spectra of each target.	Difference between non-emulsified oil and emulsified oil, also for detection of false positives (e.g., biogenic oils, sargassum).
Thermal Infrared / Forward-looking Infrared	Thermal emissivity differences between oil and surrounding ice/water based on the thermal reflectivity	Detection of oil extent before thermal equilibrium is achieved, estimated layer thickness classification.
Ultraviolet	Reflected ultraviolet contrast between oil, water, and ice	Detection of oil extent and detection of thin oil slicks and sheens
Fluorosensor and Light Detecting and Ranging System (Lidar)	Fluoresced emissions from light and aromatic components of oil	Detection of oil on or just below the sea surface and estimated layer thickness.
Synthetic Aperture Radar (SAR)	Differences in the backscatter signals generated by viscoelastic properties of oil	Detection of oil and extent on the sea surface. Advanced SAR sensors (quad-pol) can detect oil thickness.

1.3 Project Design

This RDC project evaluated the ability of a suite of passive and active UAS sensors to detect and characterize surface oil in cold water environments. More specifically, the project focused on the effect of temperature and percent cover on the efficacy of non-emulsified and emulsified oil detection in a broken ice environment. The project also determined workflow and standard operation procedures (Image Processing Algorithms) for the UAS and sensors for oil detection in ice infested waters to advance capabilities for rapid data product development.



UAS Characterization of Oil in Ice – Volume I: Laboratory Results

CRREL’s Geophysical Research Facility’s (GRF) outdoor test tank had approximately 10 to 12-inch-thick ice sheet cover at the start of the study. CRREL staff cut out 12 individual squares (1m x 1m) from the ice sheet; they served as individual treatments for synoptic UAS and ROV based data collections (Figure 6). CRREL staff added broken ice to individual squares to cover a range of percent ice cover (no ice as control, 5-10%, 25%, 50%, 80%). These percent ice cover treatments were used throughout the experiments. Eighteen black plastic totes, each with a unique thickness and or oil type, provided a point of reference for the reflectance of thermal and spectral radiation for calibration for the UAS sensors (Figure 7). The totes were black to avoid reflections from the bottom or ice.



Figure 6. Ground view of the GRF tank with ice squares (1m x 1m) and black plastic totes for oil thickness calibration.

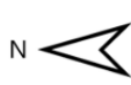
N 	No Oil	10 μm	50 μm	100 μm	200 μm	← Fresh ANS
	No Oil	10 μm	50 μm	100 μm	200 μm	← 50/50 Emulsion
		500 μm	1000 μm	2000 μm	5000 μm	← Fresh ANS
		500 μm	1000 μm	2000 μm	5000 μm	← 50/50 Emulsion

Figure 7. Target thicknesses of each tote for reference of spectral and thermal reflectance.

These known amounts were used for calibration of the UAS sensors.



1.4 Equipment and Working Area Configuration

The project team set up a base station next to the GRF tank where the data being collected from the UAS could be seen in real time. TV screens and laptops displayed the imagery collected from the UAS to ensure data was being obtained properly during the flights (Figure 8).



Figure 8. Left: Screens displaying the thermal and visual data in real time from the UAS. Right: Control base station that monitored the telemetry of the UAS.

The UAS was a Freefly Alta-X (Freefly Systems, Inc.; Woodinville, WA) multirotor quadcopter with a maximum payload capacity of ~14 kg and mounts for multiple sensors (Figure 9 and Figure 10). The Alta-X has a 2.3 m wingspan (props unfolded) and is 1.1 m tall. The carbon fiber and aluminum UAS uses two 12S Lithium Polymer batteries. With a standard payload of 7 kg, it can perform flights of up to 20 minutes.



Figure 9. UAS aircraft used for the experiment.



UAS Characterization of Oil in Ice – Volume I: Laboratory Results

All the cameras were synchronized to collect imagery every second, once triggered. The project team flew all missions at two altitudes, 13.7 m (45 ft) and 30.5 m (100 ft), to capture the full detail of the oil and ice in the squares and totes.

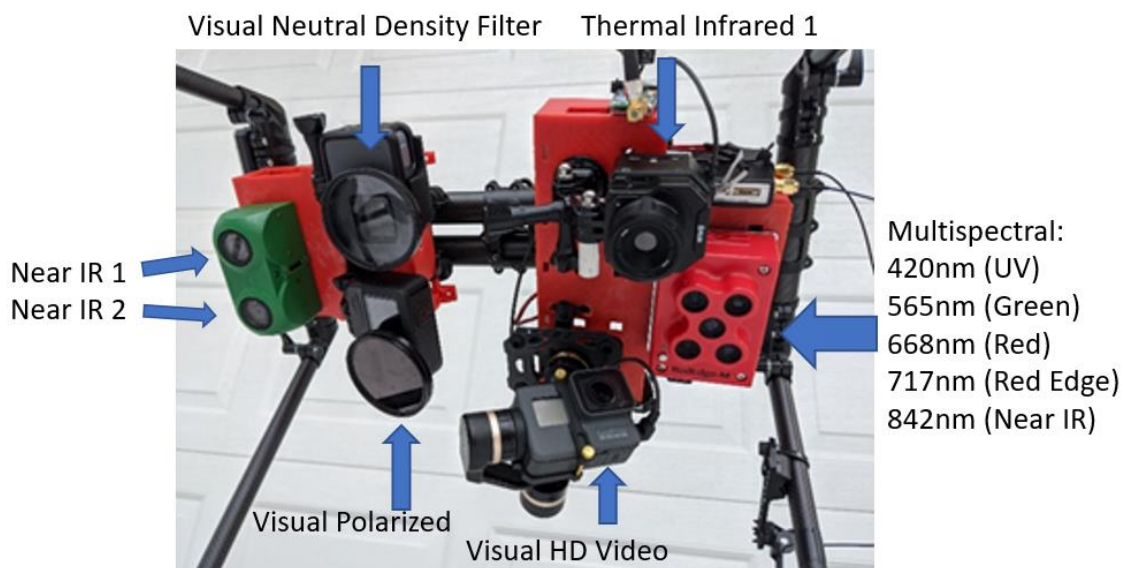


Figure 10. Sensors mounted on the landing gear of the UAS.

Each square received the requisite ice cover (Figure 11). Then, CRREL staff added the amount of oil required to achieve the target test thickness in each square (Figure 12) to obtain 10 μm , 50 μm , 100 μm , 200 μm , 500 μm , 1 mm, 2 mm, and 5 mm slicks. The pilot flew the UAS across the array of squares to collect the data for that test thickness condition. After each flight (data collection with the UAS for a given test condition), CRREL staff increased the oil thickness on each square to the next level until all the target thicknesses were imaged.



UAS Characterization of Oil in Ice – Volume I: Laboratory Results

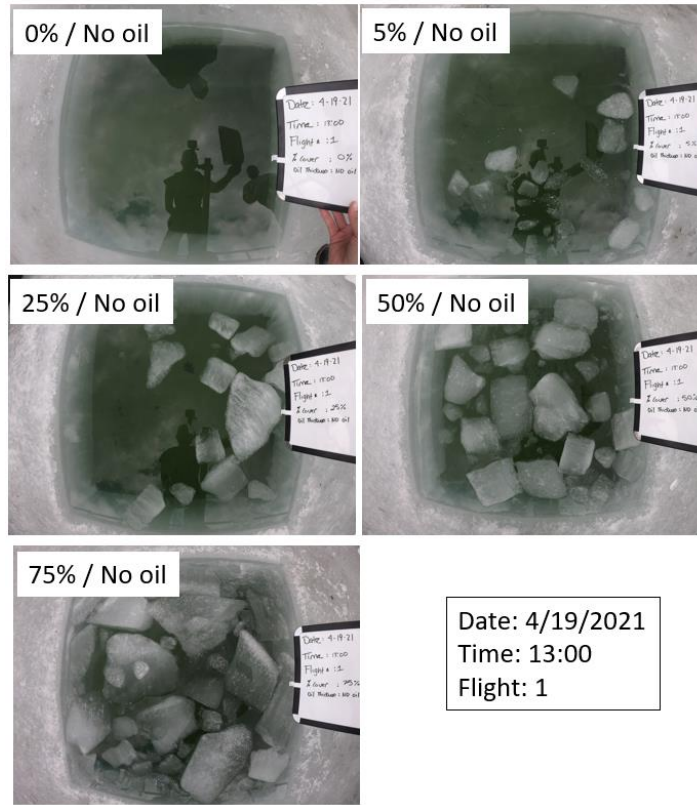


Figure 11. Close up for each of the squares with corresponding ice cover before oil was added to the squares.



Figure 12. Adding controlled amounts of oil into squares to produce established thickness layers.



UAS Characterization of Oil in Ice – Volume I: Laboratory Results

Figure 13 shows an aerial view obtained by the UAS just prior to the testing. CRREL staff added oil to the squares to achieve prescribed target oil thickness categories (based on surface area to volume estimates). The project team used Alaska North Slope (ANS) crude, supplied by CRREL, as the non-emulsified oil. CRREL staff weathered the ANS to 75-80% of the original mass, then mixing in ~30 ppm salt water at a 50:50 (by volume) ratio. Emulsions were continuously mixed in a 1.25 m³ tote with a lube pump for >3 days to allow for stabilization. Oil thickness categories were ‘no oil’ controls, 10 μm, 50 μm, 100 μm, 200 μm, 500 μm, 1 mm, 2 mm, and 5 mm (Figure 13) (Table 3).

Table 3. Test conditions at CRREL.

Oil Type	% Ice Cover	Sequentially Tested Oil Thickness (μm)
Non-emulsified ANS	0	0 → 10 → 50 → 100 → 200 → 500 → 1,000 → 2,000 → 5,000
Non-emulsified ANS	5	0 → 10 → 50 → 100 → 200 → 500 → 1,000 → 2,000 → 5,000
Non-emulsified ANS	25	0 → 10 → 50 → 100 → 200 → 500 → 1,000 → 2,000 → 5,000
Non-emulsified ANS	50	0 → 10 → 50 → 100 → 200 → 500 → 1,000 → 2,000 → 5,000
Non-emulsified ANS	80	0 → 10 → 50 → 100 → 200 → 500 → 1,000 → 2,000 → 5,000
Emulsified ANS (50/50)	0	0 → 10 → 50 → 100 → 200 → 500 → 1,000 → 2,000 → 5,000
Emulsified ANS (50/50)	5	0 → 10 → 50 → 100 → 200 → 500 → 1,000 → 2,000 → 5,000
Emulsified ANS (50/50)	25	0 → 10 → 50 → 100 → 200 → 500 → 1,000 → 2,000 → 5,000
Emulsified ANS (50/50)	50	0 → 10 → 50 → 100 → 200 → 500 → 1,000 → 2,000 → 5,000
Emulsified ANS (50/50)	80	0 → 10 → 50 → 100 → 200 → 500 → 1,000 → 2,000 → 5,000

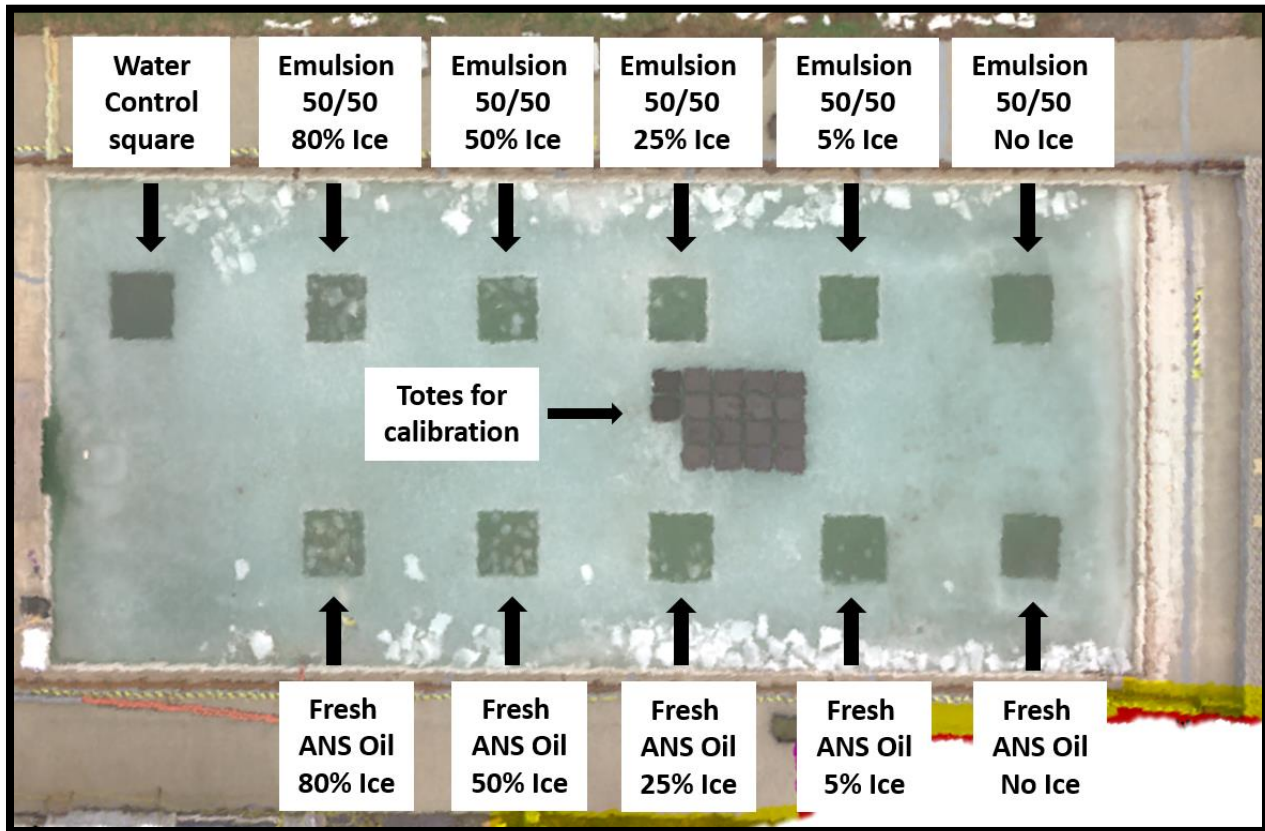


Figure 13. Aerial view of the tank setup before oil was added to the squares.



UAS Characterization of Oil in Ice – Volume I: Laboratory Results

Each of the maps or aerial photographs shown in this report (e.g., Figure 13) was made by stitching a number of individual still images to create an orthomosaic (i.e., multiple photos collected from different positions as the UAS was flying the tank at 13.7 m (45 ft)).

1.5 Effect of Daily Temperature and Illumination of Sensor Operation

Once all the flights for the thicknesses and ice cover matrix had been completed, the project team carried out an additional calibration experiment. The team fixed multispectral, visual, and thermal cameras to an A-Frame located over one square that was surrounded by totes containing non-emulsified and emulsified oil at a range of thicknesses (Figure 14).



Figure 14. Setup for time-lapse study. Left: A-Frame with cameras; Right: setup of the totes with different thicknesses and oil types.

The cameras recorded images every minute (thermal and visual sensor) and 3 minutes (multispectral) over a 24-hour period. The project team analyzed the influence of light levels (illumination) and temperature on thermal and multispectral reflectivity for the full day period (Figure 15). During the test period, there was great variation in these conditions (i.e., snowing, sunny, cloudy) producing a rich dataset of environmental variation.



UAS Characterization of Oil in Ice – Volume I: Laboratory Results

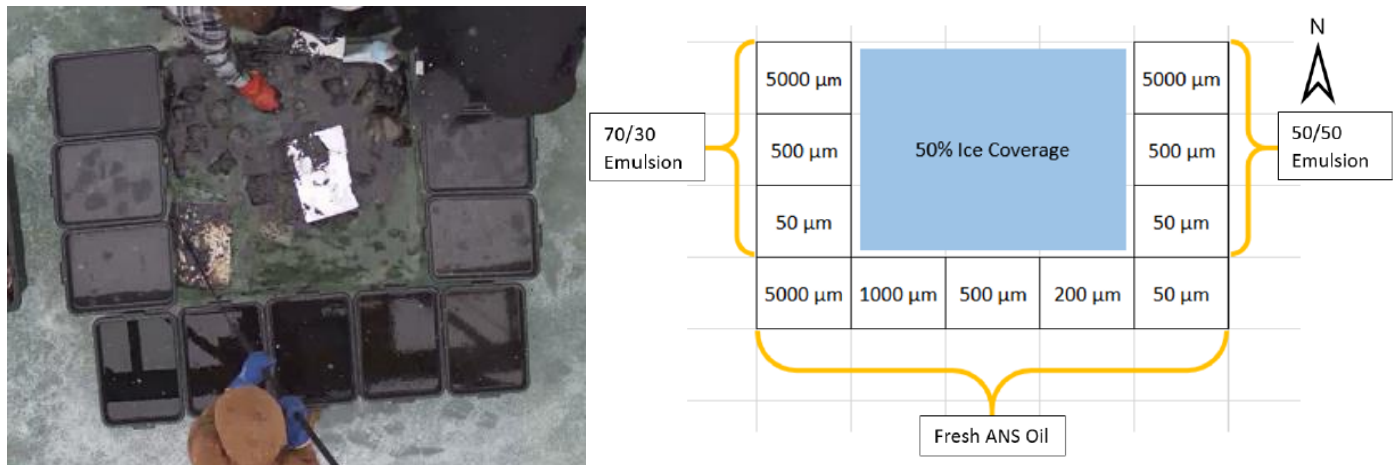


Figure 15. View from the top of the A-Frame for the daily temperature and illumination effect experiments.

1.6 Physical Thickness Measurements: Tube Sampling

The project team also took physical thickness measurements of the oil inside the 1m x 1m ice squares with a tube sampler that Water Mapping developed (Figure 16). The project team placed it on the surface of the oil-ice-water mixture. The sampler holds a crystal tube, which contacts the surface and collects an undisturbed profile of the upper layer of the oil on the water. The instrument has sensors and an electronic mechanism that automatically caps the ends of the crystal tube after the profile is collected. The tube is removed from the sampler and the thickness of oil can be measured with a digital camera or by extracting the oil.



Figure 16. Tube sampler measuring oil thickness.

The project team collected and analyzed a total of 11 thickness measurements with the tube sampler (Figure 17).

UAS Characterization of Oil in Ice – Volume I: Laboratory Results



Figure 17. Processing the tube samples for oil thickness.

Figure 18 and Figure 19 show sample extraction and sample processing, respectively, for emulsified oil (50/50) and 50 μm thickness. Measurements were collected for five thicknesses and several types of emulsified and non-emulsified oil (Table 4). Volume II of this RDC report, “UAS Characterization of Oil in Ice – Volume II: Supplemental Laboratory Data” contains all data related to measuring samples’ oil thicknesses.

Table 4. Combination of a target oil type (emulsified [ratio], non-emulsified) and oil thickness monitored in the 1m x 1m squares, using the tube samplers.

Flight #	Oil Type (Ratio)	Oil Thickness
Target Oil and Thickness 1:	(50/50)	50 μm
Target Oil and Thickness 2:	(50/50)	500 μm
Target Oil and Thickness 3:	(50/50)	5,000 μm
Target Oil and Thickness 4:	(30/70)	50 μm
Target Oil and Thickness 5:	(30/70)	500 μm
Target Oil and Thickness 6:	(30/70)	5,000 μm
Target Oil and Thickness 7:	Non-emulsified	50 μm
Target Oil and Thickness 8:	Non-emulsified	500 μm
Target Oil and Thickness 9:	Non-emulsified	1,000 μm
Target Oil and Thickness 10:	Non-emulsified	5,000 μm
Target Oil and Thickness 11:	Non-emulsified	200 μm





Figure 18. Example of sample processing for the tube sampler with emulsified (50/50) oil at 50 μm .

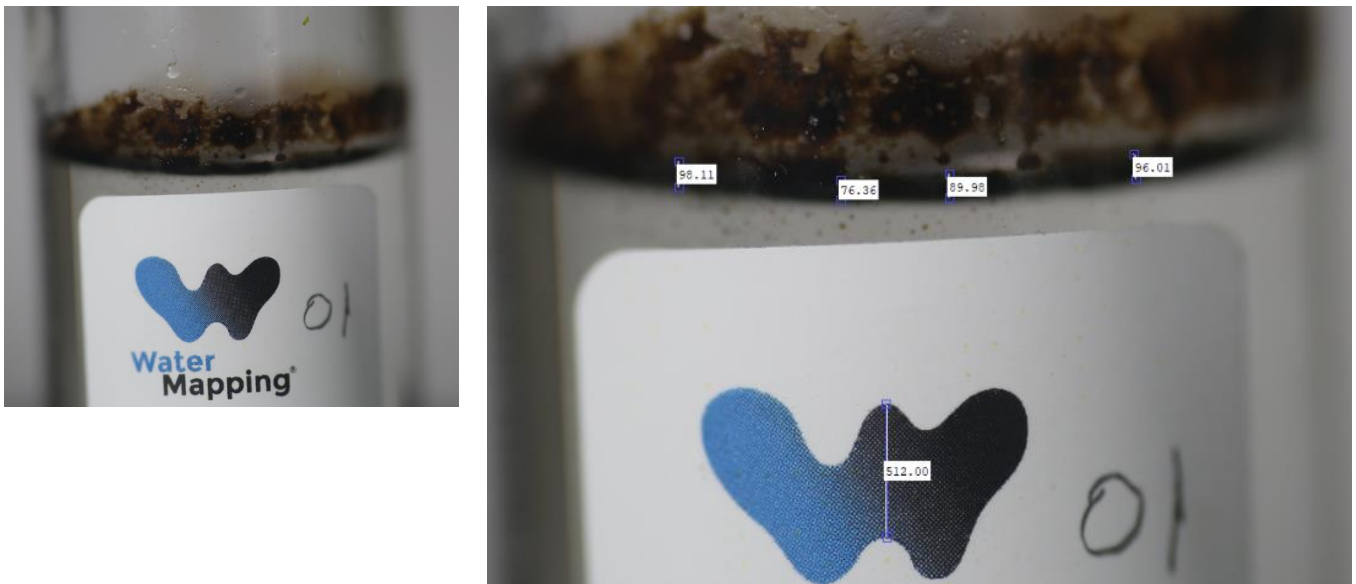


Figure 19. Oil Line: 98, 76, 90, 96 pixels with an average of 90 pixels. Line Thickness: 791 μm . Reference: 512 pixels (4,500 μm).

1.7 Acoustic Sensors

The acoustic sensors used for the underwater thickness assessment were single element piezoelectric-based transducers commonly used by the nondestructive evaluation and sonar communities. The multibeam, multi-frequency sonar system was integrated into a remotely operated vehicle (ROV) called BlueROV 2. The project team deployed it with six acoustic sensors ranging from 2.25 MHz to 10 MHz to measure slicks $\geq 500 \mu\text{m}$ and thicker with a sensitivity of $\sim 100 \mu\text{m}$.

2 EXPERIMENTAL DESIGN

Table 5 shows a summary of all the multispectral flights conducted during the experiments.

Table 5. UAS flights made during CRREL experiments.

Flight	Date	Start Time (hr)	Weather Conditions	Illumination Conditions	Mission Objectives and Thickness
WM_Flight 01	4/19/2021	1040	Overcast	Cloudy	Test flight
WM_Flight 02	4/19/2021	1310	Overcast	Cloudy	10 µm initial oil on ice flight
WM_Flight 03	4/19/2021	1550	Overcast	Cloudy	Increase to 50 µm.
WM_Flight 04	4/20/2021	0838	Overcast	Cloudy	Repeat 50 µm with frost cover
WM_Flight 05	4/20/2021	0950	Overcast	Cloudy	Increase to 100 µm
WM_Flight 06	4/20/2021	1136	Overcast	Cloudy	Increase to 200 µm
WM_Flight 07	4/20/2021	1316	Overcast/ Windy	Cloudy	Increase to 500 µm
WM_Flight 08	4/20/2021	1409	Overcast/ Windy	Cloudy	Increase to 1 mm
WM_Flight 09	4/20/2021	1437	Wind gusts	Cloudy	Increase to 2 mm
WM_Flight 10	4/20/2021	1530	Wind gusts	Cloudy	Increase to 5 mm

During each flight, the project team collected raw data from the 475 (Ultraviolet [UV]), 560, 668, 717 (Red Edge), and 840 (Near IR) nm and Red, Green Blue (RGB) channels of the multispectral sensors. Figure 20 shows an example of the images collected for the 04/19/2021 Flight 2. Figure 21 shows the data products generated from this same flight. These images include independent channels and pre-determined algorithms that are commonly used for detection of oil on land. Figure 22 shows the conditions at ground level during Flight 2.

Multispectral data available with the channels described in Figure 20, allowed the project team to produce image outputs from known algorithms used on other non-Arctic applications related to land, vegetation and soil characterization. These outputs are: Optimized Soil-Adjusted Vegetation index (OSAVI), Digital Surface Model (DSM), which is used as a tool for elevation of the surface imaged, Normalized Difference Vegetation Index (NDVI), used to measure of health for vegetation, and Normalized Difference Red Edge (NDRE), which is used for quantification of chlorophyll content. Figure 21 shows an example of these outputs.



UAS Characterization of Oil in Ice – Volume I: Laboratory Results

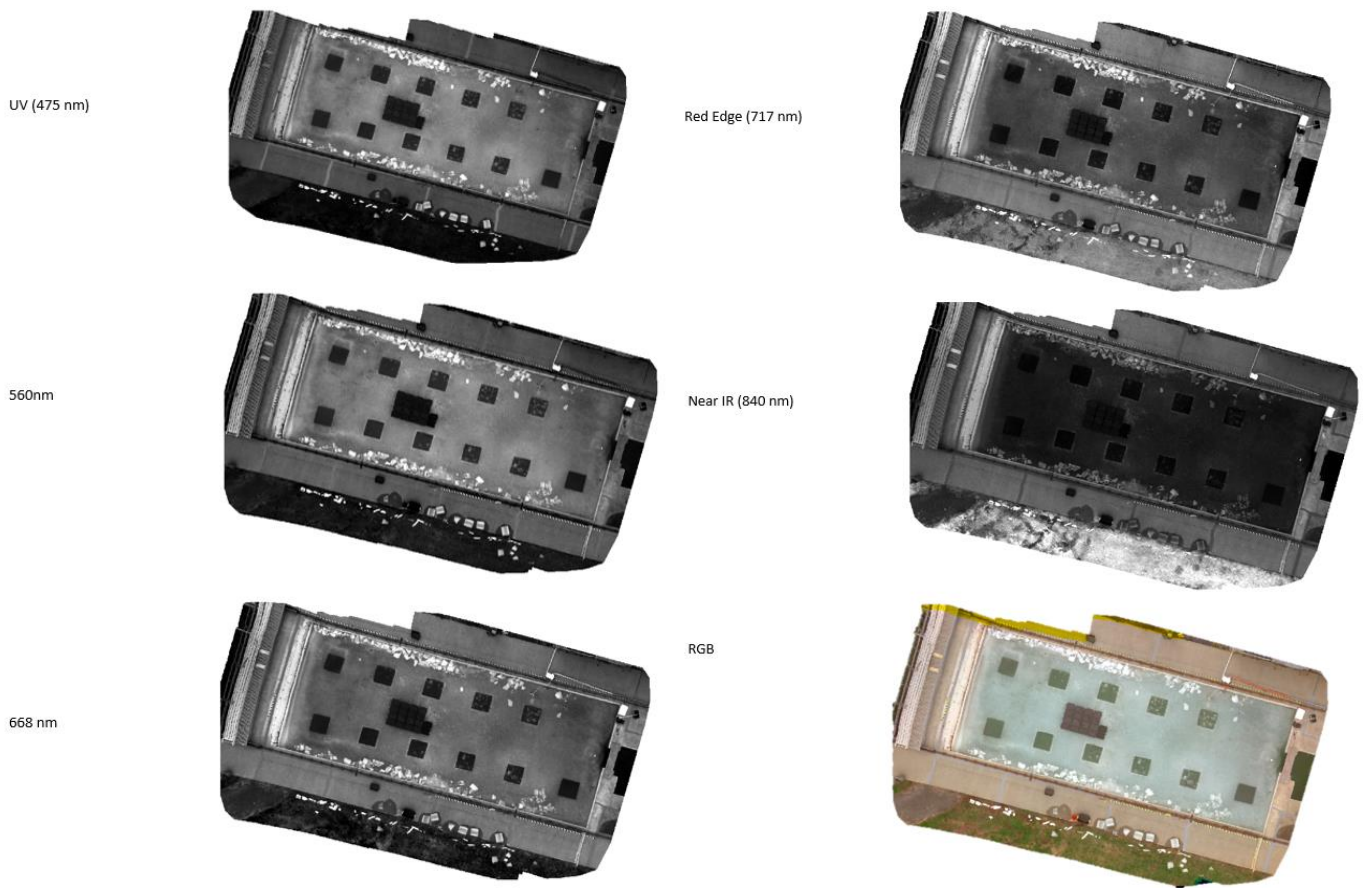


Figure 20. Example raw data from independent channels (475 nm, 560 nm, 668 nm, 717 nm, and 840 nm) wavelength for the multispectral.



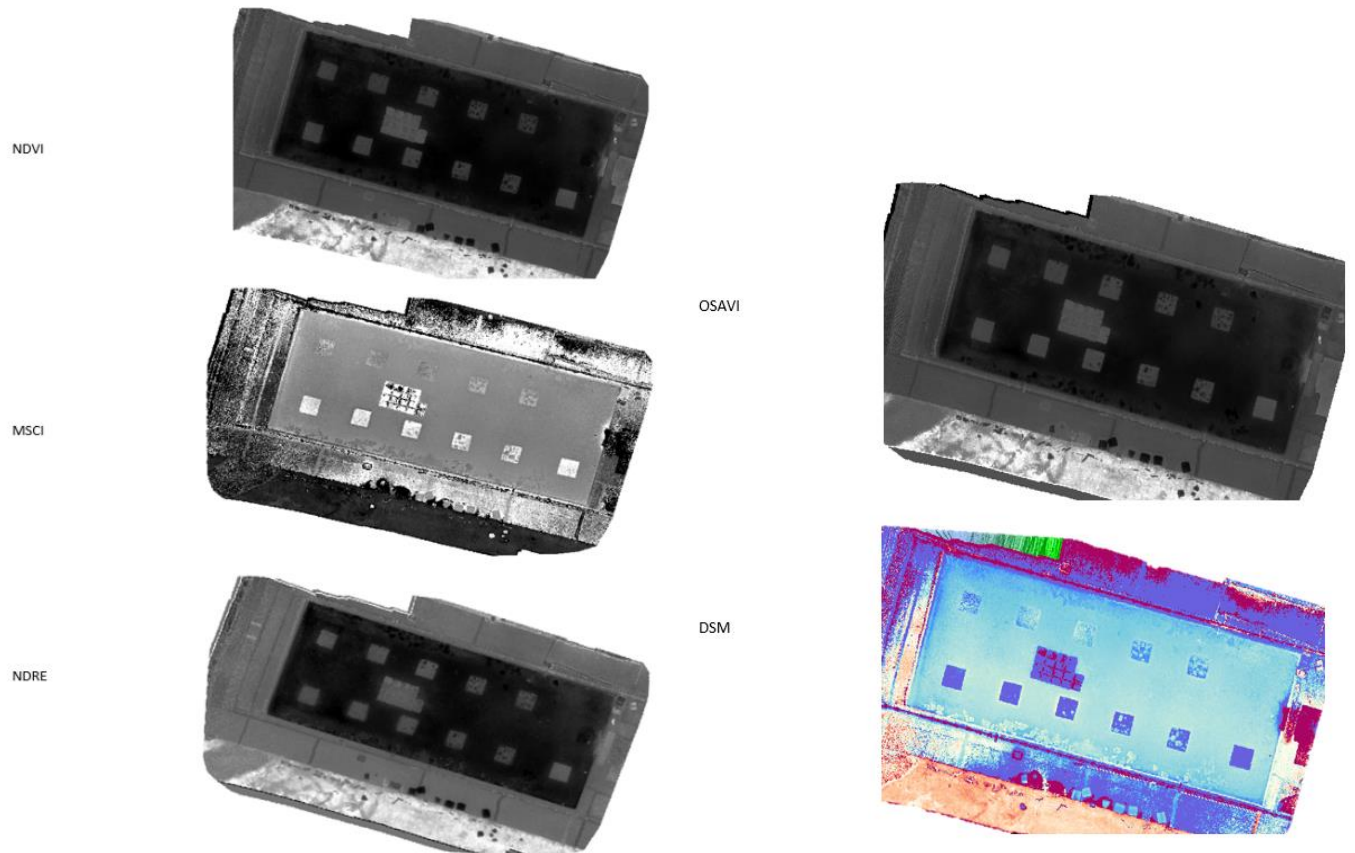


Figure 21. Example predetermined algorithms using the multispectral sensor data.

UAS Characterization of Oil in Ice – Volume I: Laboratory Results

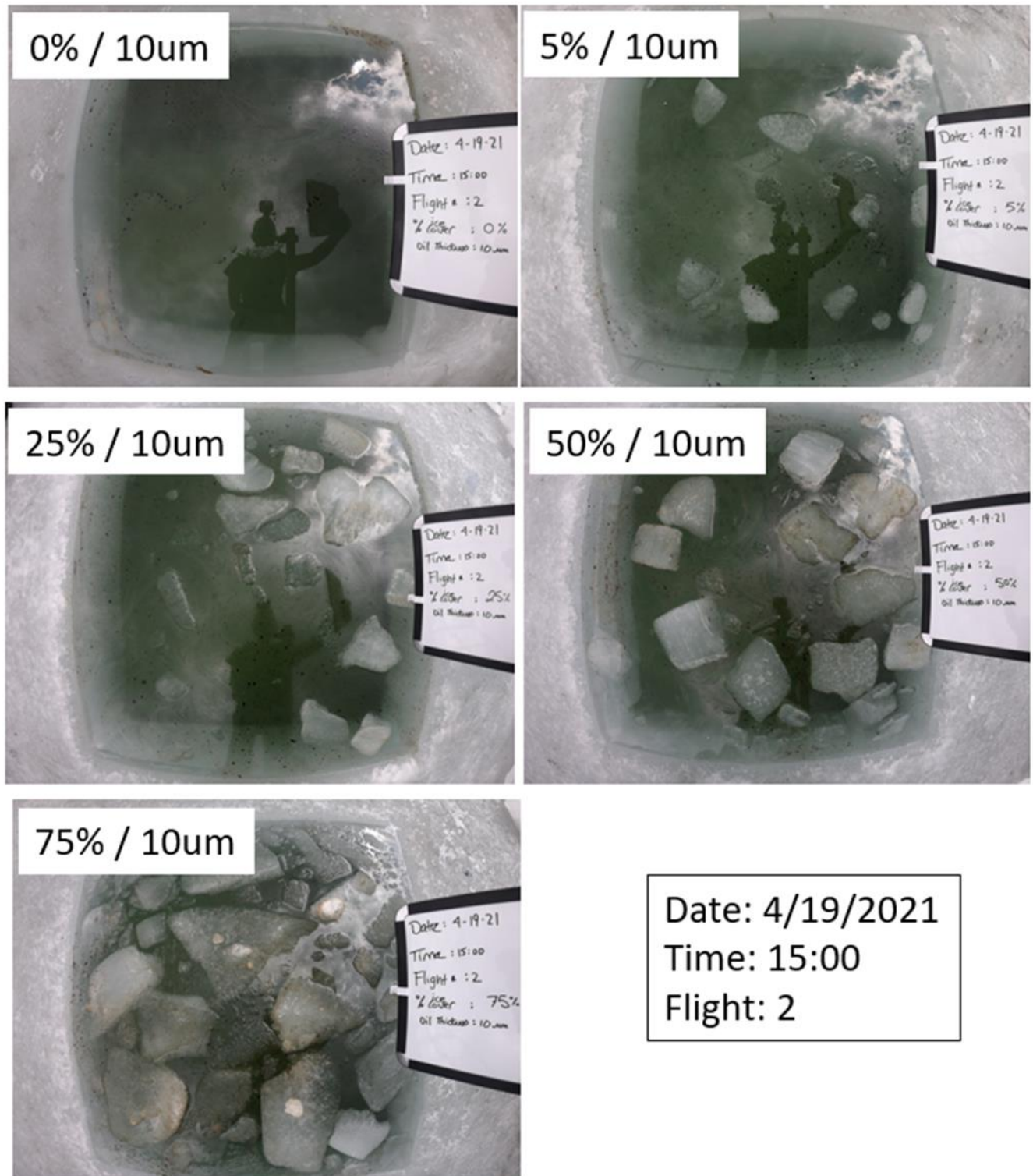


Figure 22. Ground level photographs taken when Flight 2 was occurring.

Volume II of this RDC report, “UAS Characterization of Oil in Ice – Volume II: Supplemental Laboratory Data” shows data from all of the flights.



3 RESULTS AND DISCUSSION

3.1 Multispectral and Thermal Imagery

The CRREL experiments were divided into four focus areas: (1) Multispectral imagery to differentiate between emulsified and non-emulsified oil; (2) Thermal imagery at 30.5 m (100 ft) for coarse resolution of oil thickness; (3) Thermal imagery at 13.7 m (45 ft) for high resolution of oil thickness without disturbing the oil's surface; and (4) 24-hour time lapse multispectral and thermal imagery to determine the effect of incident solar radiation. Although optical sensors are widely used in spill response operations, the focus of CRREL experiments was to advance the science of multispectral cameras in identifying and characterizing surface oil in icy environments.

3.1.1 Multispectral Differentiation of Non-Emulsified Oil and Emulsified Oil

Knowing what the emulsification state of oil is essential when responding to a spill. Multispectral sensors are useful in this regard because they are able to discern between the two states in temperate waters. Using true color makes emulsified and non-emulsified oil very difficult to distinguish, but use of false composite bands with the multispectral sensor would make the differences easier to see. A false color composite image of the emulsified and crude oils showed different reflectance in the Red, Near IR (NIR) and Green bands (Figure 23).



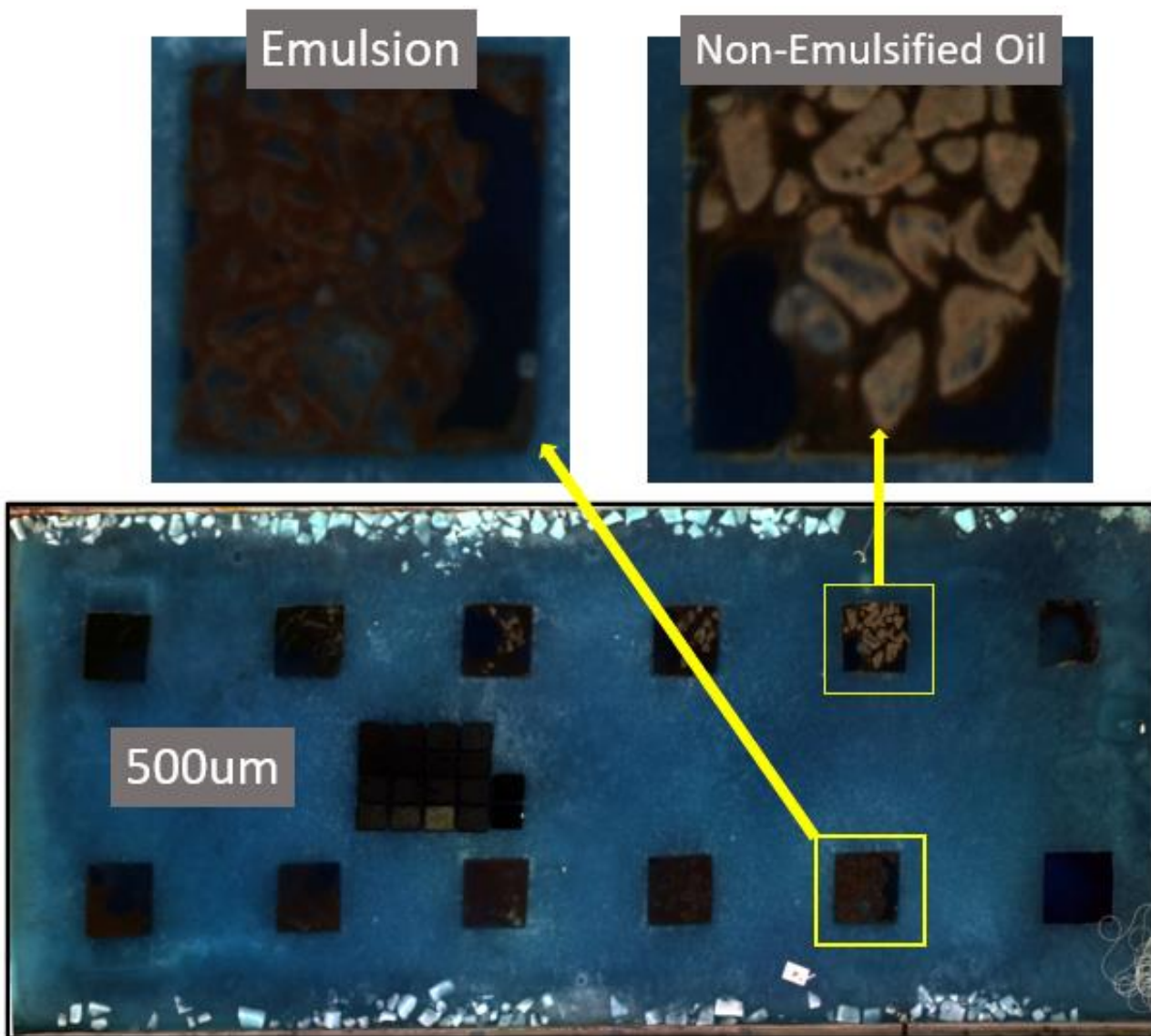


Figure 23. Emulsified vs non-emulsified oil detection using multispectral sensors (500 µm thickness, 75% ice cover).

Emulsions have low reflectance in these bands compared to non-emulsified crude and algorithms can be developed to discern oil emulsions from crude oil. In Figure 23, emulsified oil is dark brown and the ice is difficult to distinguish. Non-emulsified is a lighter brown and ice is distinguishable.

The project team explored potential combinations of multispectral bands and found that the NIR (840 nm), RedEdge (717 nm), and Red bands (668 nm) resulted in the greatest contrast between emulsified and non-emulsified oil in the ice-water mixture. Using this combination of spectral channels, the ice square coated with emulsified oil appeared gray in the images, while the emulsified oil appeared brown (Figure 24). The ice square coated with non-emulsified oil appeared white, while the ice appeared gray. The non-emulsified oil on the water's surface was brownish. For comparison, Figure 24 includes an image of the non-emulsified oil with both the NIR, RedEdge, Red and the Red, NIR and Green composite images.

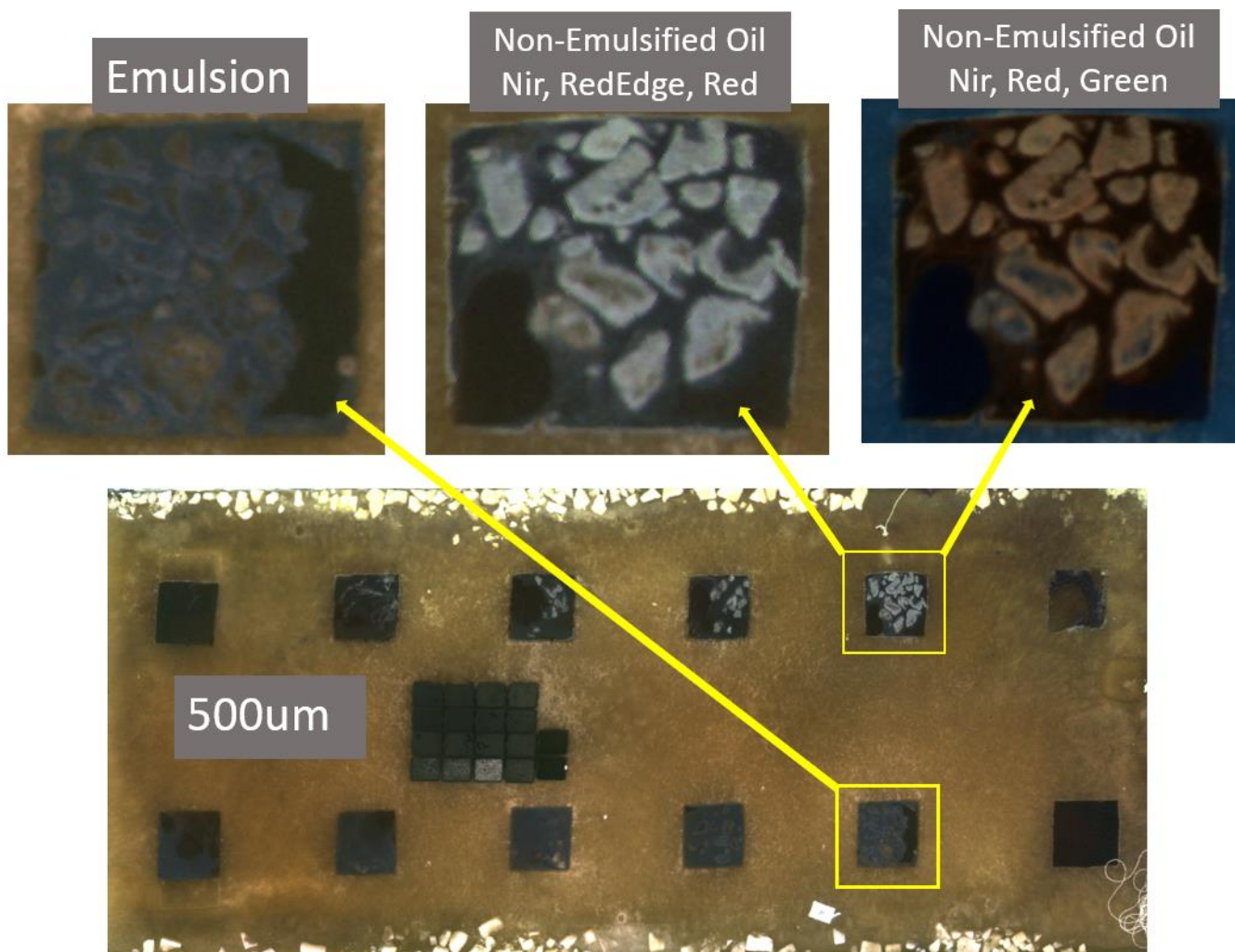


Figure 24. Emulsified and non-emulsified oil (500 μm , 75% ice cover).

For the false color composite combining NIR, RedEdge, and Red bands the ice sheet appears to be brown, non-emulsified oil on the ice is almost white and the ice appears to be gray. The oil on the surface of the water is brownish. The NIR, Red, and Green composite (from Figure 23) shows the non-emulsified oil associated with the ice as light brown, but the oil on the water's surface is brown and harder to distinguish from the water itself. The NIR, RedEdge and Red composite causes the emulsified oil on the water to look brownish and the oil on the ice to appear gray.

The project team tested the algorithm (See Section 3.3) of the false composite bands Near Infrared, RedEdge, and Red bands with different oil thicknesses and percent ice covers. For example, Figure 25 shows how 200 μm oil appears on a square 75% covered with ice. The contrast and coloration between the emulsified and non-emulsified oil was consistent between Figure 24 and Figure 25. The coloration suggested that the presence of the ice did not affect the detection/reflectance for this false composite combination of wavelengths for thicknesses ranging from 200 to 5,000 μm .

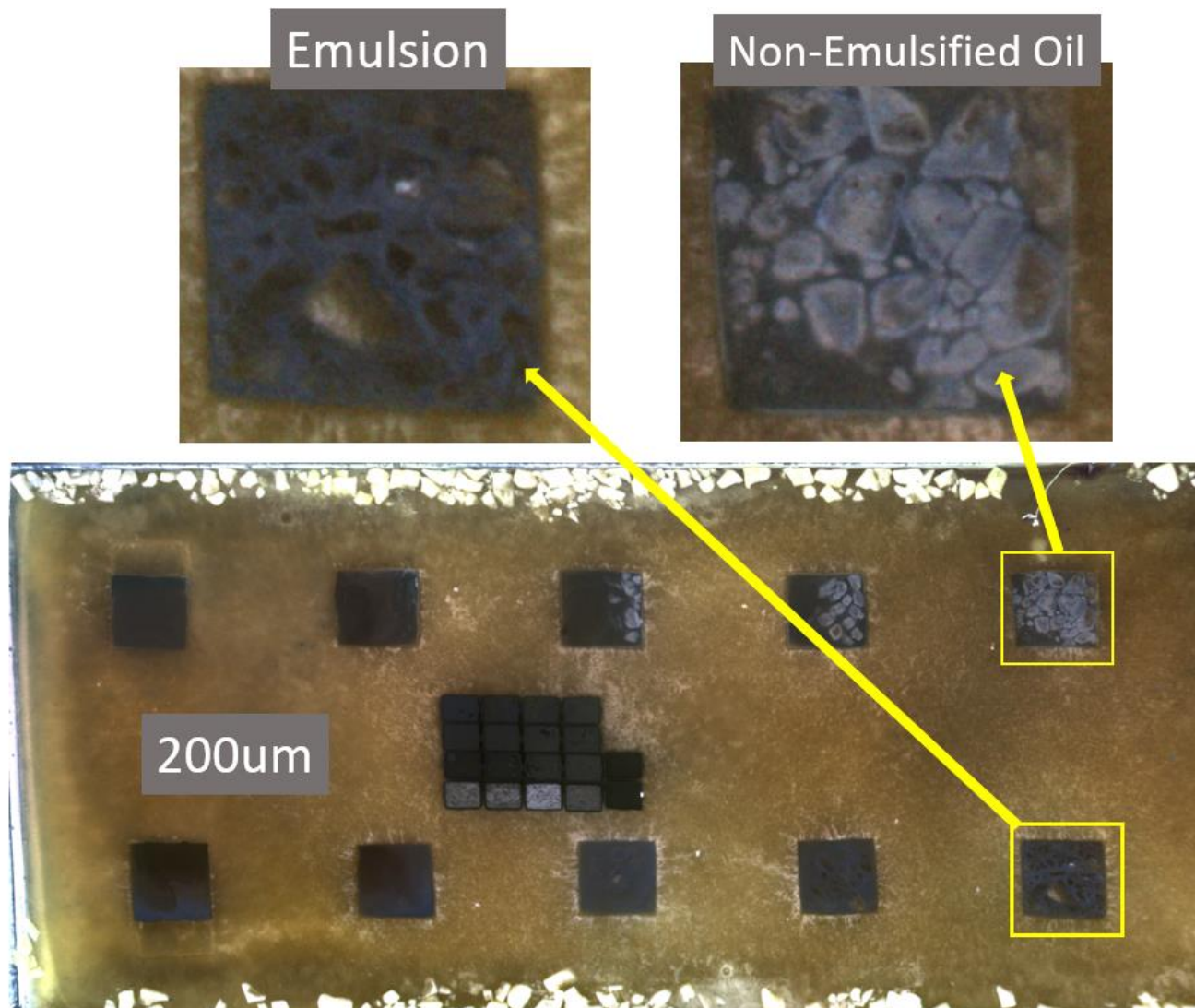


Figure 25. Emulsified vs. non-emulsified oil (200 µm, 75% ice cover).

The NIR, RedEdge, and Red composite in Figure 25 shows the same pattern of coloration as in Figure 24. The Red NIR, Green composite shows the non-emulsified oil associated with the ice as a light brown, but the oil on the water's surface is brown and harder to distinguish from the water itself. The NIR, RedEdge and Red composite causes the emulsified oil on the water to look brownish and the oil on the ice to appear gray.

The lower limit of detection for the NIR, RedEdge, and Red composite was around 100 µm of oil thickness (

Figure 26). The contrast between the oil and the emulsion is faded and only appreciable on certain areas of the squares. This result is consistent with observations from the field from previous experiments of oil on water (Garcia-Pineda et al., 2019). Creating an even layer of emulsion at 100 µm is difficult. Emulsified oil normally creates thicker patches of mousse that converge resulting on very thick, unevenly distributed layers and are more viscous than oil itself.



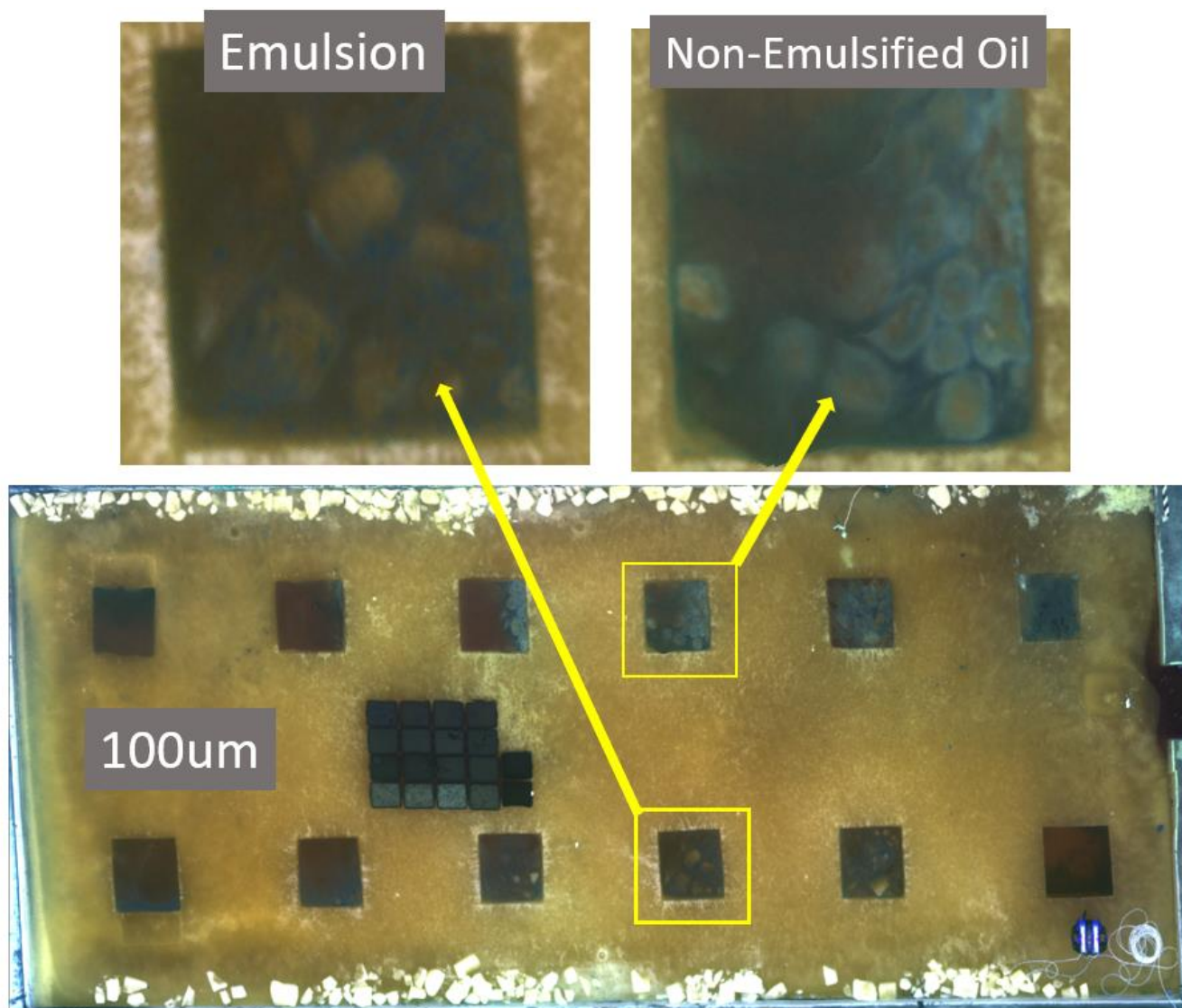


Figure 26. Emulsified vs non-emulsified oil (100 μm , 50% ice cover).

For the NIR, RedEdge, and Red composite, the contrast between the non-emulsified and emulsified oil is faded and only appreciable on certain areas of the squares. 100 μm is near the limit of detection for ANS crude under these conditions.

3.1.2 Thermal Analysis of the Oil Thickness

The project team carried out pre-test flights to determine the minimum altitude a UAS could fly without disturbing the surface of the water. The first flight determined that a UAS flying at 11 m (36 ft) would not produce turbulence on the surface of the squares or totes. The team decided that 13.7 m (45 ft) was the minimum altitude the UAS would be flown to ensure the highest resolution possible without affecting the targets samples. A higher altitude of 30.5 m (100 ft) was used for reference as a coarser resolution with a larger field of view.



UAS Characterization of Oil in Ice – Volume I: Laboratory Results

3.1.2.1 Thermal Analysis at 30.5 m Altitude

Figure 27 shows the aerial view of the GRF tank at 30.5 m for a 10 μm layer of oil. The cut-out ice squares and totes are enclosed within the GRF. The normal true visual color, the linear gray scale thermal, and the non-linear bi-color thermal views are in the left, center, and right panels, respectively. The thermal sensor’s linear gray scale ranges from black (-3.89 °C (25 °F)) to white (26.7 °C (80 °F)). The non-linear bi-color thermal view has the same range of temperature, but the corresponding colors are black and yellow. Totes contained oil with thicknesses ranging from no oil to 5,000 μm for both emulsified and non-emulsified oil.

Non-linear bi-color images do not use the same color palette. Software used for these analyses (e.g., FLIR tools in this case) allow the analyst to select the best color palette to differentiate over the range of apparent temperatures for the data collected (e.g., oil, ice). For example, in Figure 27, the apparent temperature range to optimize visualization is -3.89 °C (25 °F) (black) to 26.7 °C (80 °F) (yellow-white). For this reason, all subsequent bi-color images will show the apparent temperature range used to optimize the visualization of the data collected. Data with an apparent temperature range of 1.1 °C (34 °F) to 18.9 °C (66 °F) would have different predefined color palettes depending on which one could achieve the highest contrast among features.

The 10 μm layer is undetectable in the squares and the totes with the normal (true) visual color at the linear gray scale. The different thicknesses in the totes are more readily distinguished in both thermal images (linear gray scale and non-linear bi-color). It is important to note that these temperatures are apparent and not actual temperatures. The totes temperature variations occur because thinner layers of oil (10 to 200 μm) absorb less solar radiation than the thicker layers (500 to 5,000 μm) and are therefore colder.

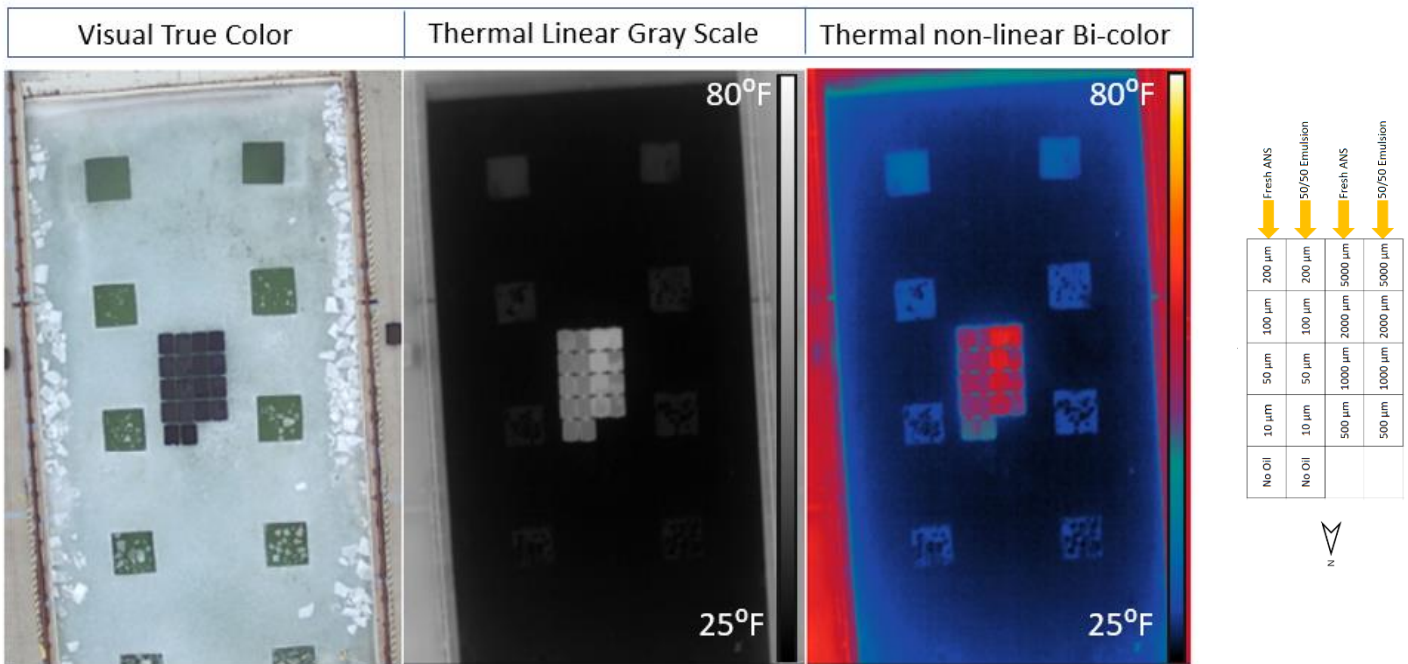


Figure 27. Aerial view of the GRF tank with the 1m x 1m squares with 10 μm of oil and different amounts of ice and the totes with different thicknesses of oil.



UAS Characterization of Oil in Ice – Volume I: Laboratory Results

The thermal reflectivity using the non-linear bi-color scheme clearly detects the ice in the 1m x 1m squares and the contrast of the oil thicknesses in the totes becomes even clearer. The darker colored totes contained cooler, thinner slicks (10 to 200 μm), while the lighter red totes contained warmer, thicker slicks (500 to 5,000 μm). This suggests that the non-linear bi-color scheme can detect the presence of floating oil slicks and be used to differentiate between water, ice, and oil. As the non-linear bi-color scheme on the right in Figure 27 shows, when there is a thin layer of oil (i.e., 10 μm) the amount of ice cover affects the temperature, and therefore, the thermal sensor's output. When there is less ice cover, there are higher apparent temperatures and darker colors (black), whereas more ice produces comparatively lighter colors (gray to lighter blue).

Figure 28 shows a clear trend of the ice cooling the water inside the squares; the more ice in the square, the colder the surface temperature. This relationship is shown in the apparent temperatures for each of the squares. The average apparent temperatures of the squares with no ice cover were of 2.44 °C (36.4 °F) and 1.39 °C (34.5 °F) (Box 1 and 2), while the average apparent temperature for squares with 50% ice cover were -1.33 °C (29.6 °F) and -1.94 °C (28.5 °F) (Box 7 and 8), respectively, for emulsified and non-emulsified oil. This shows a difference of apparent temperature change of approximately 7 °F degrees from no ice to 50% ice cover regardless of the weathering of the oil. The triangles in each square indicate the point of coldest (blue) and warmest (red) apparent temperatures. The boxes inside the squares were made smaller so that data would not be collected from the very cold edge of the ice sheet surrounding each hole where data were being collected.



UAS Characterization of Oil in Ice – Volume I: Laboratory Results

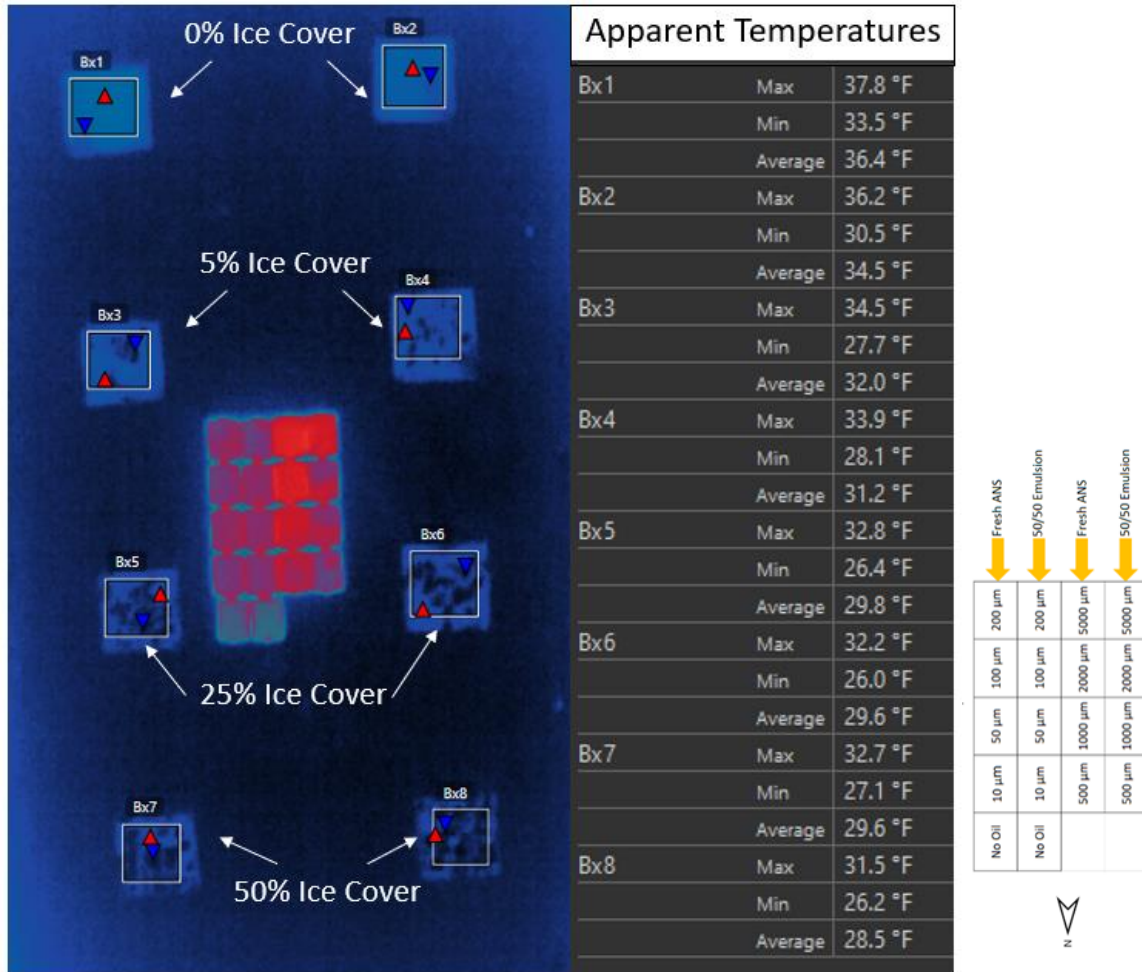


Figure 28. Non-linear bi-color thermal imaging showing apparent temperature of squares with increasing amounts of ice percent cover. Left and right columns are emulsified and non-emulsified oil, respectively.

Apparent temperatures shown in Figure 28 were determined before and after CRREL staff added the 10 mL of oil into the squares. The difference between the highest temperature from Box 2 (no ice, 2.33 °C (36.2 °F)) versus the highest temperature from Box 4 (5% ice, 1.06 °C (33.9 °F)) was 1.27 °C or 2.3 °F degrees. Similarly, the coldest temperature from Box 2 (no ice, -0.83 °C (30.5 °F)) and the coldest temperature from Box 4 (5% ice, -2.17 °C (28.1 °F)) differed by 1.34 °C or 2.4 °F. This means that the difference in temperature was likely controlled by the presence of the ice as opposed to the oil. A similar cooling effect from the ice was observed for 25% and 50% cover. The data suggested that the apparent temperatures detected during thermal analysis when UAS was flown at 30.5 m (100 ft) must be adjusted when calculating oil thicknesses to compensate for the cooling effect of the ice.

Overall, thermal imagery from an altitude of 30.5 m (100 ft) performs well to differentiate between water/oil and ice. This makes it very useful to mask off the pixels related to the solid ice cover and for quantification of percent cover. However, the data also suggest that oil thickness estimations will be challenging, if not impossible, to derive by relying solely on the linear gray scale apparent temperature change in the presence of ice. Furthermore, the presence of ice will result in an underestimation of oil thickness if its cooling effect is not considered.



UAS Characterization of Oil in Ice – Volume I: Laboratory Results

3.1.2.2 Thermal Analysis at 13.7 m Altitude

The purpose of flying and capturing data at different altitudes was mainly to verify if sensors had sufficient spatial resolution to detect variability.

The distribution of oil within the squares was seen more clearly during UAS flights at 13.7 m (45 ft). The oil was especially visible as oil thickness increased. For example, with 200 μm thickness (corresponding to 200 mL of oil added), the oil distribution was not even throughout each square. This may be attributed to the UAS flying too close to the ice surface as a result of wind or the pilot-directed flight pattern. The propeller downdraft (prop wash) created air currents (downdrafts) across the tote's surface, causing a visible non-uniform oil distribution (e.g., accumulation in one part of the tote).

The accumulation of oil in some corners caused the maximum apparent temperatures for different ice amounts to be similar (Figure 29). For example, in the non-emulsified 5% ice cover square (bottom-right), the maximum apparent temperature was 4.61 $^{\circ}\text{C}$ (40.3 $^{\circ}\text{F}$), while the maximum apparent temperature for no ice and the same oil (upper-right) was 4.67 $^{\circ}\text{C}$ (40.4 $^{\circ}\text{F}$). This was not true for the data collected at 30.5 m (100 ft), which was more integrated across a square, lowering the effective overall maximum apparent temperature measured with higher ice cover (Figure 27). For flights at 13.7 m (45 ft), the minimum and average apparent temperatures were lower in the 5% cover squares (Figure 29). Despite the issues with the propeller downdraft, the results from the two altitudes were similar (e.g., decreasing apparent temperatures at higher ice concentrations) (Figure 28) indicating the sensors had sufficient spatial resolution to detect variability.

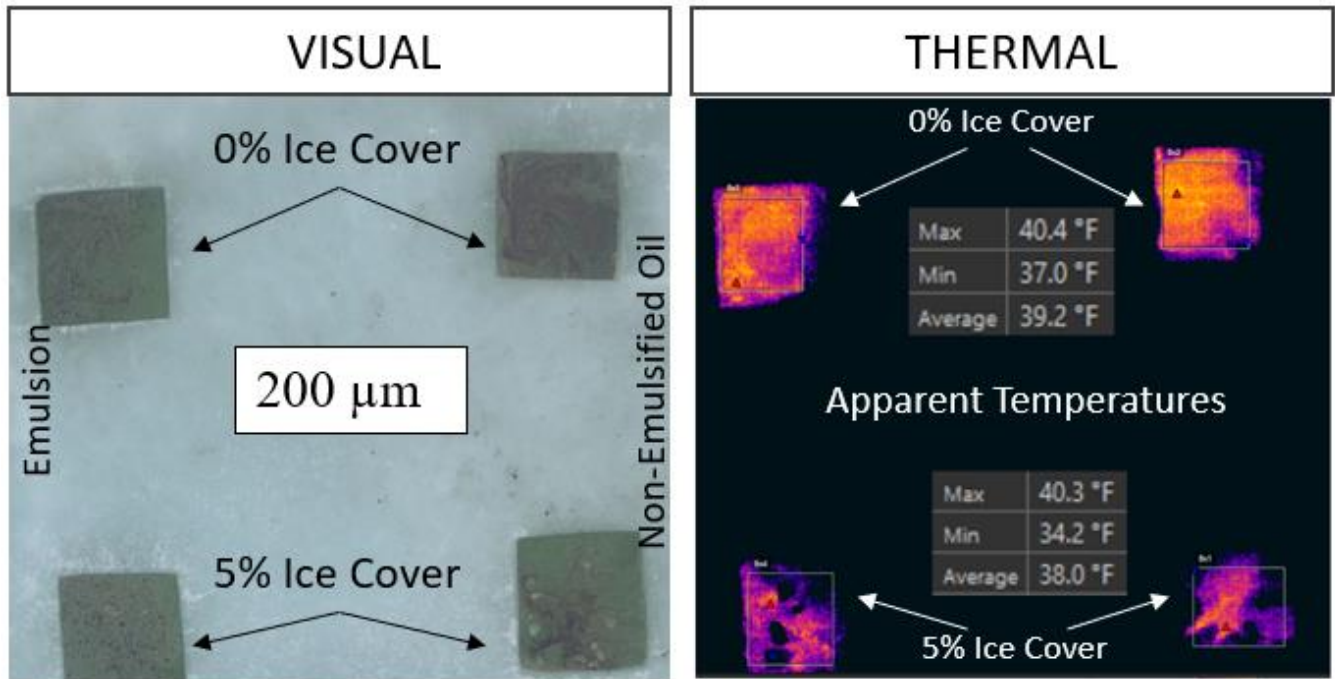


Figure 29. Visual vs. non-linear bi-color thermal images taken at 13.7 m (45 ft) (200 μm thickness, 0-5% ice cover). Apparent temperatures for non-emulsified oil.



UAS Characterization of Oil in Ice – Volume I: Laboratory Results

The ice also cooled the squares with higher quantities of oil (1,000 μm) and greater ice cover (Figure 30). CRREL staff applied non-emulsified oil to the bottom-right (50% ice cover) and top-right (25% ice cover) squares. A non-linear bi-color scale differentiated the ice, water, and oil, and captured how apparent temperature changed with thickness. The spreading on the 25% square was more uniform, whereas oil aggregated in a smaller area in the 50% square, resulting in a thicker slick. The uneven distribution of oil caused the bottom right square to have cooler apparent temperatures and a darker color.

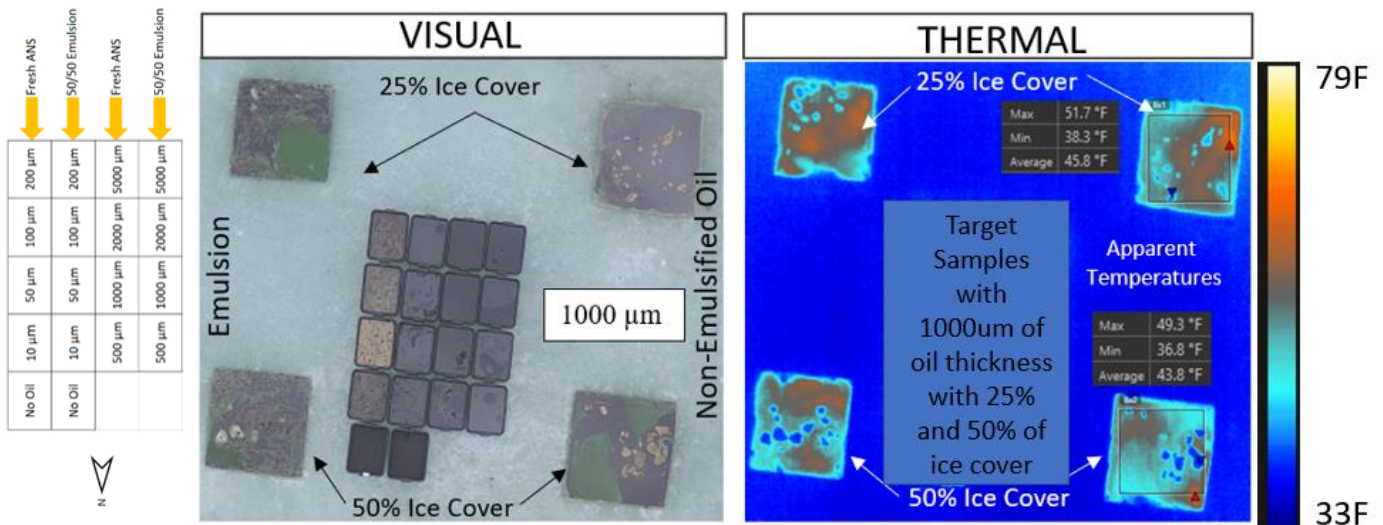


Figure 30. Comparison of visual vs. thermal images on higher quantities of oil.

The presence of more ice affected the apparent temperature readings of the oil, and skewed the oil thickness measurements. The square on the bottom right had a thicker layer of oil, however, this was not reflected as a warmer apparent temperature because greater ice concentration decreases the temperature.

The totes on the center of the GRF tank, provided another way to measure the variability of the apparent temperature of the oil as a function of oil thickness. Figure 31 shows the visual true color of the totes, the thermal view, and range of apparent temperatures inside each tote during Flight 4 (time 0834, overcast conditions). Box 1 (water only, non-emulsified oil) had an average apparent temperature of 9.28 °C (48.7 °F), while the 10 μm tote (Box 2, non-emulsified oil) had an apparent temperature of 10.4 °C (50.8 °F). The apparent temperatures of the boxes inside the non-emulsified totes increased with oil thickness until reaching a maximum temperature of 13.1 °C (55.5 °F) for the box with 5,000 μm of oil (Box 6).



UAS Characterization of Oil in Ice – Volume I: Laboratory Results

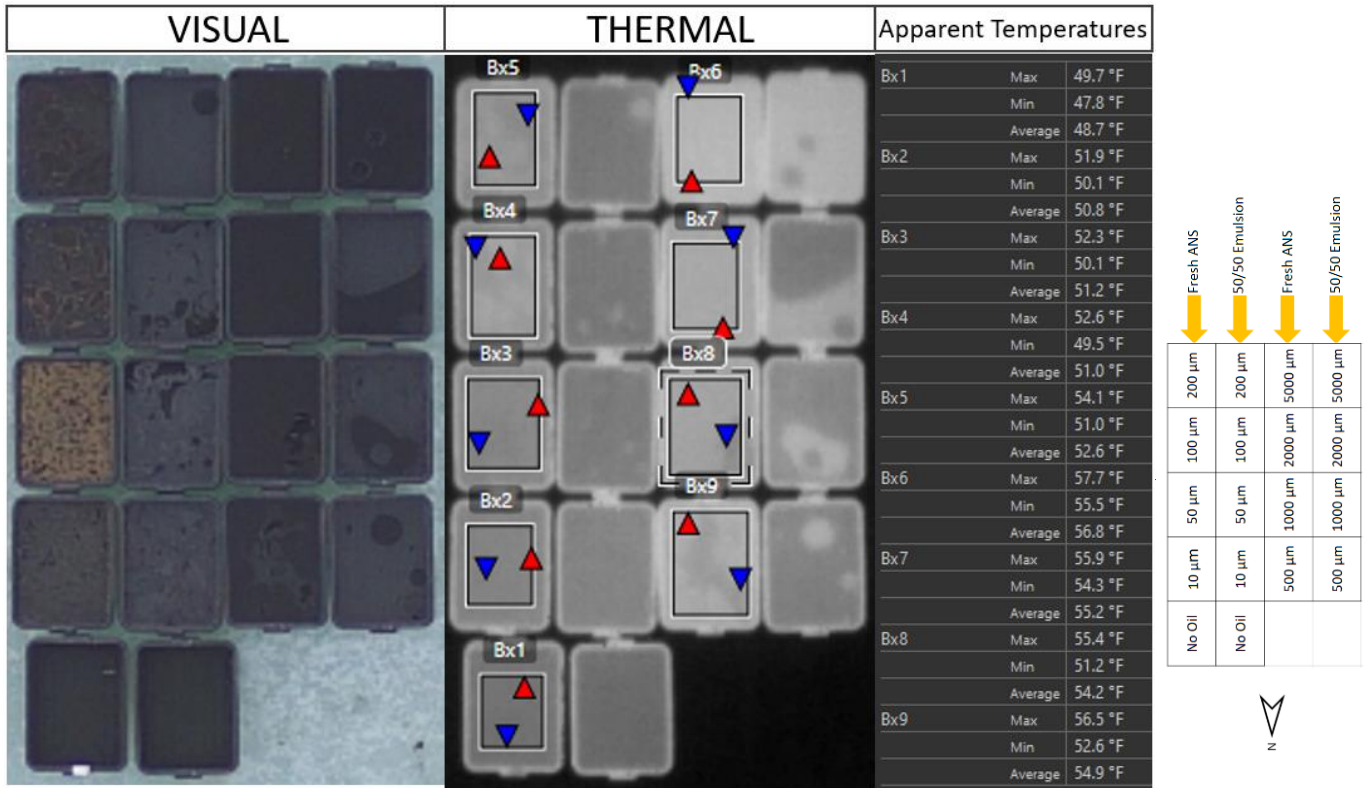


Figure 31. These measurements show the maximum (red triangle), minimum (blue triangle), and average of the apparent temperatures inside the totes (Boxes 1 through 9).

The maximum, minimum, and average apparent temperatures of the totes were compared among flights. During Flight 4 (Figure 32) the project team collected data at 0834 under overcast sky conditions and limited solar radiation. These low illumination conditions were chosen for analysis because they represented the most challenging scenario; the thermal radiation from the sun was low enough so that the range in apparent temperature readings was ~7 °F. Figure 32 demonstrates that under the conditions experienced during Flight 4, one can detect changes in the oil thickness for slicks ≤500 μm. The thermal radiation of thickness greater than 500 μm showed very little variation. Early in the day, the sun had not warmed the thicker oil layers and their reflective apparent temperatures were similar to thinner oil layers.



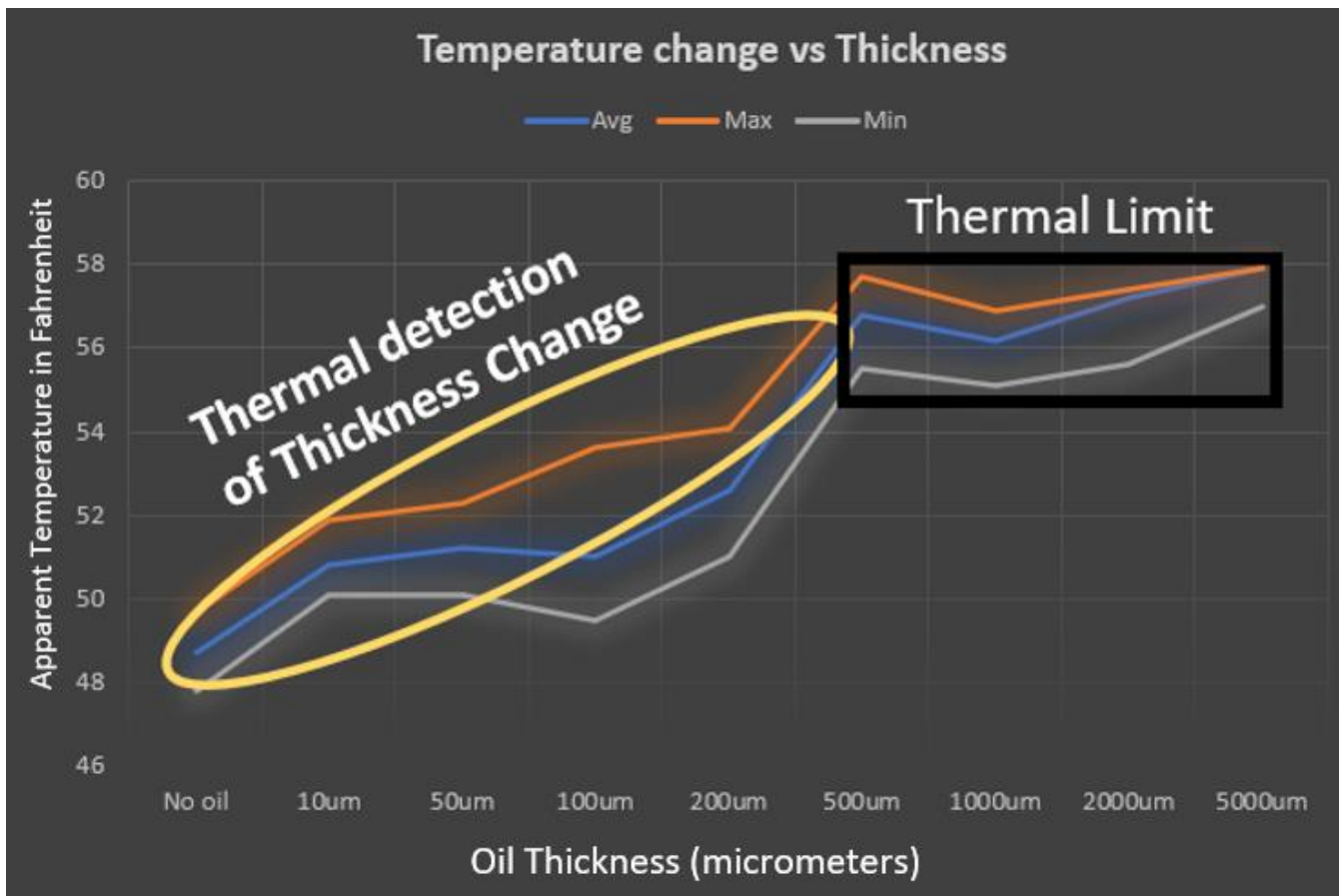


Figure 32. Comparison of maximum, minimum, and average of apparent temperature observations for the totes vs. oil thickness during Flight 4 at 8:34am under overcast skies and limited solar radiation.

UAS Flight 7 took place later in the day (1134) and more solar radiation was available to heat the oil. Skies were still overcast, but light from the sun could be seen reaching the totes indirectly. Under these conditions, the variations in oil thickness were more discernable (Figure 33) and the tailing effect above 500 μm was not seen. Instead, the project team noted a steady increase in apparent temperature of the oil from a thickness of 2,000 μm to 5,000 μm. The linear relationship indicated the apparent temperature on the totes increased 1.22 fold starting at 9.94 °C (49.9 °F) as the thickness of the oil increased:

$$A_T = 1.2167 \ln(O_T) + 48.624 \text{ (Equation 1)}$$

where A_T is the apparent temperature (°F) inside a tote and O_T represents the corresponding oil thickness (μm). This linear relationship only applies for the conditions present at the time these multispectral images were taken. Stronger thermal radiation (images taken later in the day or with fewer clouds) will increase the separation on the apparent temperature values of the thicknesses. Similarly, as seen earlier in the morning (Figure 32), less thermal radiation produced less contrast and it may reach an inflection point above which apparent temperature changes little with increasing oil thickness.



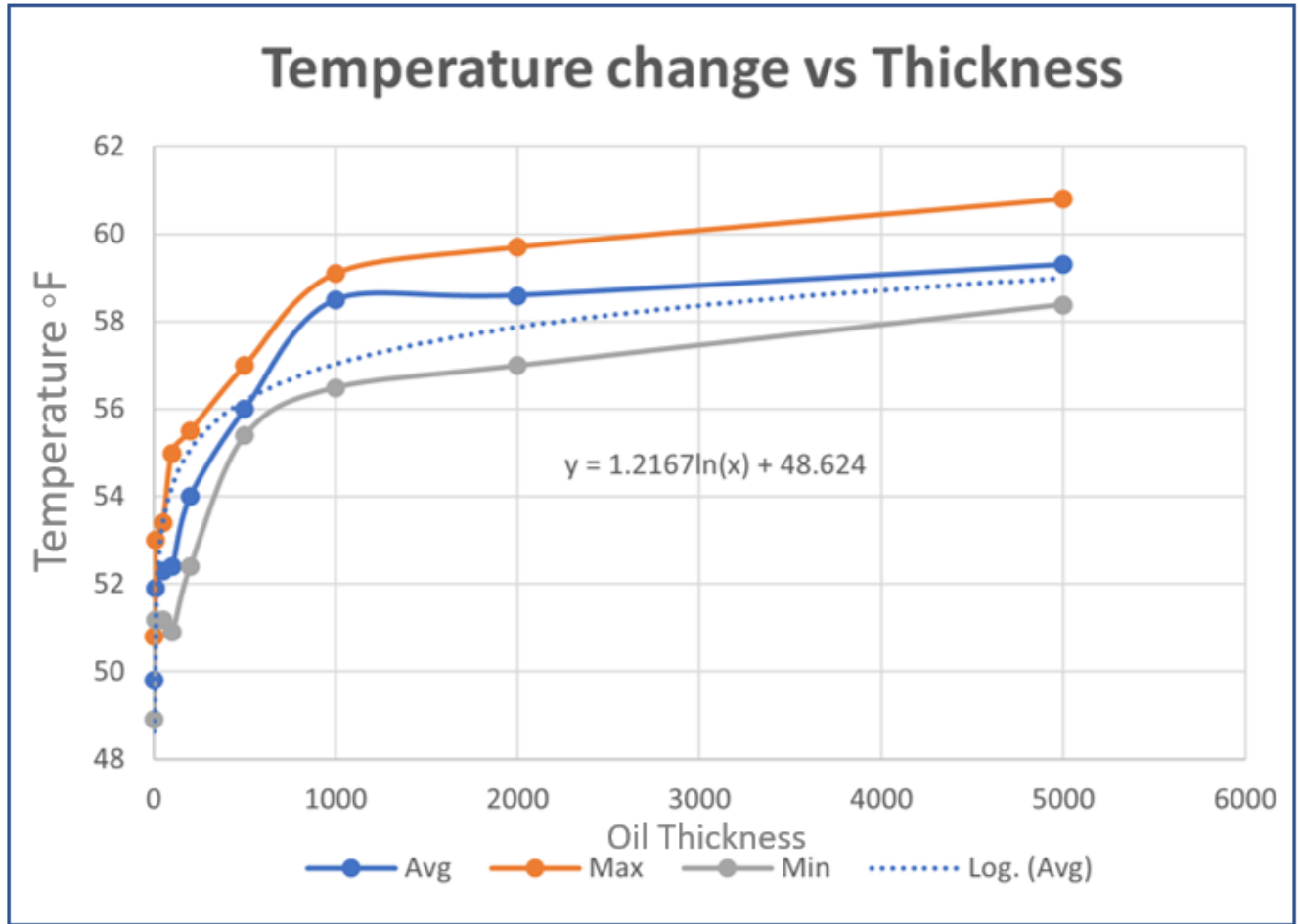


Figure 33. Apparent temperature change vs oil thickness for Flight 7 at 11:34am under overcast skies, but with more solar radiation.

The radiation at mid-day produced (even for overcast conditions) produced a difference of 24 °F between the ice and thickest oil, while early in the morning there was only a 10 °F temperature difference. Figure 34 shows a thermal view of the highest contrast in apparent temperature between the 2,000 μm thick oil and ice during Flight 9 at 1433 local time on April 20 during a window of sun exposure. Even a limited amount of direct sunlight over the totes produced a much higher thermal contrast among the oil thicknesses and ice.



UAS Characterization of Oil in Ice – Volume I: Laboratory Results

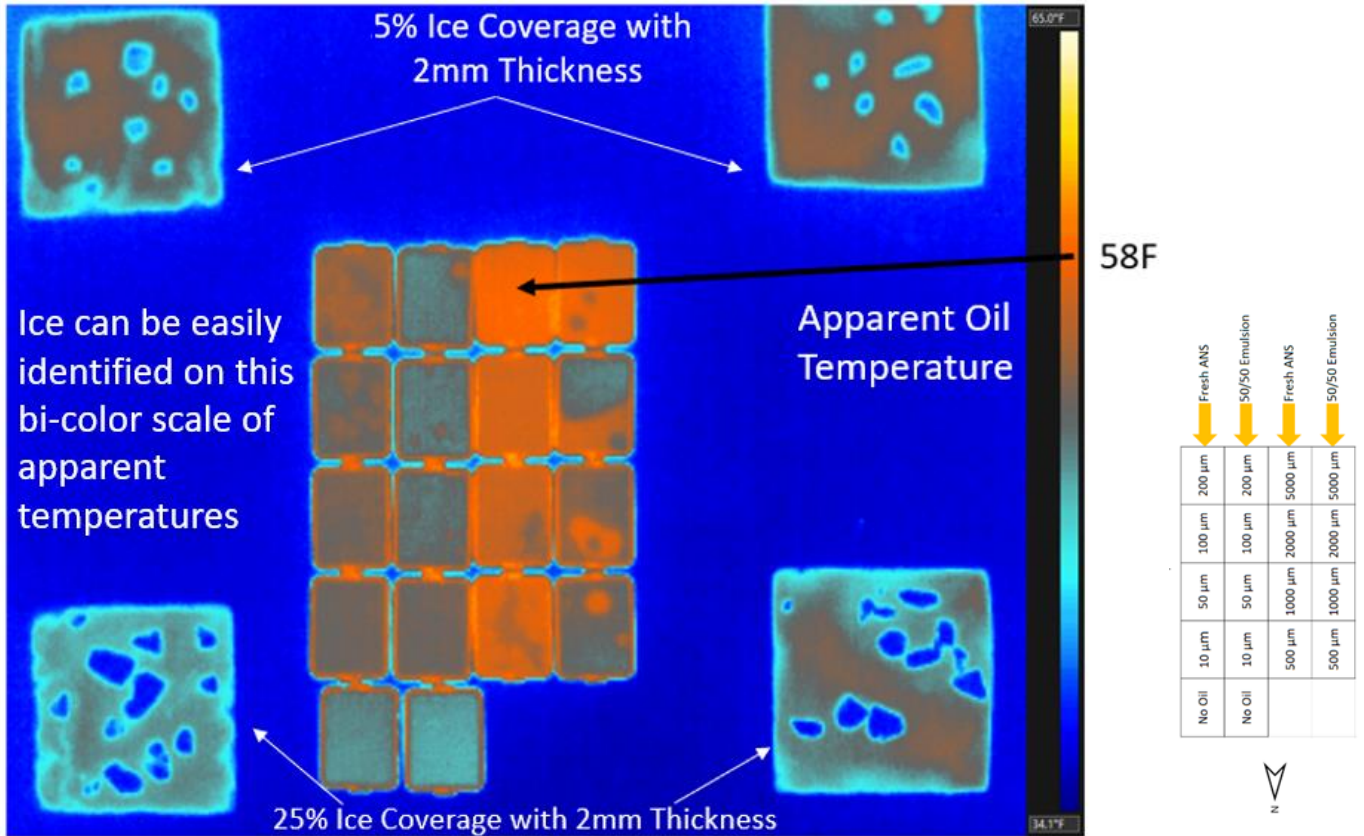


Figure 34. Thermal view of the highest contrast in apparent temperature between the 2,000 μm thick oil and ice for Flight 9 during sun exposure.

During the nine flights at 13.7 m (45 ft), the non-emulsified oil produced higher apparent temperatures than the emulsified oil regardless of the time of the day (e.g., Figure 35).

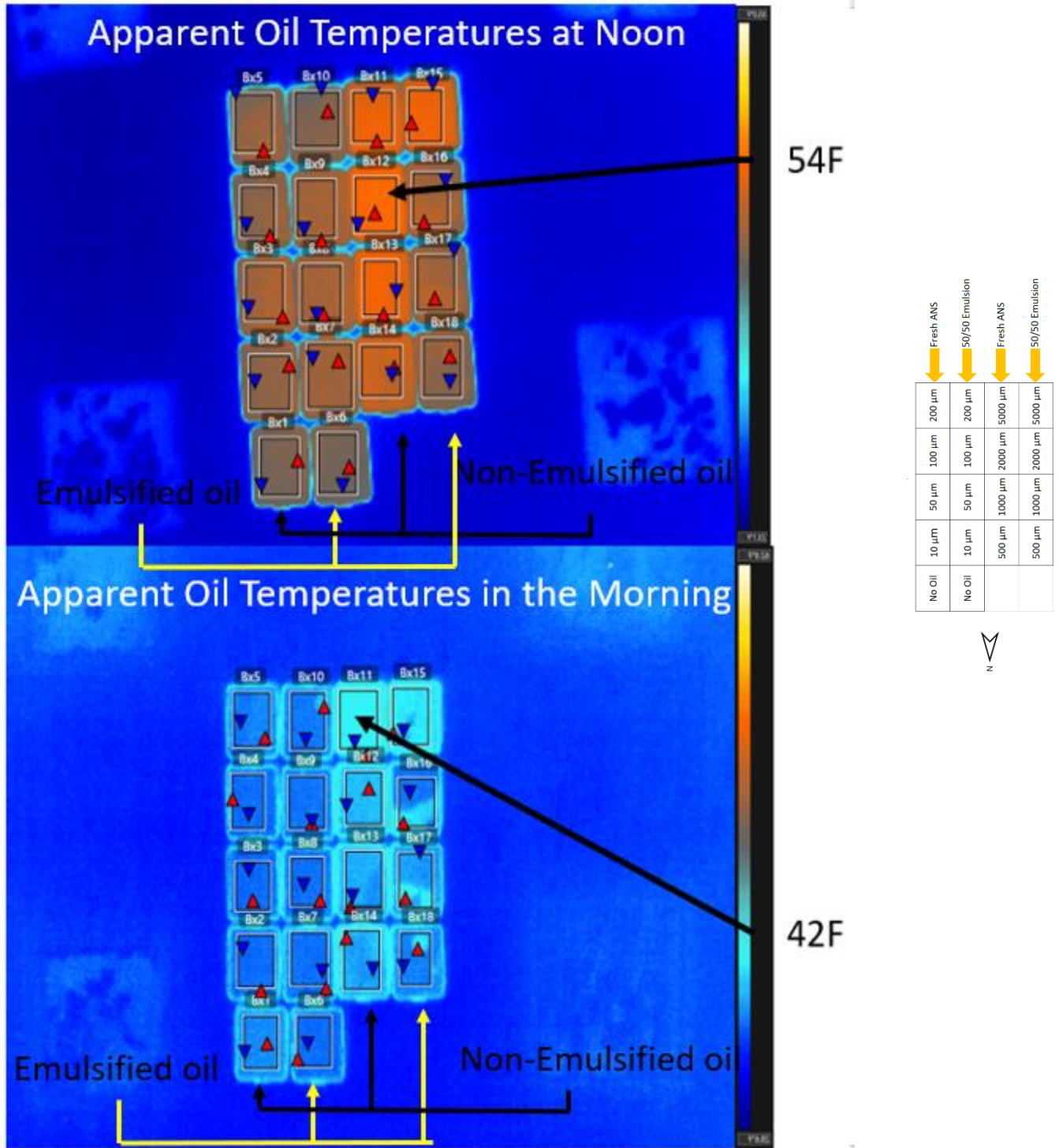


Figure 35. Analysis of apparent oil temperatures from non-emulsified oil vs emulsified oil. Early morning flight at 07:45am.

3.1.3 24-Hour Time Lapse of Multispectral and Thermal Imagery

The project team collected more than 5,000 digital multispectral, visual, and thermal photos during the 24-hour time lapse experiment. It received thermal imagery using a Forward Looking Infrared (FLIR) camera that was calibrated for the collection of relative apparent temperature data on each pixel in the image. To process and analyze the time lapse data, an algorithm was generated that batched the images to process them semi-automatically. This algorithm extracted the apparent temperature data from manually-selected locations and targets. These targets included areas within the totes where variations in thermal radiance could be visually detected with respect to variability of the oil thickness. Additional targets were selected within the area of the 1m x 1m squares to compare different oil thicknesses and emulsifications with ice and water. The apparent temperature values were compiled on data processing software and used for statistical analysis. Figure 36 shows an example of the thermal imagery.

One of the purposes of this experiment was to identify if thermal reflectivity of different oil emulsification ratios (e.g., non-emulsified, 50:50 and 30:70 emulsified) would produce a different response or detection over the course of the day.



UAS Characterization of Oil in Ice – Volume I: Laboratory Results

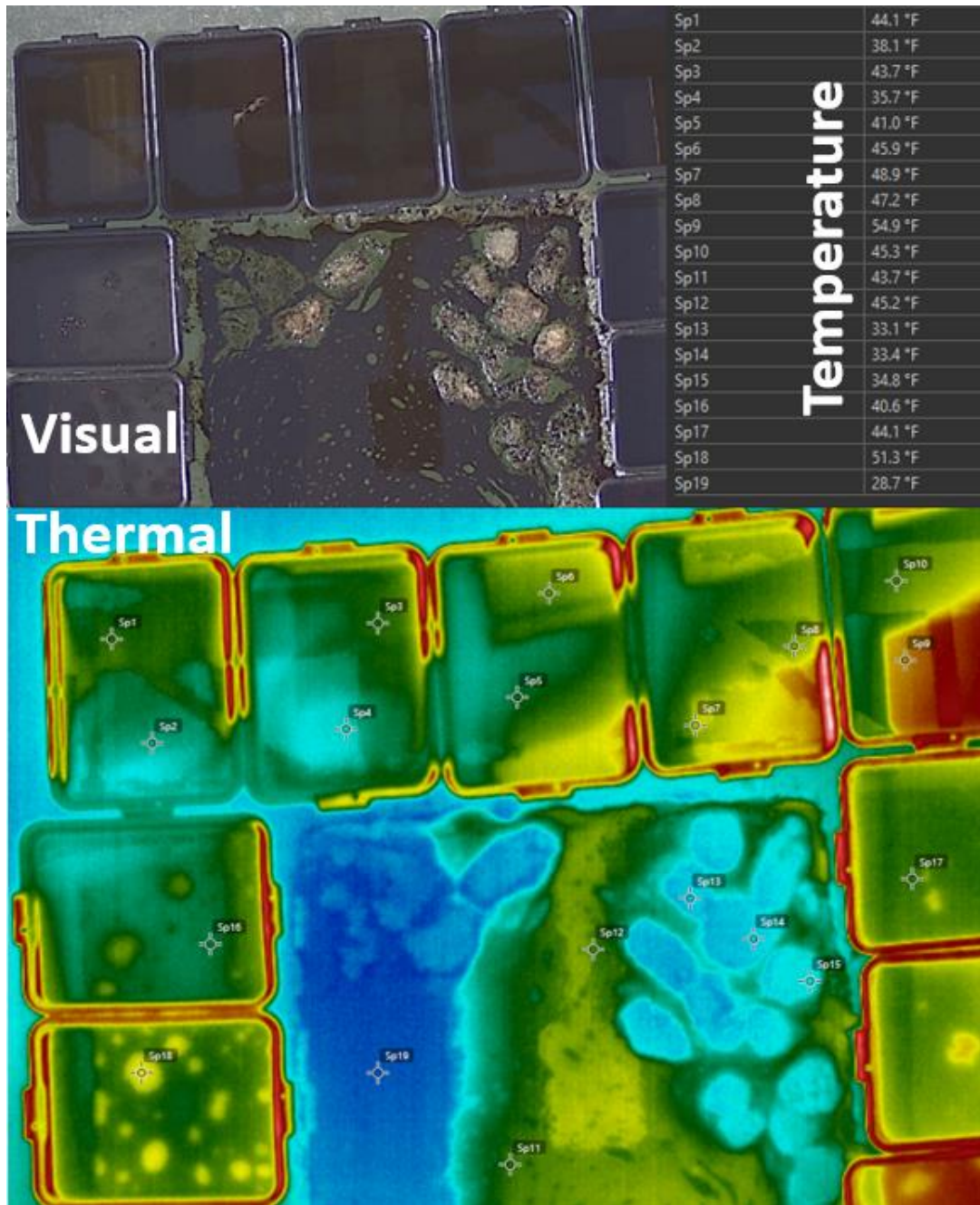


Figure 36. Example of difference in imagery obtained from the visual versus thermal sensors. The top photo is a visual RGB image in which little can be discerned much about the variation in oil thickness as opposed to the apparent temperature data in the bottom image.

The positioning of the A-Frame holding the sensors above the totes allowed direct sun exposure and some shading (indirect sunlight). However, the camera was not perfectly aligned with the totes. This occurred because it was difficult to position the camera on the A-Frame from ladders positioned on the ice sheet. This is the reason for the skew in the images in Figure 36. Despite this, the project team was able to collect a sufficient amount of data from the totes. Volume II of this RDC report, “UAS Characterization of Oil in Ice



UAS Characterization of Oil in Ice – Volume I: Laboratory Results

– Volume II: Supplemental Laboratory Data” summarizes apparent temperature readings every 15 minutes for the 24 hours.

Figure 37 shows a plot of the apparent temperatures for the oil targets inside the totes as a function of time. It also shows the emissivity (relative apparent temperature) properties for thicknesses and oil types where the camera was able to capture images. The effect of the sun crossing overhead, setting, darkness, dawn, sunrise and the sun again crossing overhead is clear in the apparent temperature pattern over the 24-hr time lapse from noon to noon.

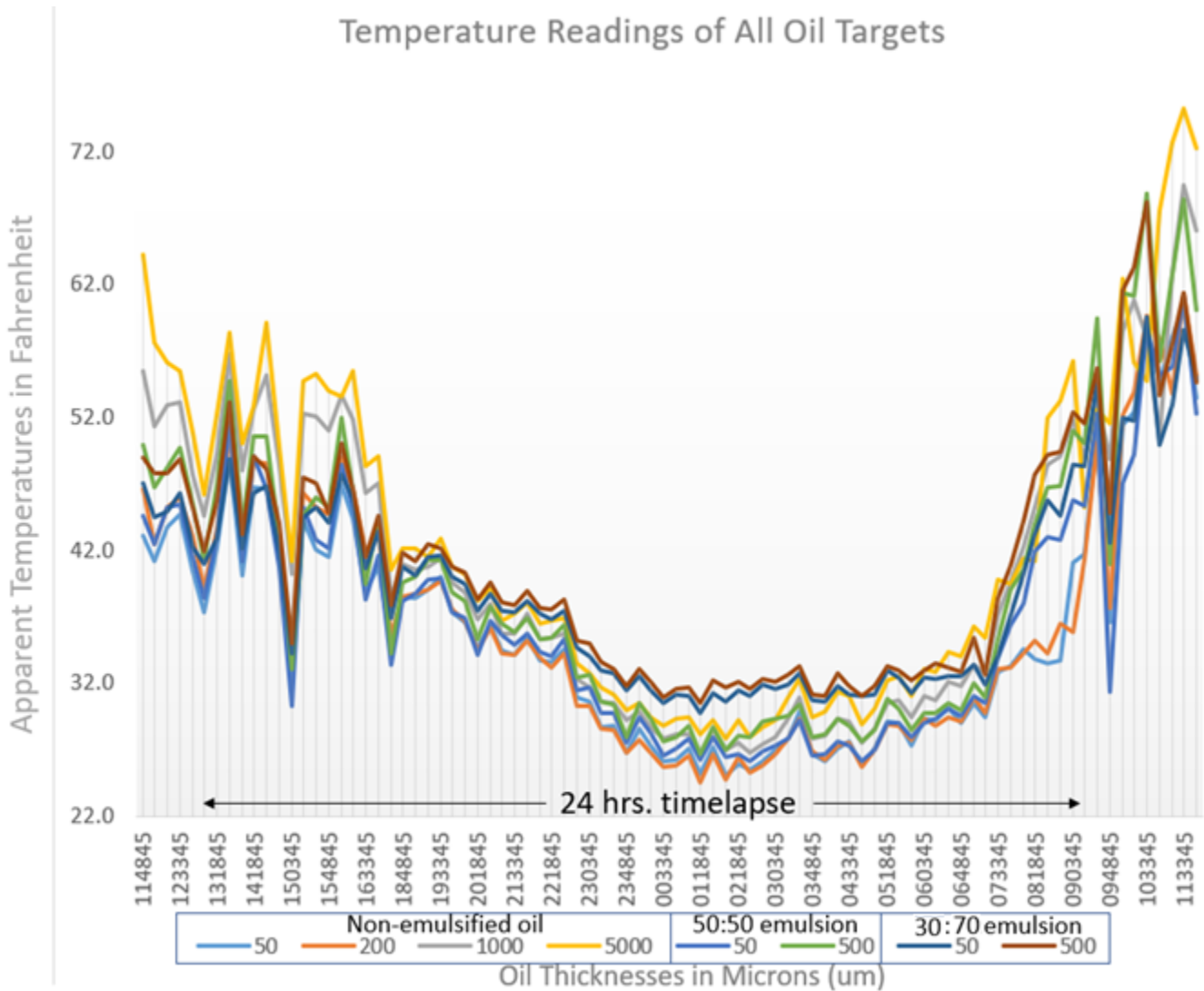


Figure 37. Thermal readings from the 24-hour time lapse of oil thicknesses for the totes. Each point is the average of apparent temperature readings every 15 minutes.

For subsequent discussion, only the non-emulsified data is used but the pattern in the apparent temperatures for the emulsified oil (50:50, 30:70) was similar. Apparent temperature readings from the 24-hr time lapse of non-emulsified oil shows the effect of the thicker oil on the thermal radiation reflectivity under these cold ‘Arctic’ conditions (Figure 38). While the thermal difference between 50 and 200 μm of oil thickness was minimal (maximum difference of 4 $^{\circ}\text{F}$), the difference between 50 and 500 μm , 50 and 1000 μm and 50 and



UAS Characterization of Oil in Ice – Volume I: Laboratory Results

5000 μm reached 13 °F, 18 °F, and 25 °F, respectively. 50 μm was used as a reference because it is typically the threshold for ‘actionable oil’. This is similar to the quasi-linear relationship observed for the totes during the thermal analysis performed at 13.7 m (45 ft) (Figure 33).

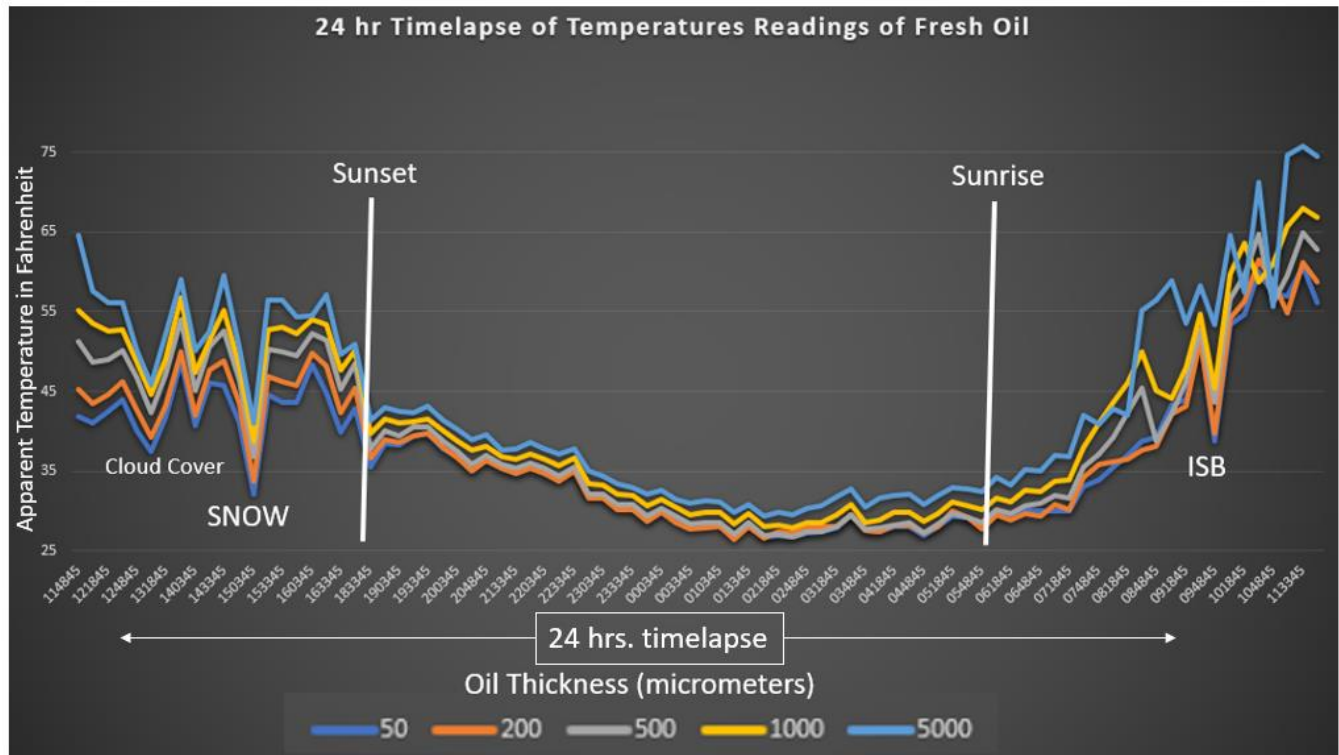


Figure 38. Apparent temperature readings of non-emulsified oil over a 24-hour time lapse.

The apparent temperature readings for oil slicks measuring between 50 μm and 200 μm were very similar, indicating that the capacity to discern thicknesses in this range, may be limited. There are several reasons for this limitation. For example, thin oil slicks tend to be more susceptible to surface water effects and are much more unstable. This introduces uncertainty to oil thickness estimates and unexpected oil behavior. Another reason for the lack of thermal discernibility in thin oil slicks is the spectrum of the sensors used in this experiment, which limited the ability to resolve the differences between them.

Figure 38 shows the low apparent temperature reading at night from snowfall during the evening of April 22. Before the snow, the project team captured the effects of dense, cloudy conditions when solar radiation was drastically reduced. Sunset and sunrise were also very apparent, and during the night there was a tailing off of the signal and a minimal difference in the apparent temperatures for the oil, regardless of thickness. Figure 38 shows that the oil began to warm after the sun rose, slowly at first and then rapidly.

The thermal readings of non-emulsified oil, and 50:50 and 30:70 emulsions were similar for the same thicknesses (Figure 39). The water molecules in the 30:70 emulsion produced a radiation inversion as the sunlight disappeared at night indicating that highly emulsified oil may have a greater apparent temperature when light levels are low to non-existent in the Arctic. This effect is also known as thermal crossover. For example, the 30:70 emulsified oil yielded higher reflectance at night compared to the 50:50 emulsified and the non-emulsified oils.



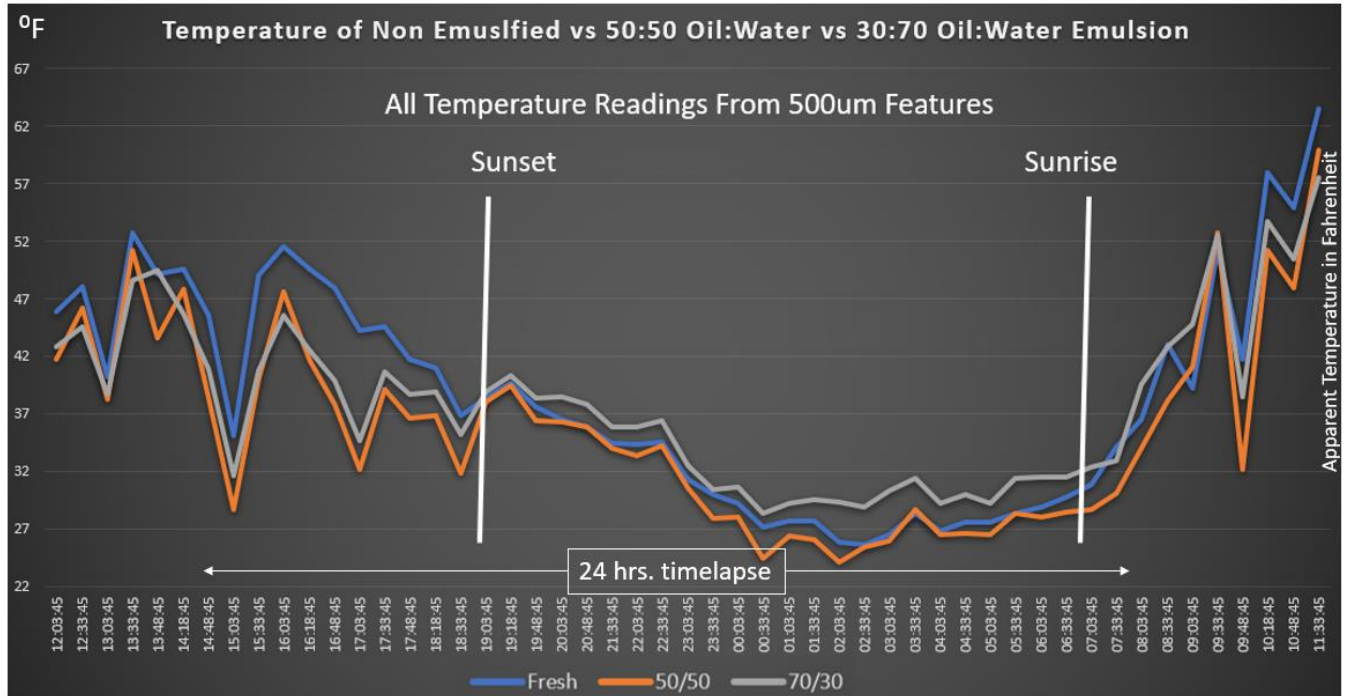


Figure 39. Apparent temperature of non-emulsified vs 50:50 oil-water vs 30:70 oil-water emulsion.

3.1.4 Synchronous and Comparison of Observations from Aerial (UAS) and Underwater (ROV)

The ROV-based acoustic sensors collected underwater measurements of the floating oil inside the squares while UAS sensors collected thermal and multispectral measurements. The overlap in the range of thicknesses that these technologies can measure is small. While the UAS sensors became saturated at thicknesses >1,000 μm, the ROV acoustic system showed it performed best at 700 μm. The best overlap with the concurrent data occurred with the 2,000 μm thick slick with 5% ice. Figure 40 shows an aerial image (visual and thermal) of the squares during the 2,000 μm sampling cycle.



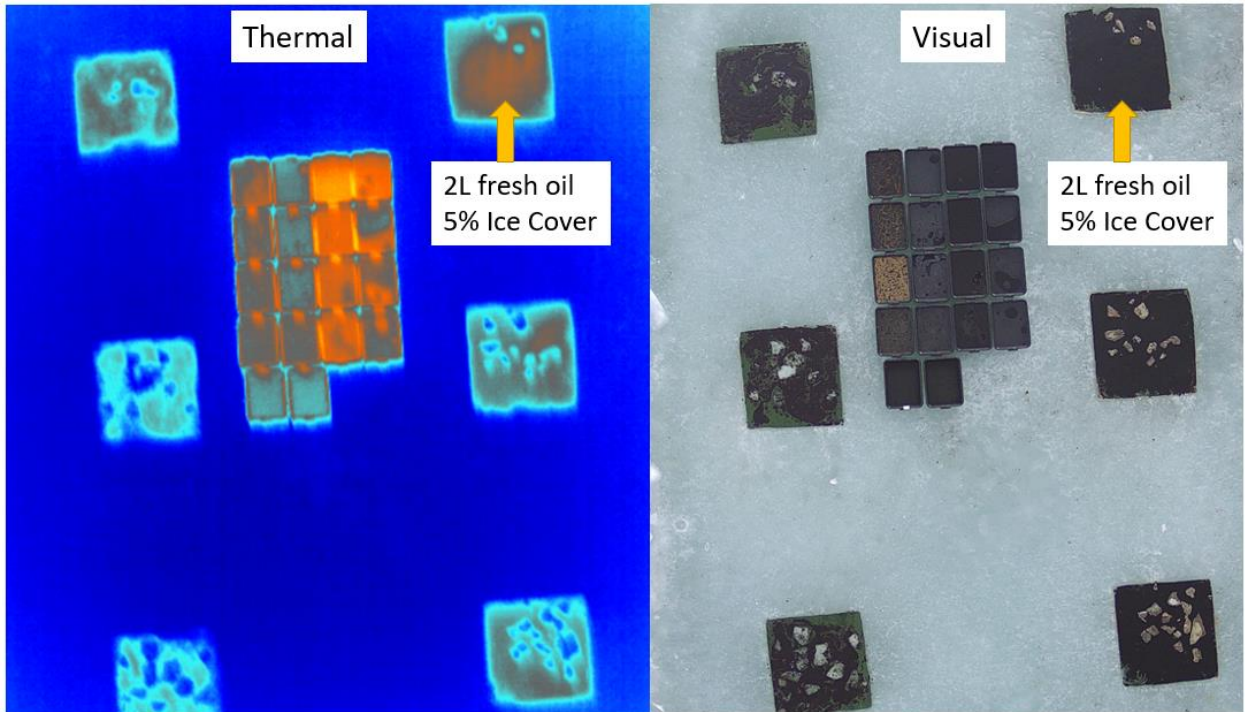


Figure 40. The upper right square was used for comparison of synchronous data collected by the UAS and ROV. This square corresponds to 5% ice cover with 2 L of oil on it.

Using thermal data, Figure 41 indicates that a large number of pixels with very thin sheens were detected (mostly at one edge of the square), and minimal number of pixels reached thicknesses $>3,000 \mu\text{m}$. The average thickness was $1,304 \mu\text{m}$ and the estimated volume was $1,516 \text{ mL}$. These results were consistent with previous calculations of thicknesses above the saturation point for the thermal sensor.

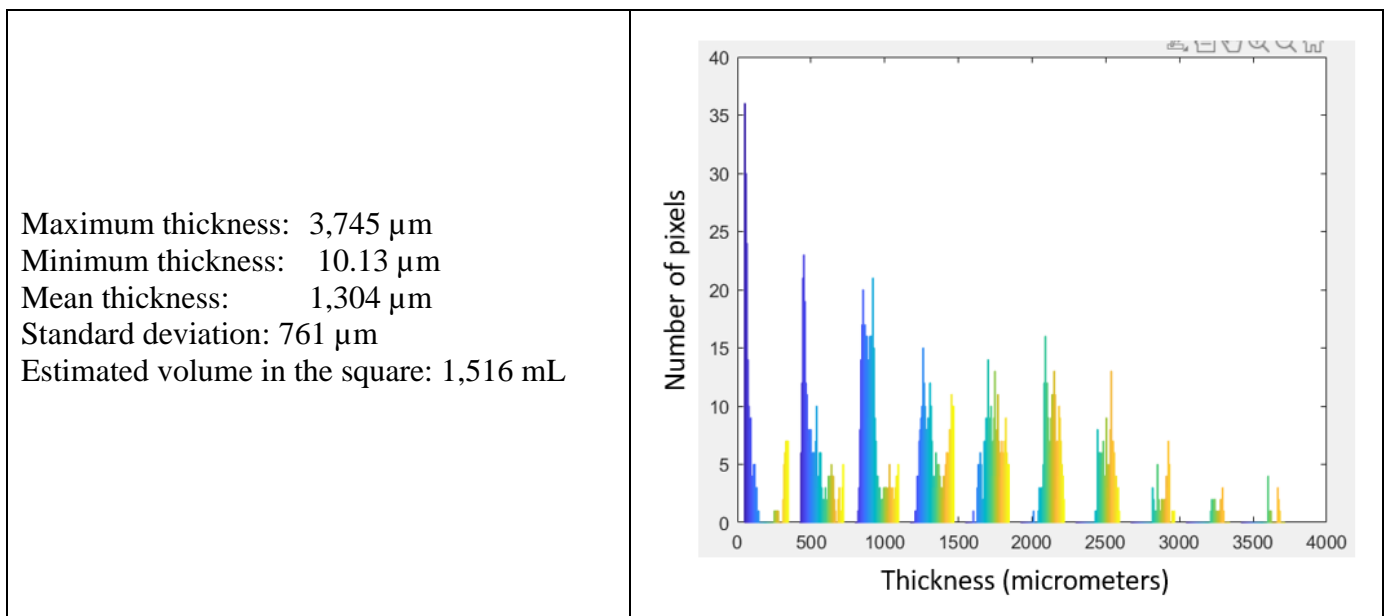


Figure 41. Statistics from the thermal data including the frequency of sheen thicknesses for the test square.

UAS Characterization of Oil in Ice – Volume I: Laboratory Results

The ROV-based acoustic sensors sampled the square with the 2,000 μm slick and 5% ice for 30 seconds. Figure 42 shows the resultant thickness measurements. The UAS thermal and the ROV acoustic measurements reported a similar average with the UAS thermal measuring 1,300 μm and the ROV acoustic measuring 1,500 μm . Table 6 shows the comparison of the results from the UAS and the ROV technologies.

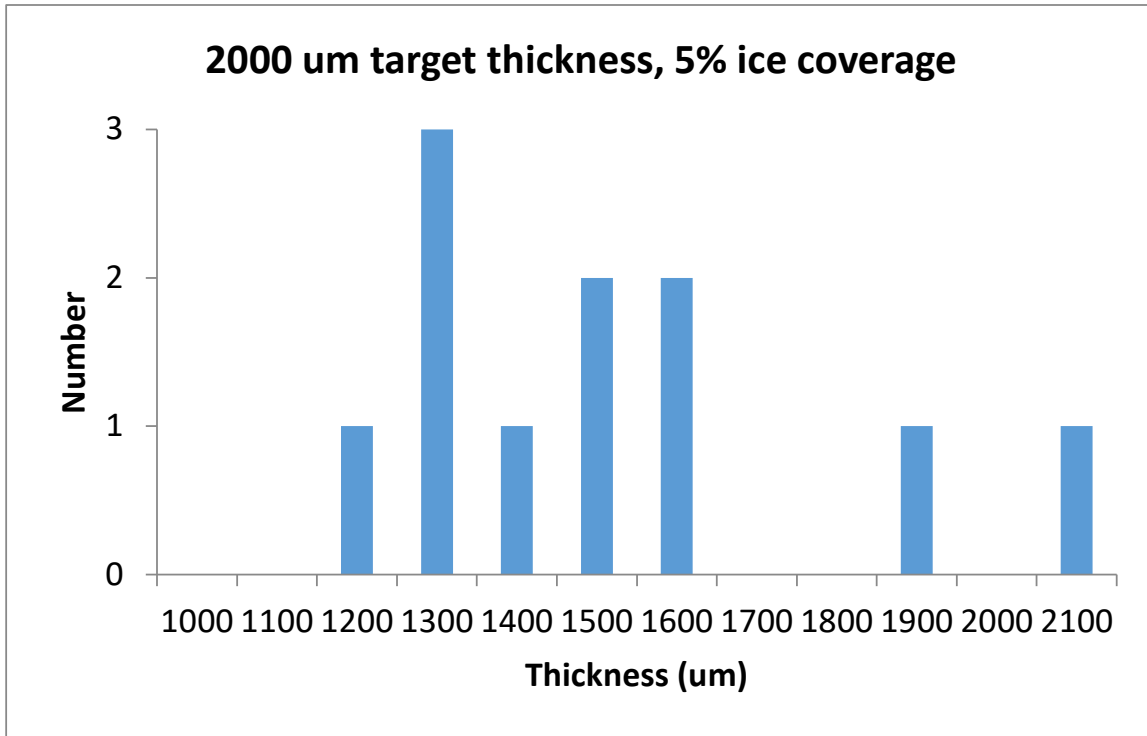


Figure 42. ROV-based acoustic measurements of the thickness of oil in 5% ice covered square with target thickness of 2,000 μm .

Table 6. Comparison of acoustic and thermal sensor thickness estimates for 2,000 μm and 5% ice.

	UAS (Thermal)	ROV (Acoustic)
Average (μm)	1,304	1,500
Std. Dev. (μm)	761	300
Maximum (μm)	3,745	2,100
Minimum (μm)	10	1,200
Range (μm)	3,735	800

Both methods computed an average below the target thickness of 2,000 μm . This deviation from the true thickness suggests that the amount of oil inside the square may be affected by physical processes. For example, evaporation, the accumulation of oil at the edges of the square, or the enlargement of the square due to ice melt at the edges may cause the slick to thin. Overall, the closeness of the measurements from the two technologies is encouraging.

Additional data was collected on isolated squares of oil and ice where the oil was added to increase the thickness of the slick. In those cases, the direct sampling using the tube sampler and the ROV-based acoustic sensors also provided similar results (Figure 43, Table 7).



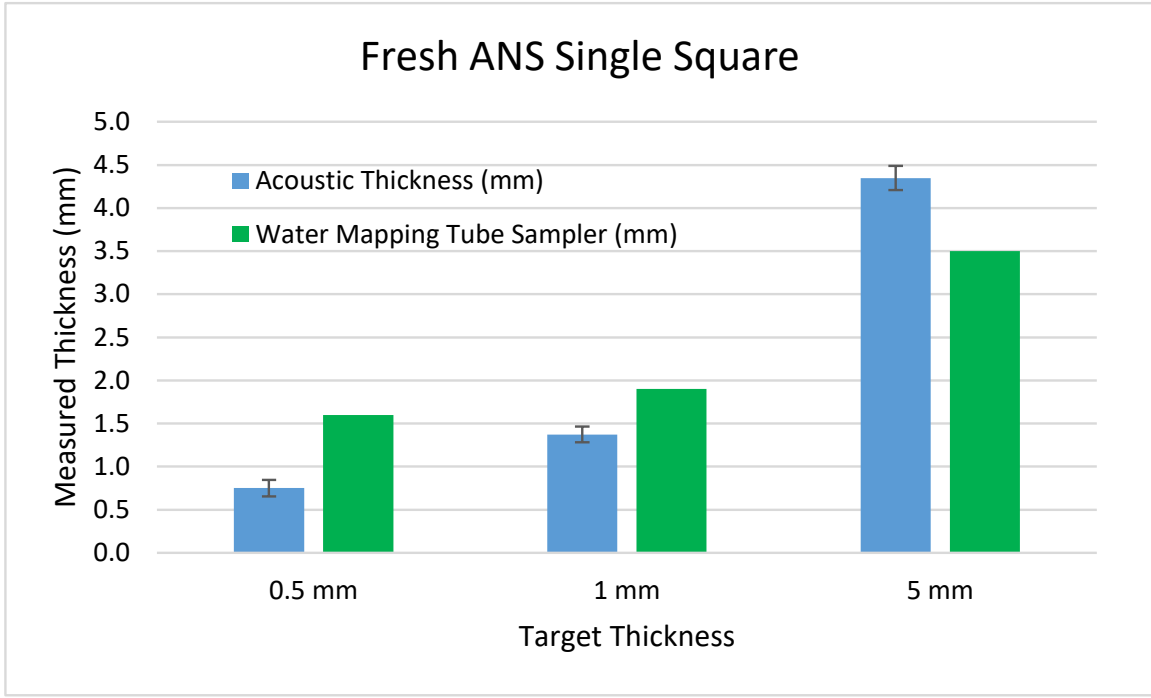


Figure 43. Comparison of the acoustic sensor thickness estimates and Water Mapping’s tube sampler for a range of oil thicknesses.

Table 7. Comparison of the acoustic sensor thickness estimates and Water Mapping’s tube sampler for a range of oil thicknesses.

Acoustic measurement of thickness			
Fresh ANS Single Square	0.5 mm	1 mm	5 mm
Average (mm)	0.75	1.4	4.3
Std. Dev. (mm)	0.28	0.5	1.0
Maximum (mm)	1.36	2.9	5.8
Minimum (mm)	0.31	0.9	2.3
Range (mm)	1.05	2.0	3.5
Number	9	33	48
Std. Error (mm)	0.094	0.09	0.14
Water Mapping Tube Sampler (mm)	1.6	1.9	3.5

This experiment demonstrated that the two technologies are complementary. The UAS will perform better on thinner slicks (< 1,000 μm) and the ROV with acoustic sensors will perform better on thicker thicknesses (>1,000 μm).

3.2 Minimum Detection Limit

It is important to the FOOSC to know the minimum detection level of the sensors for Arctic conditions so they can have a better understanding of detection/characterization range if using those sensors. The project



UAS Characterization of Oil in Ice – Volume I: Laboratory Results

team determined the minimum detection levels of the multispectral and thermal sensors using CRREL data to differentiate between emulsified and non-emulsified oil and determine oil thickness, respectively.

3.2.1 Minimum Detection Limit of Oil in Cold Waters without Ice

Detection limits of oil are different for thermal sensors used in temperate vs. Arctic conditions. The background of a thermal image of oil on water is the apparent temperature of the water. The oil produces a distinct contrast, if it is thick enough, due a change in its apparent temperature compared to the temperature of the water. This temperature difference must exceed some threshold in order to detect the oil. This detection limit changes depending on the temperature of the water and the heat potential from the ambient illumination conditions from the sun. Thinner oil layers will be detected more easily on temperate waters on a summer day at noon because the apparent temperature contrast will be at its maximum. The opposite would happen on Arctic waters with significant ice cover and limited illumination because the thermal contrast between oil, water, and ice will not be as high. Hence, it will be harder to detect thickness variation in colder waters.

3.2.2 Minimum Detection Limit of Oil in Cold Waters with Ice

In the CRREL experiments, the thermal imagery did not detect changes in apparent temperature for 10 μm or 50 μm (Figure 44 shows 50 μm case), even with the least amount (5%) of ice for either emulsified or non-emulsified oil.

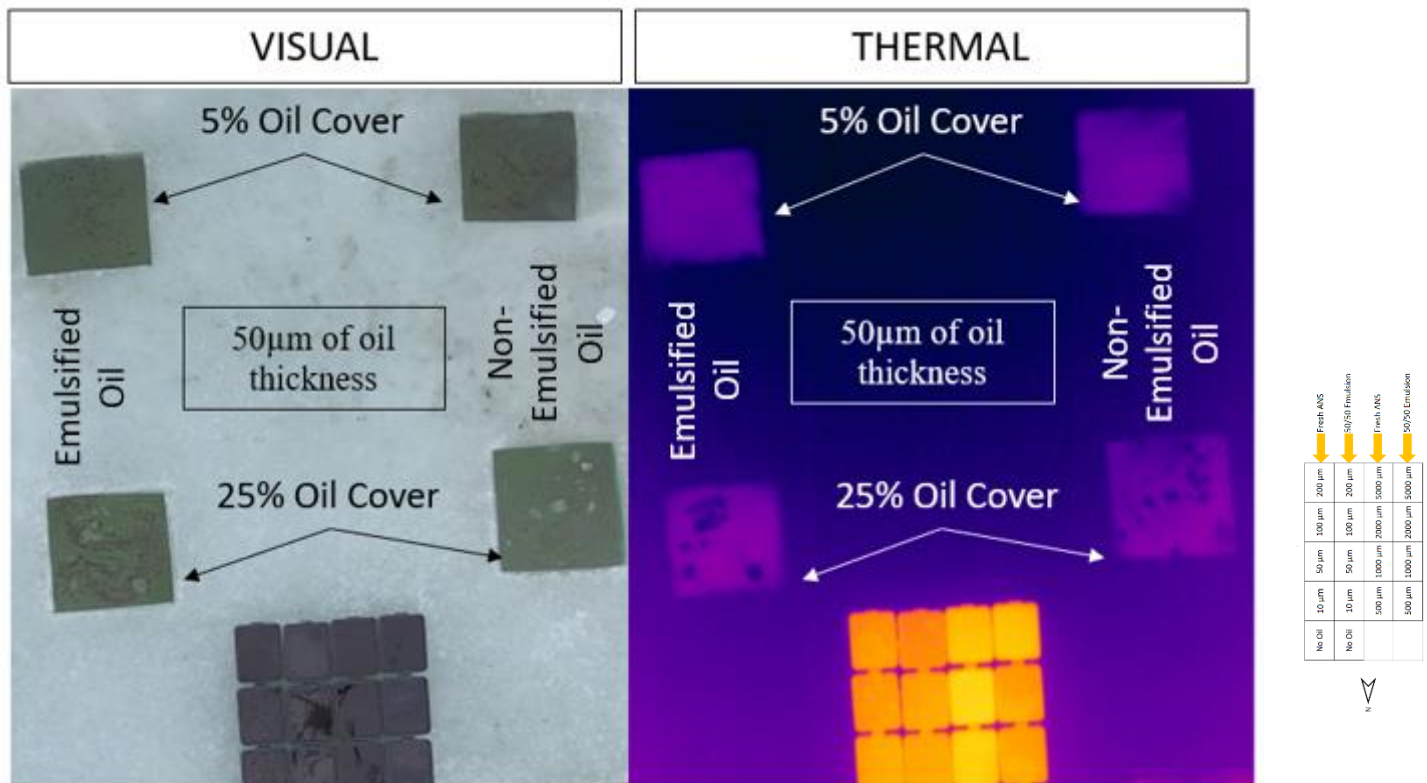


Figure 44. Aerial view from the squares set with 50 μm of oil.



UAS Characterization of Oil in Ice – Volume I: Laboratory Results

Small strings and patches of oil were visible inside the squares with no ice (not shown) and 5% ice and 50 μm (left of Figure 44), but there was no change in the apparent temperature. For comparison, there was a clear thermal signal in the totes containing no ice and 50 μm of oil. There was some variability in the apparent temperatures (Figure 31), there was little to no visual change between totes with 0, 10 and 50 μm of oil.

Figure 45 shows that a thermal signature is detectable in the 100 μm squares. The squares shown in Figure 45 are the same as the ones shown in Figure 44 with the only difference being the increase in oil thickness from 50 to 100 μm . Apparent temperatures on the 100 μm square with 5% ice were recorded as 3.83 $^{\circ}\text{C}$ (38.9 $^{\circ}\text{F}$) for thicker oil (Sp1), 3.0 $^{\circ}\text{C}$ (37.4 $^{\circ}\text{F}$) for the thinner oil (Sp2), and 0.89 $^{\circ}\text{C}$ (33.6 $^{\circ}\text{F}$) for the ice (Sp3).

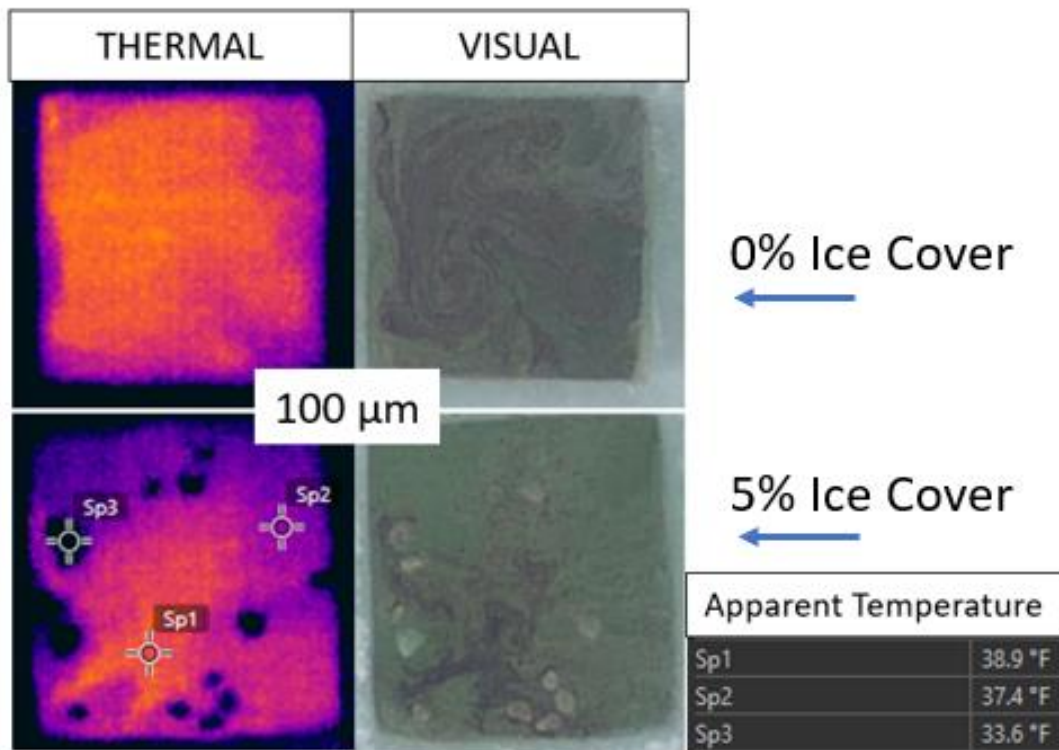


Figure 45. Thermal contrast detected when oil thickness reached 100 μm .

These experiments indicated that the minimum thickness threshold for detection of oil with thermal imagery in Arctic conditions is between 50 μm and 100 μm . (The same sensor was used to detect seep oil in waters off Santa Barbara, CA, but had a detection limit of 5 μm .)

The multispectral sensor did not detect oil at 10 μm (Figure 46) with the false composite (left = NIR, RedEdge, Red) or true color RGB (right). Using independent channels and multiple combinations of false composites did not help.



UAS Characterization of Oil in Ice – Volume I: Laboratory Results

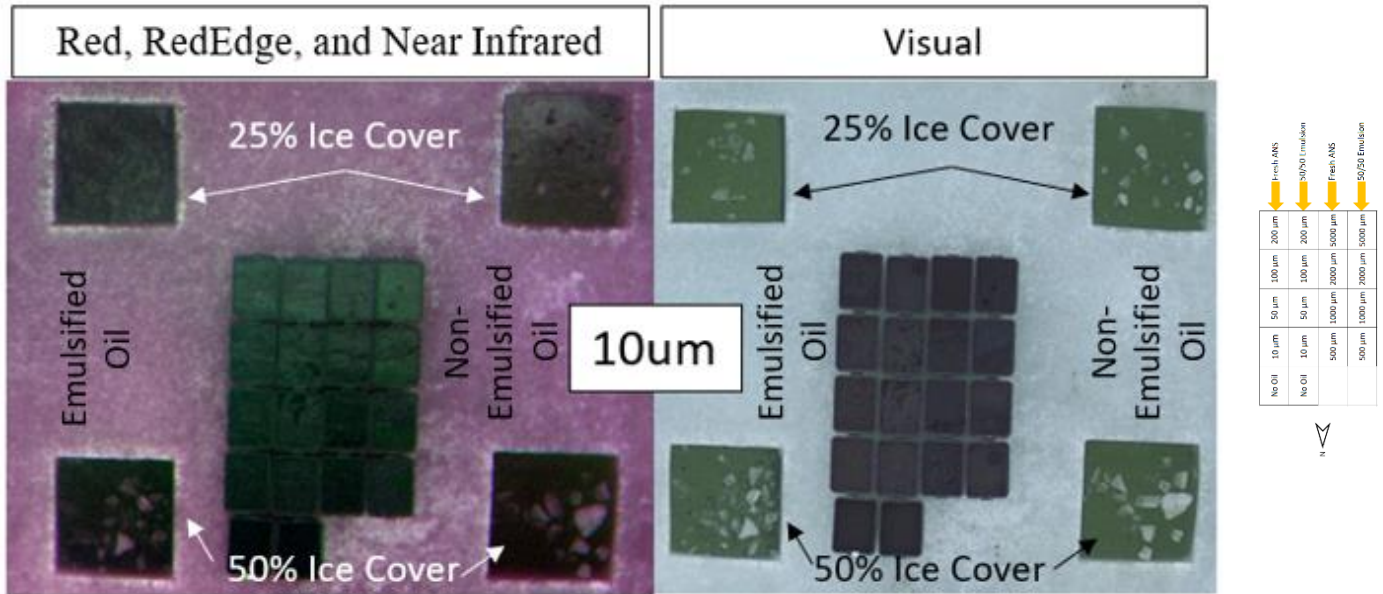


Figure 46. Multispectral analysis of 10 μm of oil. There was no detection of change at this level.

At the 50 μm and 25% ice thickness, oil and emulsions were detected using the multispectral imagery. Figure 47 shows a multispectral false composite (left) and the true color RGB (right).

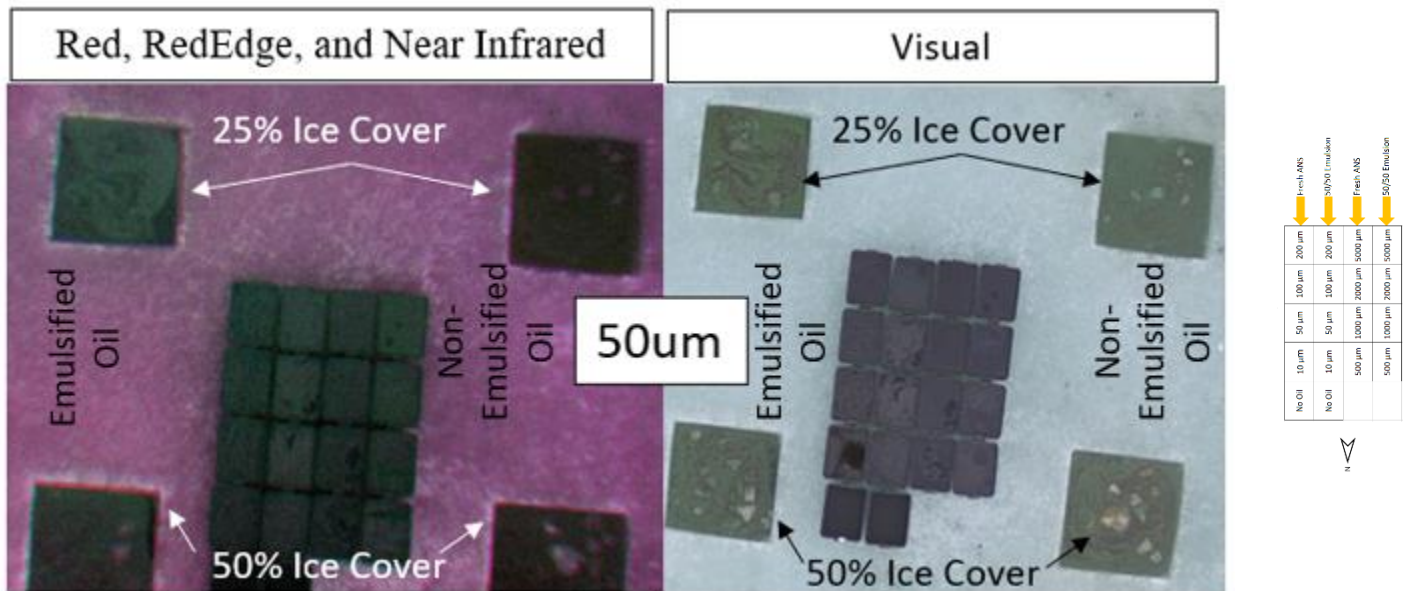


Figure 47. Multispectral analysis of 50 μm of oil.

Figure 48 shows a closer view of the 50 μm and 25% ice cover. The pattern of the emulsified oil inside the square (left) matched the oil distribution seen on the visual imagery (right).



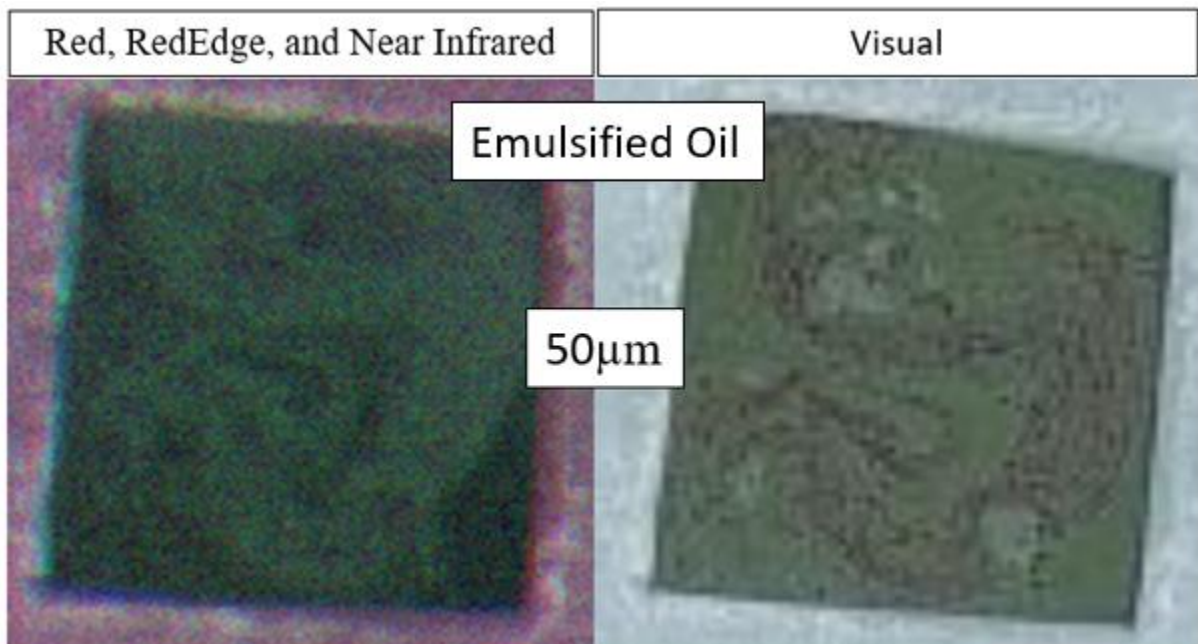


Figure 48. Higher magnification of the 25% ice cover using multispectral image of 50 μm emulsified oil.

The minimum detection level for thermal occurs between 50 μm and 100 μm for non-emulsified oil, while the minimum detection level for the multispectral imagery occurs between 10 μm and 50 μm for emulsified oil.

3.3 Algorithms for Oil Thickness Detection

The objective of the proposed algorithms is to estimate the thickness of the oil when ice is present based on the ambient conditions when the imagery is collected. The apparent temperature of the oil will decrease as the water temperature decreases and the percent ice cover increases.

3.3.1 Algorithms for Oil Thickness in Cold Water without Ice

Equation 1 on page 33 of this report describes the logarithmic relationship between apparent temperature and thickness of the oil in the totes (Figure 33). Although the temperature of the water in the totes was warmer than the water inside the 1m x 1m squares, a similar relationship is expected in which the temperature of the background water would have to be adjusted to *in situ* condition (Equation 1 for the totes has ambient water = 9.94 $^{\circ}\text{C}$ (49.9 $^{\circ}\text{F}$)). The time lapse experiments (Figure 37) confirmed that in ice-free water, oil thickness detection changes as the illumination conditions change.

3.3.2 Algorithms for Oil Thickness in Cold Water with Ice

When ice is present in water containing oil, it must be masked off (i.e., removed) from the images to estimate the percent of the area it covers. This can be achieved by using the high contrast of the multispectral imagery or “thresholding” the apparent temperatures of the thermal data. After the ice coverage is estimated, the apparent temperatures based on the thermal analysis are compared to the ice cover. For example, Figure 49 was produced by measuring the apparent temperature of the 1m x 1m squares



UAS Characterization of Oil in Ice – Volume I: Laboratory Results

and comparing emulsified vs non-emulsified oil for each of the ice covered areas during Flight 8 at 1409 hours. The best fit for these two lines is a quadratic equation.

$$A_T = -1.766 \ln (IC) + 27.658 \text{ (Equation 2)}$$

where A_T is the apparent temperature variation, and IC is the percent ice cover. The thermal radiation from emulsified oil was slightly higher than from non-emulsified oil. This effect was also observed for the multispectral imagery and time lapse analysis for apparent temperatures of the totes (e.g., 500 μm through a 24-hour period; Figure 37).

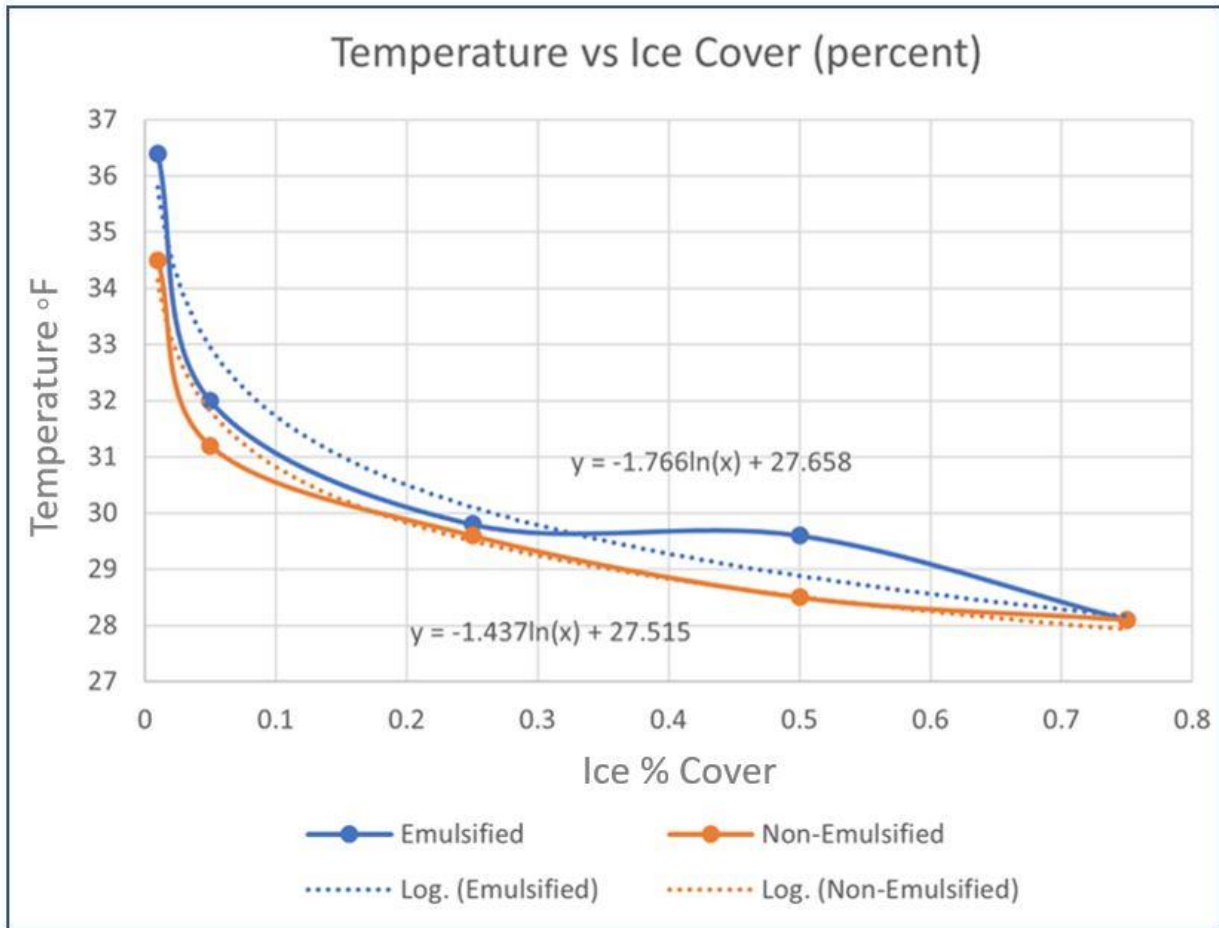


Figure 49. Apparent temperature variability due to ice cover.

Equation 2 indicates how much the apparent temperature of the oil will decrease as the percentage of ice increases. As the ice cover increases, the difference in the apparent temperatures between the non-emulsified and emulsified oil decreases. The equation can be used to adjust apparent temperatures obtained from thermal imagery to assess oil thickness in ice infested waters. Note: The efficacy of this relationship has not been tested in the field and would need to be developed as a function of the environmental conditions.

Figure 50 shows data from Flight 8 with a 1,000 μm slick applied to each square. The amount of ice cover in each square varied from 25% to 75% for emulsified and non-emulsified oil. The panel on the left shows



UAS Characterization of Oil in Ice – Volume I: Laboratory Results

the actual visual image of the oil distribution on the squares. The corresponding thermal (FLIR) image is also shown in the right panel. The apparent temperatures from every pixel in the image for the 25%, 50%, and 75% ice cover of emulsified and non-emulsified oil are shown in the left and right columns of squares in the thermal image. Figure 51 shows the results of adjusting the apparent temperatures obtained from the thermal images using Equation 2. The adjusted apparent temperature values are then transformed to thicknesses (μm) using a logarithmic relationship which is derived from the totes containing known amounts of oil without ice (See Equation 3 below).

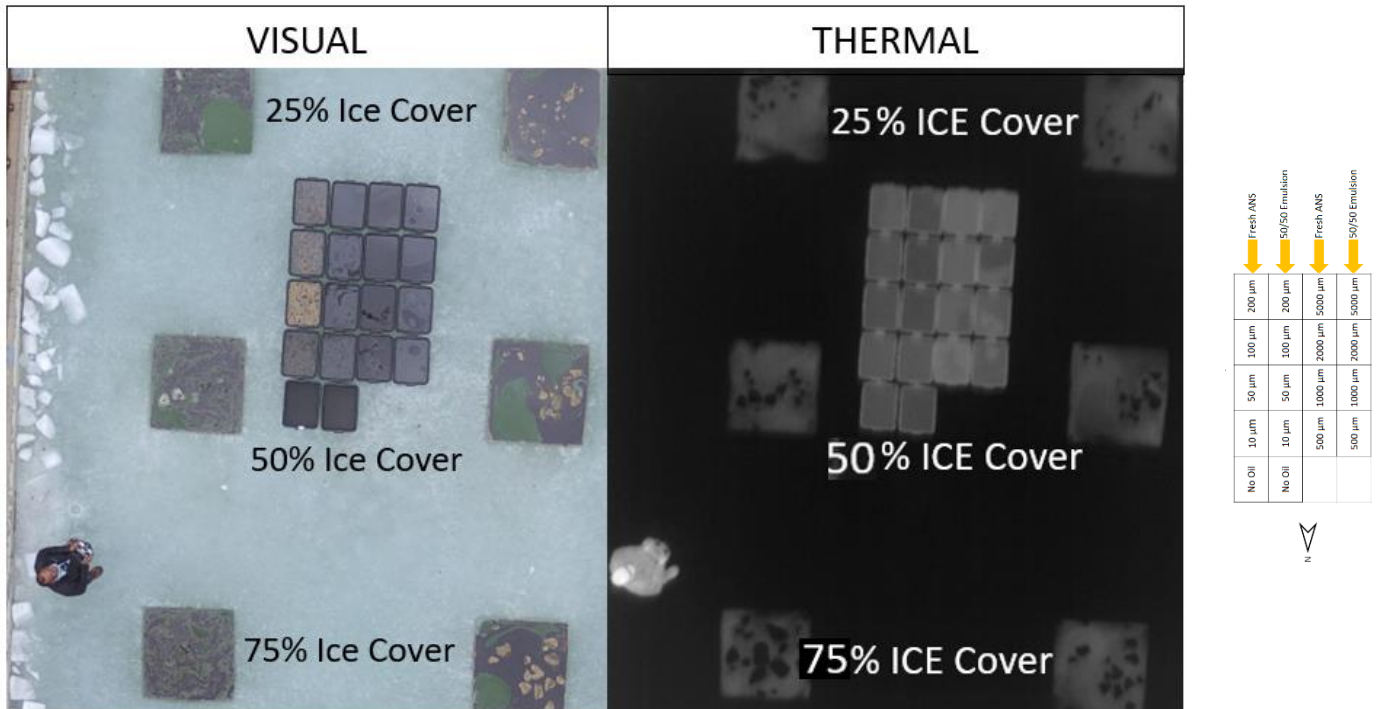


Figure 50. Oil distribution on squares during Flight 8 with 1,000 μm of emulsified (left) and non-emulsified (right) columns of oil for each panel.



UAS Characterization of Oil in Ice – Volume I: Laboratory Results

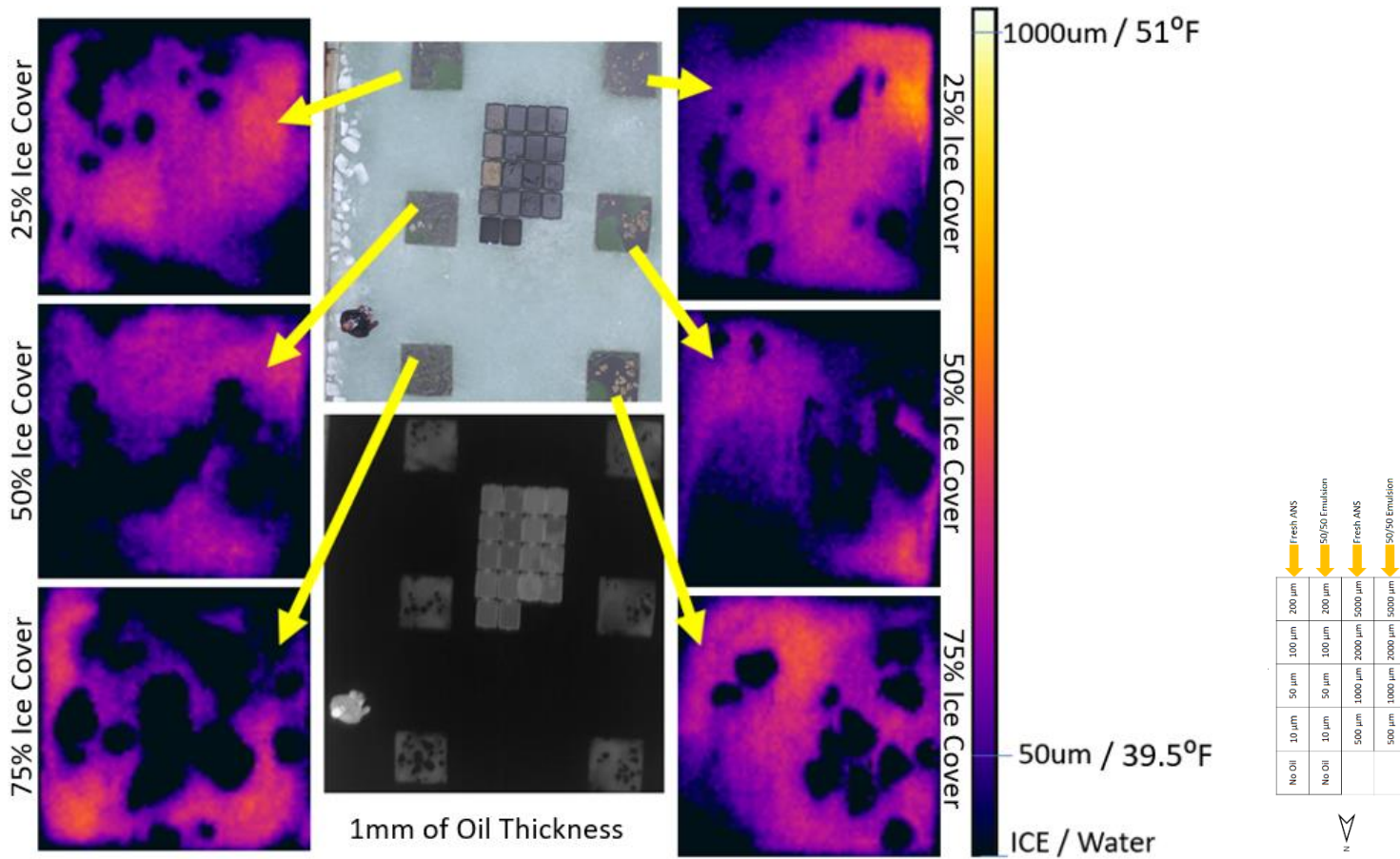


Figure 51. Apparent temperatures derived from thermal images of squares containing 1,000 mL of emulsified (left) and non-emulsified (right) oil with different ice cover from Flight 8.

Figure 52 shows the relationship between the apparent temperatures derived from the thermal imagery taken at 13.7 m (45 ft) of the totes and the known oil thicknesses. In this case, using the apparent temperatures obtained at the highest and warmest contrast, the best fit equation is obtained from a logarithmic function:

$$A_T = 1.4002 \ln(O_T) + 48.749 \text{ (Equation 3)}$$

where A_T is the apparent temperature ($^{\circ}\text{F}$), and O_T is the oil thickness (μm).



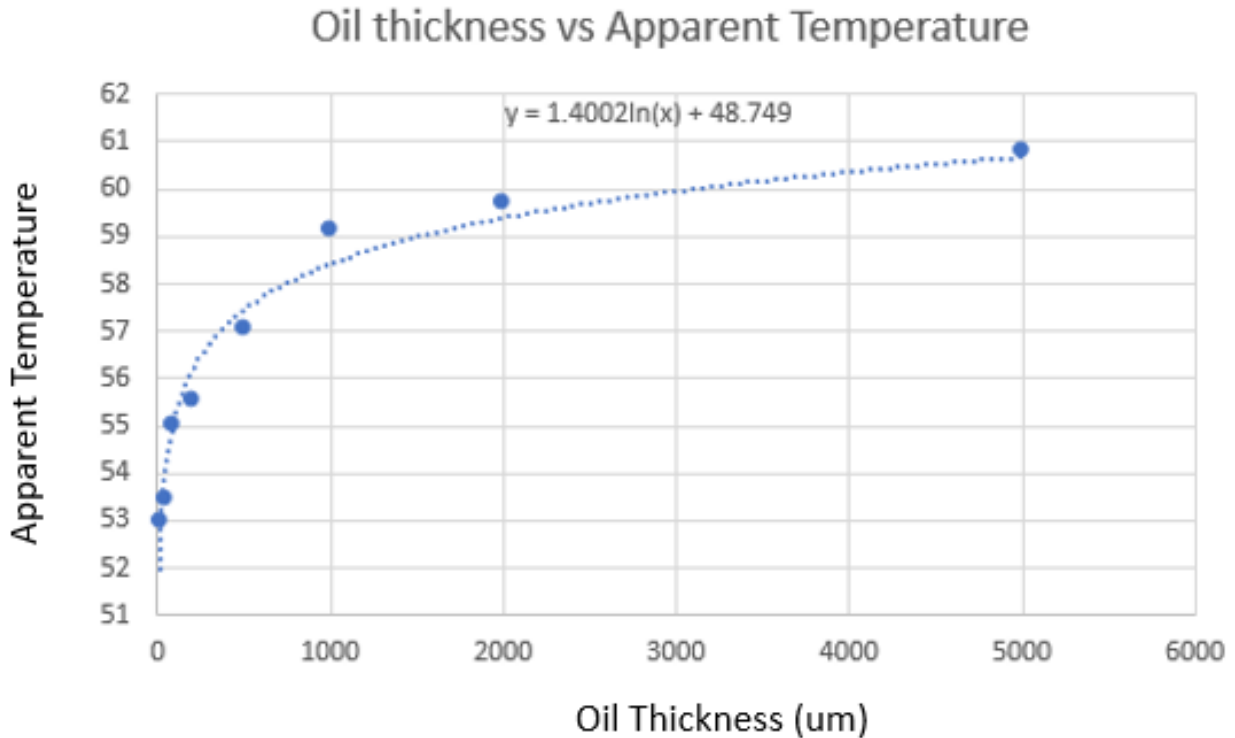


Figure 52. Apparent temperature vs. oil thickness using Flight 8 data and the oil totes of known thickness.

The inflection point on this curve occurs between 500 μm and 1,000 μm. This indicates that at some thickness greater than 500 μm and less than 1,000 μm, the apparent temperature changes will diminish and thickness will be harder to predict (particularly during conditions when the maximum contrast is not obtained). For example, thermal sensor saturation and the limited radiometric resolution means that only a 1 °F increase in apparent temperature occurs as thickness increases from 2,000 μm to 5,000 μm. Therefore, using Equation 3 for oil thicknesses < 748 μm (the inflection point) will be the most reliable. It is important to note, these changes occurred in apparent temperatures of the oil in the totes with no ice. The presence of ice will diminish the thermal contrast and mean that thickness estimates will be less reliable.

The experiments clearly show that the apparent temperature range obtained by thermal imagery depends on the target under study (i.e., ice, oil, and/or water) and the environmental conditions. For example, the plot shown on Figure 49 displays a range of temperatures for identification of ice cover (28 °F to 37 °F), while Figure 50 shows a range of temperatures for oil thickness differentiation between 53 °F to 61 °F. This means that each time a mission is conducted in the Arctic, the thermal imagery (i.e., apparent temperatures) must be calibrated on-site to obtain reliable oil thickness data.

3.4 Ice Cover Adjustment Effect on Oil Thickness and Volume Estimates

The relationship between apparent temperature and ice cover (Figure 49), which is the foundation of Equation 2, had to be independently validated. The project team was able to do this using the 1m x 1m squares that contained known oil and ice volumes.

Figure 53 shows a thermal linear gray scale of the temperatures during Flight 8, in which 1,000 mL of oil were added to the squares with different amounts of ice cover.



UAS Characterization of Oil in Ice – Volume I: Laboratory Results

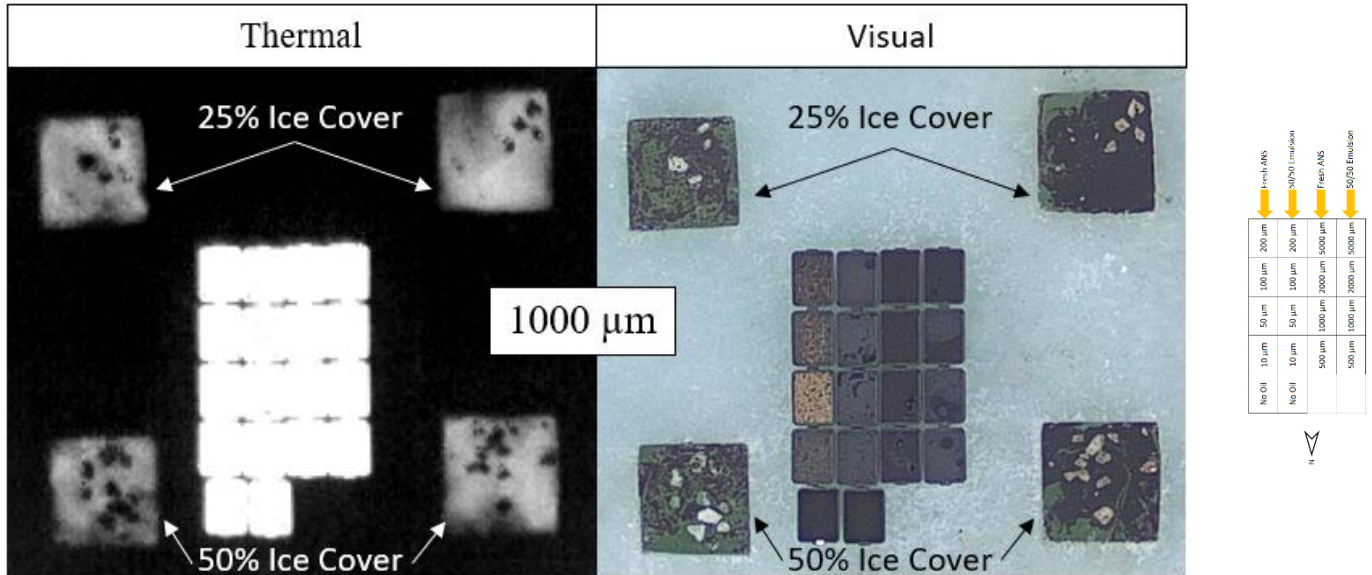


Figure 53. Linear temperature of the ice and oiled surface in the GRF tank. Totes with no ice show much warmer than 1m x 1m squares with oil and ice.

Using threshold-based image segmentation, all pixels that corresponded to the ice on the thermal image were masked off (i.e., all pixels that looked black on the thermal image corresponded to ice). Figure 54 shows the ice sheet on the tank and the ice inside the squares as pure black. All the ice pixels were assigned a value of ‘zero’ oil. The yellow box corresponds to 25% ice cover and 1,000 mL of ANS non-emulsified oil.

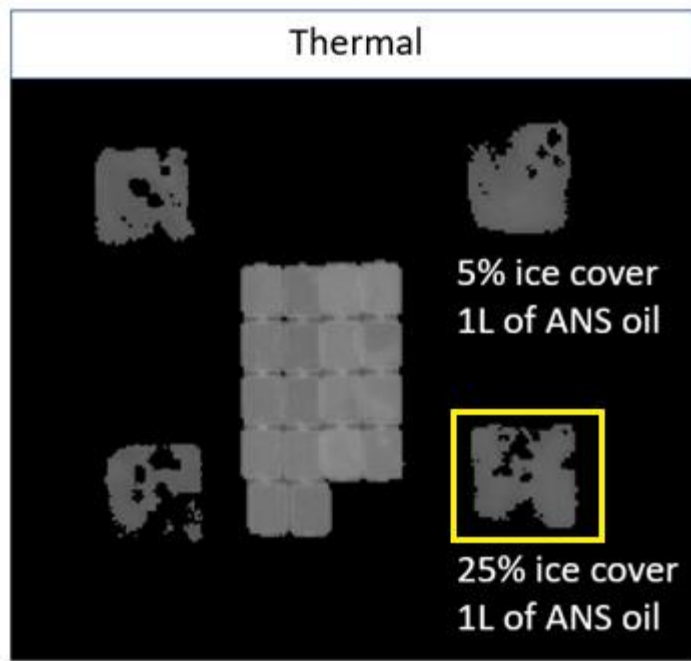


Figure 54. Ice pixels converted to zero, the yellow square shows the 1m x 1m cell with 25% ice cover and 1,000 μm.



UAS Characterization of Oil in Ice – Volume I: Laboratory Results

The actual ice cover in the yellow box observed using the thermal imagery was 16% (instead of 25%). This percentage was obtained by counting the number of pixels equal to zero (i.e., ice) and dividing that by the total pixels contained inside the 1m x 1m square. There are several potential reasons for this difference in ice cover (16% instead of 25%), the most probably of which is that smaller patches of ice melted relatively quickly (as observed by the CRREL staff). Thus, by the time UAS data was collected, a smaller portion of the initial area was ice covered.

Figure 55 shows the apparent temperatures of the individual pixels that the thermal imagery obtained inside the yellow 1m x 1m square. The reflected apparent temperature of the ice was 4.17 °C (39.5 °F). Anything below that apparent temperature was considered non-oiled ice and was masked and assigned a value of zero. The high resolution thermal image taken at 13.7 m (45 ft) of the 1m x 1m square shown in Figure 55 measured 39 pixels x 39 pixels, which is equivalent to 2.56 cm x 2.56 cm [6.55 cm²] per pixel.

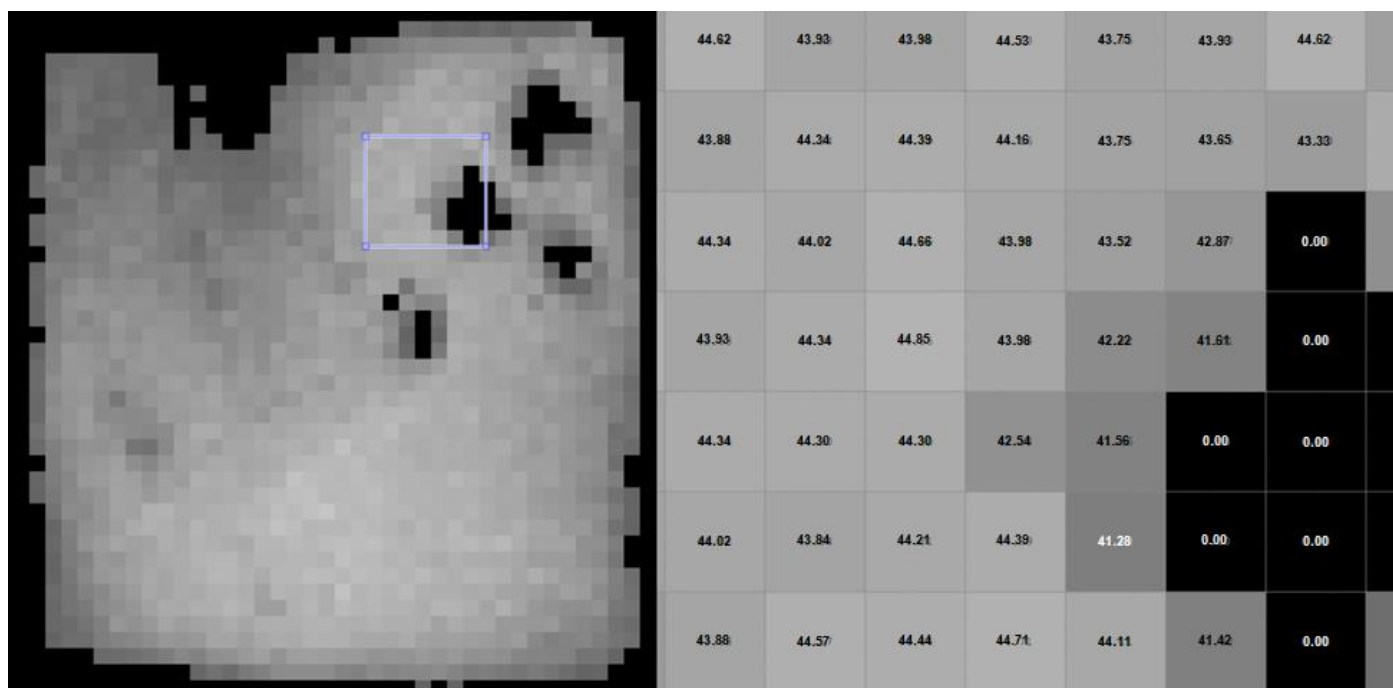


Figure 55. Apparent temperatures inside each pixel in the 1m x 1m square with 25% ice cover and 1,000 μm. The right panel is a magnified image of the light blue square on the left panel to show the apparent temperature values.

The volume of oil per pixel was calculated by dividing the 1,000 mL of oil added to the square by the normalized apparent temperatures, where the minimum apparent temperature of an oiled pixel was 4.17 °C (39.5 °F). All units were converted to meters, square meters, and cubic meters for thickness, area, and volume, respectively. Figure 56 shows the equivalent oil volumes in cubic meters per pixel.



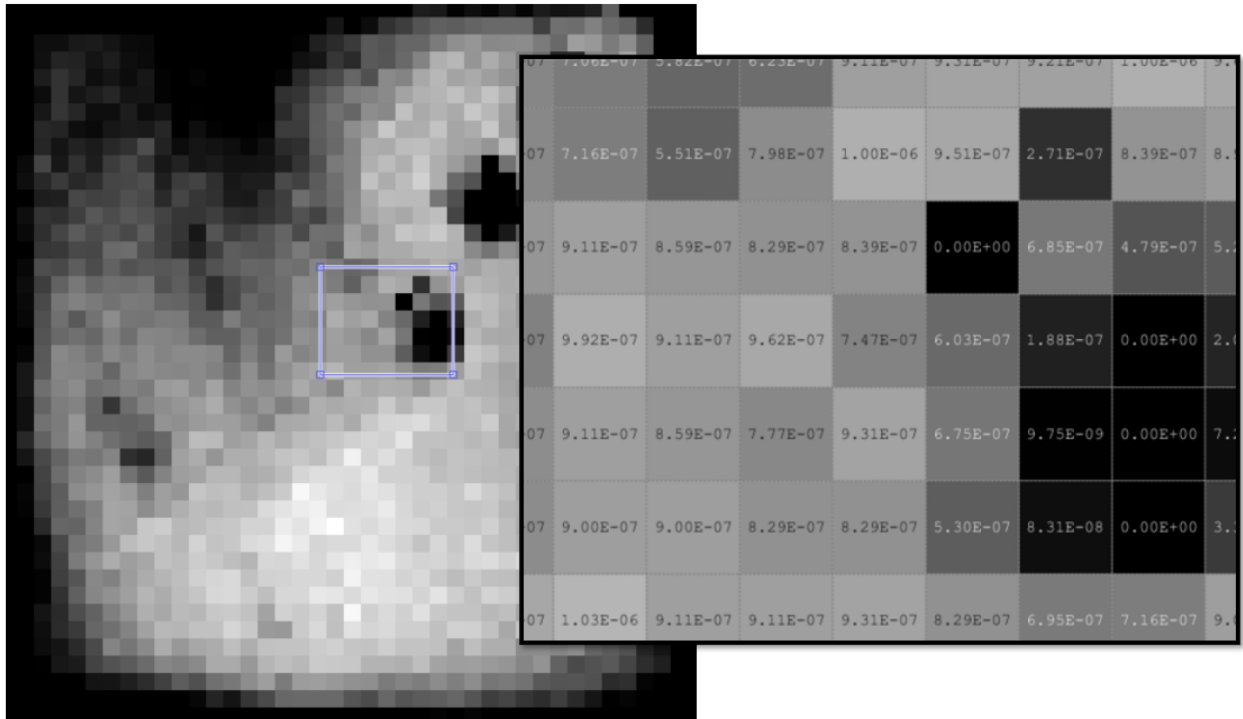
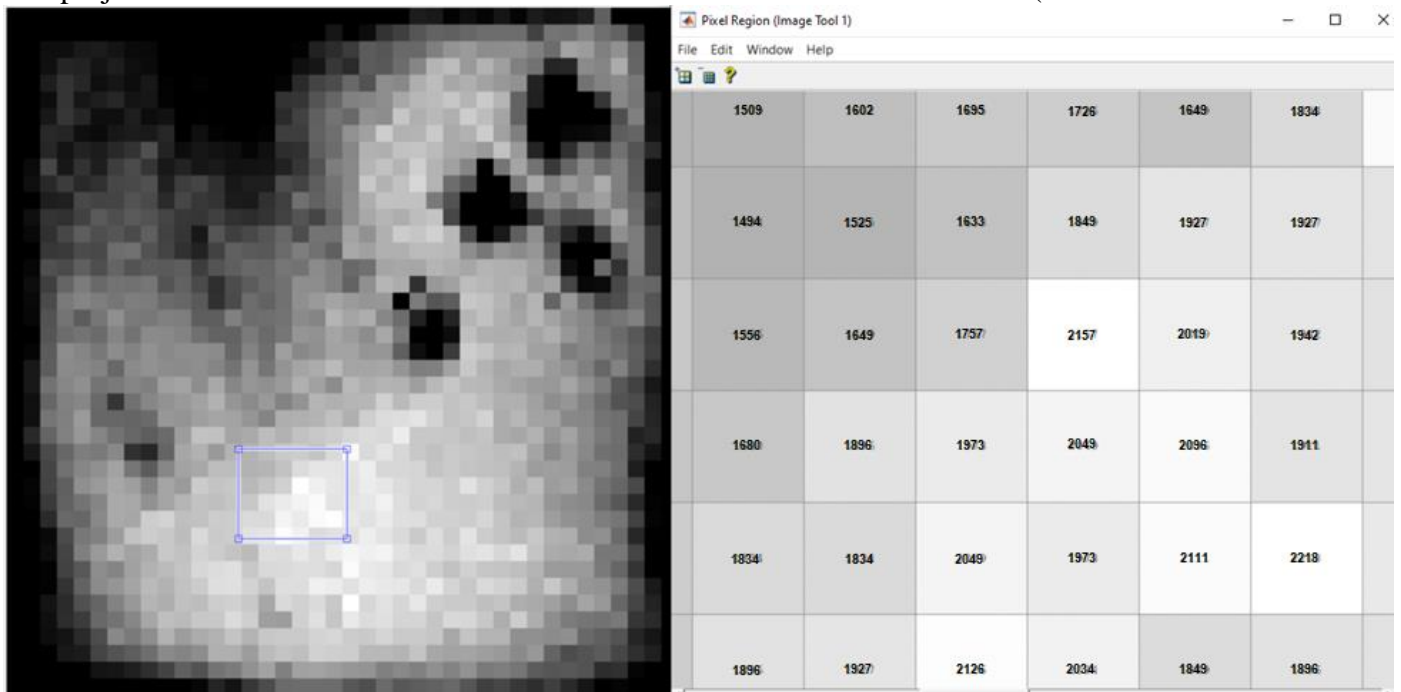


Figure 56. The volume of oil per thermal image pixel (m^3). The right panel is a magnified image of the light blue square on the left panel to show the apparent temperature values.

The project team was able to obtain the estimated distribution of oil thicknesses (



UAS Characterization of Oil in Ice – Volume I: Laboratory Results

Figure 57) by dividing the oil volumes by the area per pixel (e.g., 6.55 cm² per pixel). The thicknesses ranged from zero (area occupied by ice) to 2,157 μm (more than double the hypothetical 1,000 μm uniformly distributed layer).

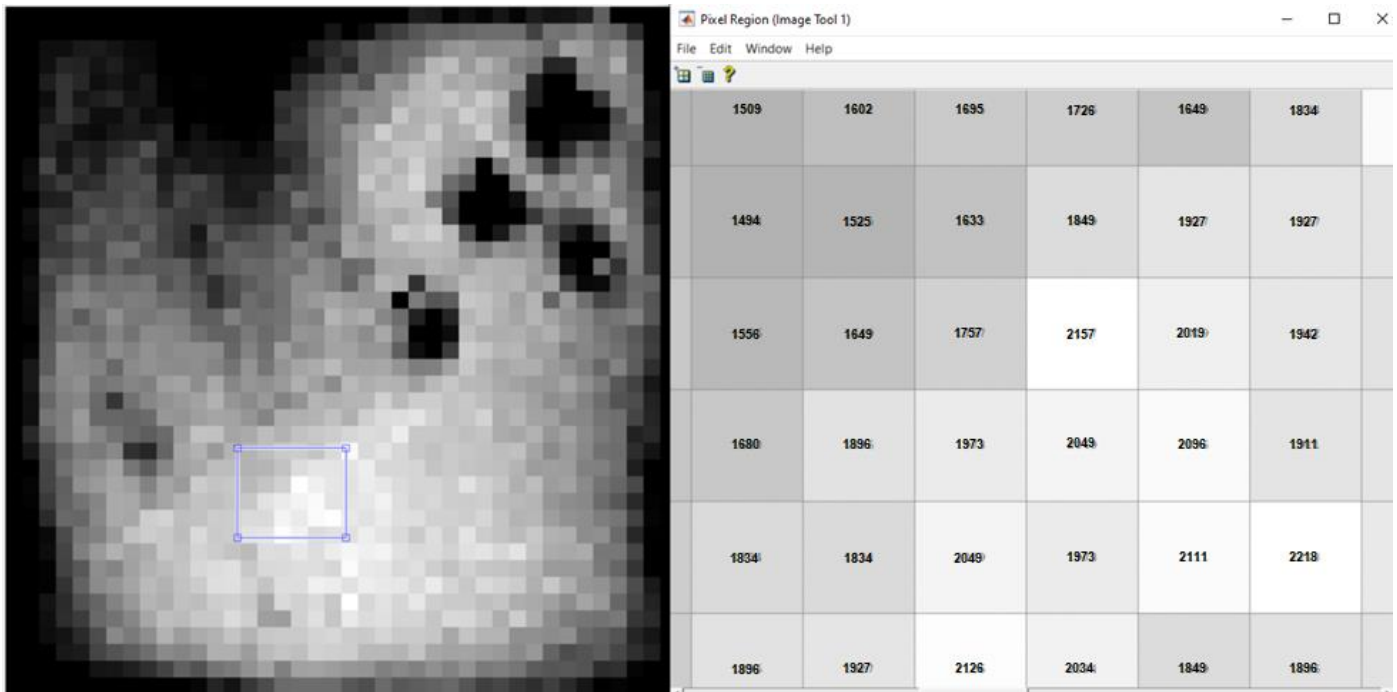


Figure 57. Estimated thickness of oil per pixel; maximum thickness calculated was 2,157 μm. The right panel is a magnified image of the light blue square on the left panel to show the apparent temperature values.

Using 16% in Equation 2, which the thermal imagery determined was the actual ice coverage inside the yellow box in Figure 54, the project team calculated the adjusted apparent temperatures and the oil volumes in the 1m x 1m square. Figure 58 shows the thicknesses resulting from this correction. The estimated volume of oil present using this approach was 940 mL instead of 1,000 mL of oil with a maximum thickness of 2,157 μm. If the apparent temperature of this square had not been adjusted by the actual percent ice cover, the calculations would have shown 830 mL of oil (17% error). The histogram inset in Figure 58 shows many pixels had thicknesses above 1,500 μm.



UAS Characterization of Oil in Ice – Volume I: Laboratory Results

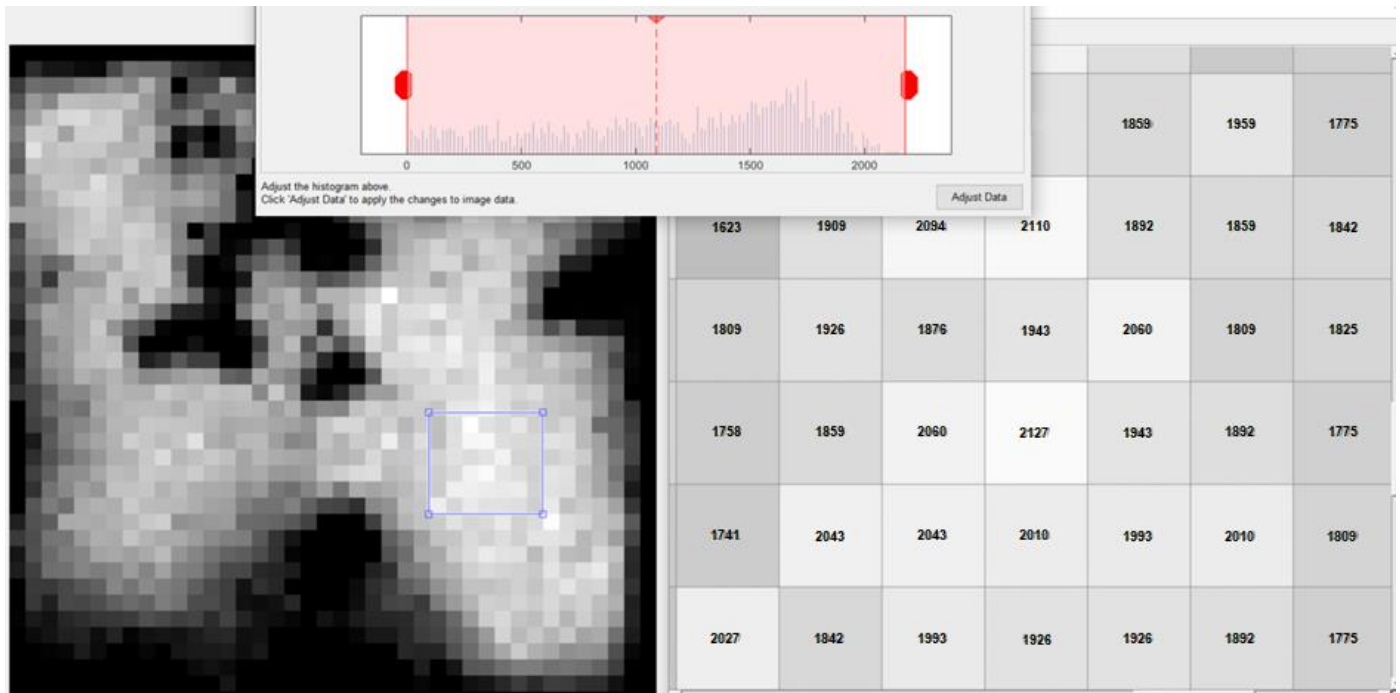


Figure 58. Adjusted thicknesses (μm) per pixel on a 1m x 1m square using the actual 16% ice coverage. Histogram inset in shows the frequency distribution of the oil thicknesses.

The same process was repeated for cells with 50% and 75% of ice cover, and the actual ice cover was determined to be 39% and 63%, respectively (Figure 59). The difference in percent ice cover is again attributed to ice melt. The oil volumes for squares these squares were 890 mL and 840 mL (11% error and 16% error), respectively.



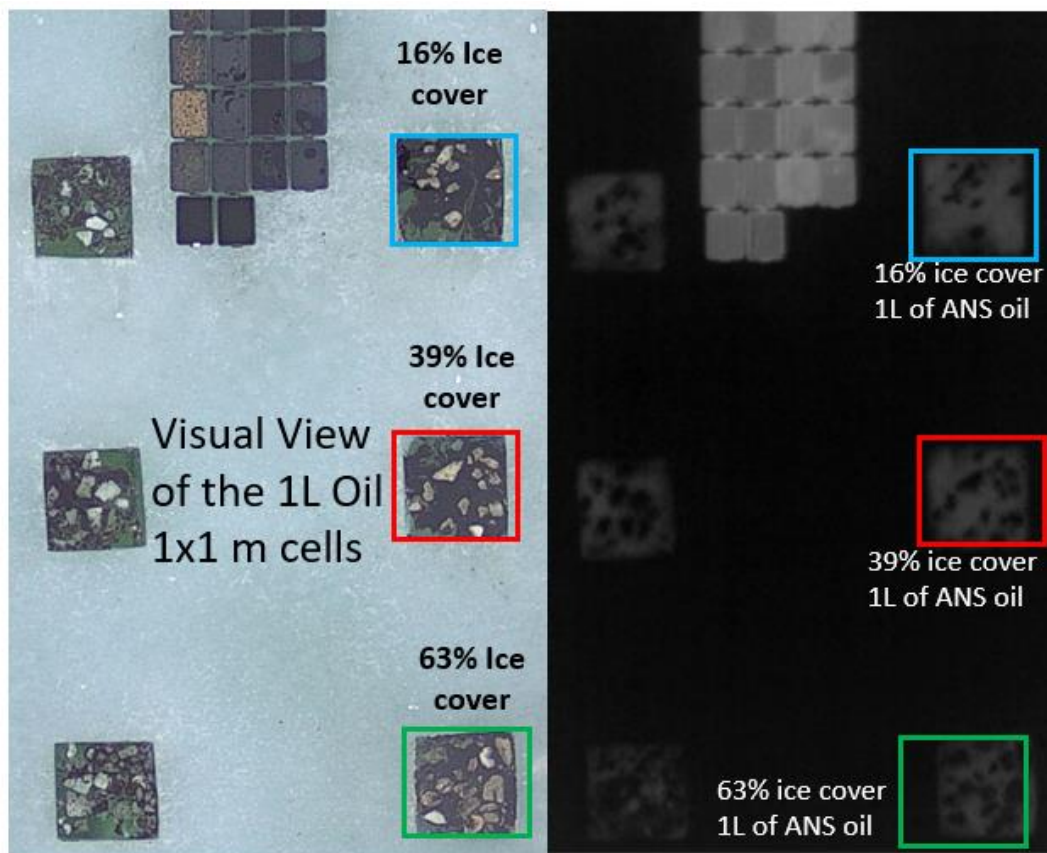


Figure 59. Cells with 50% and 75% of ice cover where ice melted to 39% and 63%, respectively.

Overall, these evaluations showed that as ice cover increases, the uncertainty in the oil volume calculation increases. This could be caused by the difficulty in adjusting the apparent temperatures properly due to the unevenness in oil spreading. A thermal sensor with a higher spectral and spatial resolution would be needed to provide more accurate results.

3.5 Workflow and Data Processing to Obtain Oil Thickness

Data acquisition for remote sensing depends on available resources and what weather conditions are present at the time of data collection. The workflow is independent of sensor or platform type and consists of a review of the imagery collected along with ancillary data (e.g., weather conditions). Visual inspection of the imagery is required to identify/discern the elements (e.g., oil thickness) present. A trained user is needed to apply classification to produce maps of the detected elements/features.

Based on the CRREL experiments, a workflow for the data processing for oil detection experiments in Arctic waters should be executed as follows:

1. Obtain background and synchronous visual, multispectral, and thermal imagery over points of reference (e.g., totes with known oil thickness, non-oily water/ice) to use for calibration.

UAS Characterization of Oil in Ice – Volume I: Laboratory Results

2. Obtain synchronous visual, multispectral, and thermal imagery of the oil on ice/water at a higher elevation to locate and initially resolve oil from ice and water. Once oil is detected, fly at a lower altitude to obtain higher resolution imagery without disturbing the oil's surface.
3. Record and note ambient conditions including surface apparent temperature and illumination conditions.
4. If possible, obtain *in situ* physical measurements of multiple targets (i.e., oil thicknesses) at the same time imagery is collected to use for calibration/validation.
5. Identify and differentiate emulsified vs. non-emulsified oil from multispectral imagery.
6. Plot apparent temperature data from imagery of reference (known) oil thicknesses to derive the relationship (based on the ambient conditions) for thermal radiation of the targets (e.g., Equation 3). For reference, this should also include collection of data on areas where oil is not present.
7. If no ice present, transform apparent temperature values to thickness values using the equation derived in Step 6.
8. If ice is present:
 - a. Use image processing software (e.g., Matlab, Arcmap, IDL) to apply a supervised image classification routine to segment the areas of:
 1. Water with no oil (clean water)
 2. Clean ice
 3. Areas where oil is deposited directly above the ice
 4. Non-emulsified oil on water
 5. Emulsified oil on water
 - b. Determine the percent of ice cover.
 - c. Apply the adjustment of apparent temperatures for the different areas depending on the ice cover percentages (e.g., Equation 2).
 - d. Transform apparent temperature values to thickness values (e.g., Equation 3).

There is a parallel process to this workflow with the geo-projection of orthomosaics. The GPS data is assigned to each of the UAS images given the spatial resolution at a given altitude. This parallel process is necessary so all data generated can be properly projected and mapped.

The workflow can be also applied to UAS imagery that does not include *in situ* physical thickness measurements using visual thickness estimates obtained from the Bonn Agreement Oil Appearance Code.

3.6 Methods for Calculating Oil Thickness in Ice Infested Waters

There are two methods for determining oil thickness based on apparent temperatures from thermal sensors mounted on a UAS. These methods use different approaches to convert the thermal sensor's apparent



UAS Characterization of Oil in Ice – Volume I: Laboratory Results

temperatures into thicknesses. Method 1 uses *in situ* measurements of the oil thickness (e.g., using a tube sampler deployed from a vessel) to convert the apparent temperature readings to oil thickness. Method 2 bases the conversion on apparent temperatures obtained from totes containing known amounts of oil of different thickness.

3.6.1 Method 1. Using *In Situ* Physical Measurements of Oil Thickness

The project team tested Method 1 using thermal imagery for the pixels on a 1m x 1m square while a tube sampler collected physical thickness measurements simultaneously (Figure 60). CRREL staff added 500 mL of oil to the square with approximately 50% ice cover while it was snowing. Figure 60 shows the project team collecting measurements of oil thickness with a tube sampler while thermal images were taken on the A-Frame every minute. After each measurement, CRREL staff added in additional oil for the next thickness target. Once new oil was added, the water/ice/oil was manually moved inside the 1m x 1m square for a few of minutes to distribute the oil on the surface as evenly as possible. The project team collected the physical thickness measurements shortly after the oil was added coinciding with the period when the thermal imagery was poor.



Figure 60. Top view from the multispectral imaging of a 1m x 1m square while the project team collected physical measurements of multiple thicknesses.

There were multiple factors affecting the imaging of the oil in ice. Illumination conditions were the main constraint to image collection. Additionally, snow, cloud cover, and rain can reduce the thermal reflectivity of the target, which decreases the capacity of the thermal and multispectral sensors to obtain a clear signal. Turbulence created by waves, currents, or swells could generate the thermal mixing of ice/water/oil and



UAS Characterization of Oil in Ice – Volume I: Laboratory Results

challenge the masking of the ice and the thickness classification. This effect is illustrated by the movement of floating ice and oil at the beginning of each oil addition to the 1m x 1m square. When that occurred, the thermal sensor had difficulty differentiating between oil/ice/water because the movement of ice would produce a more continuous exchange in the apparent temperature of the oil and water. This observation suggests that constant movement of the ice/oil/water in the field may compromise the usefulness of thermal imagery to estimate oil unless the *in situ* conditions are relatively stable.

The thickness measurement and thermal image collection for the thickness target of 1,000 μm was much better. The oil and ice were imaged with much better contrast and the *in situ* thickness measurement was not collected immediately after the oil was added. Figure 61 illustrates how the thickness of each pixel and total volume was calculated after the ice/water/oil was static. The thermal camera was setup on the top of the A-Frame ~6 m above the surface of the square, the pixel resolution inside the square was 3 mm.

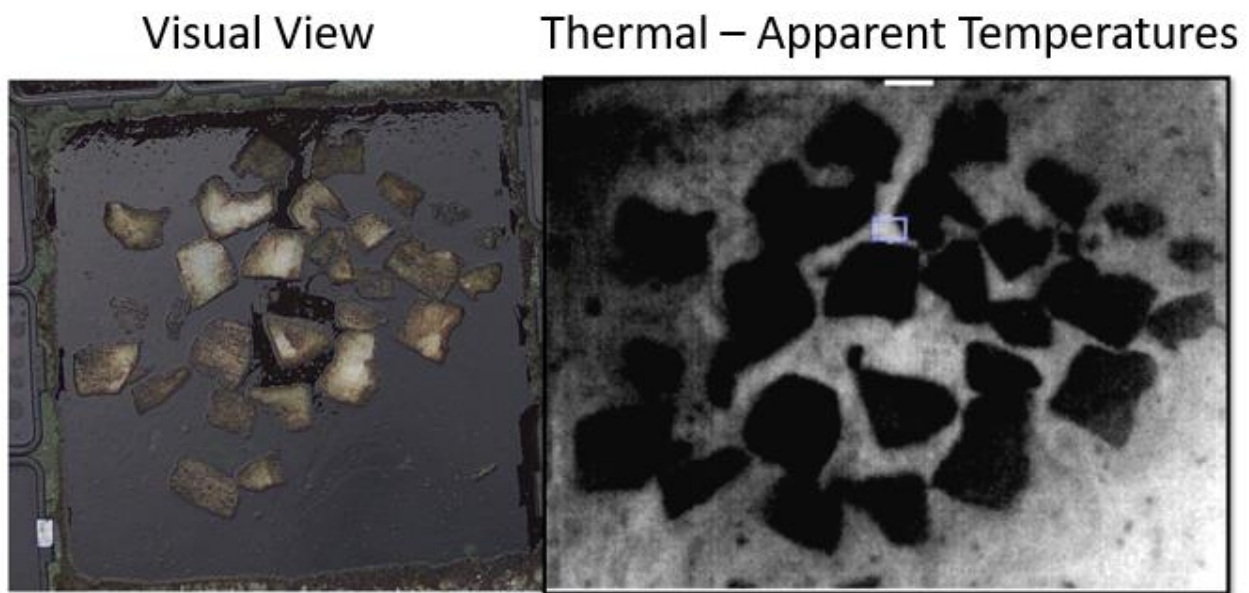


Figure 61. 1m x 1m square with 1,000 μm of oil on ice and 50% ice cover.

All the ice pixels were assigned a value of zero apparent temperature for oil thickness calculations. The area of the square where the tube sample was collected is shown in a yellow circle on Figure 62. The physical measurement collected showed an approximate thickness of 1,120 μm . All of the apparent temperatures from each pixel of the thermal image were converted (calibrated) to thickness. This approximates a one-point calibration.



UAS Characterization of Oil in Ice – Volume I: Laboratory Results



Figure 62. Pixels on the thermal image that have been converted to thickness values.

After the apparent temperatures were converted to thicknesses, the total volume of oil on the square was calculated to be 1,134 mL, an error of approximately 13%. This error could be caused by several factors, including the uneven distribution of the oil and the associated variable surface thickness across the square, and imprecision of the tube sampler. Further work is required to characterize the error/uncertainty behavior of the thermal thickness estimates under various environmental conditions.

Figure 63 shows the color map of thicknesses. It shows a maximum thickness of 2,500 μm in the bottom right corner of the square. This effect was observed in previous field work and in the CRREL experiments indicating that thicker oil accumulates in corners, as it will against natural barriers.



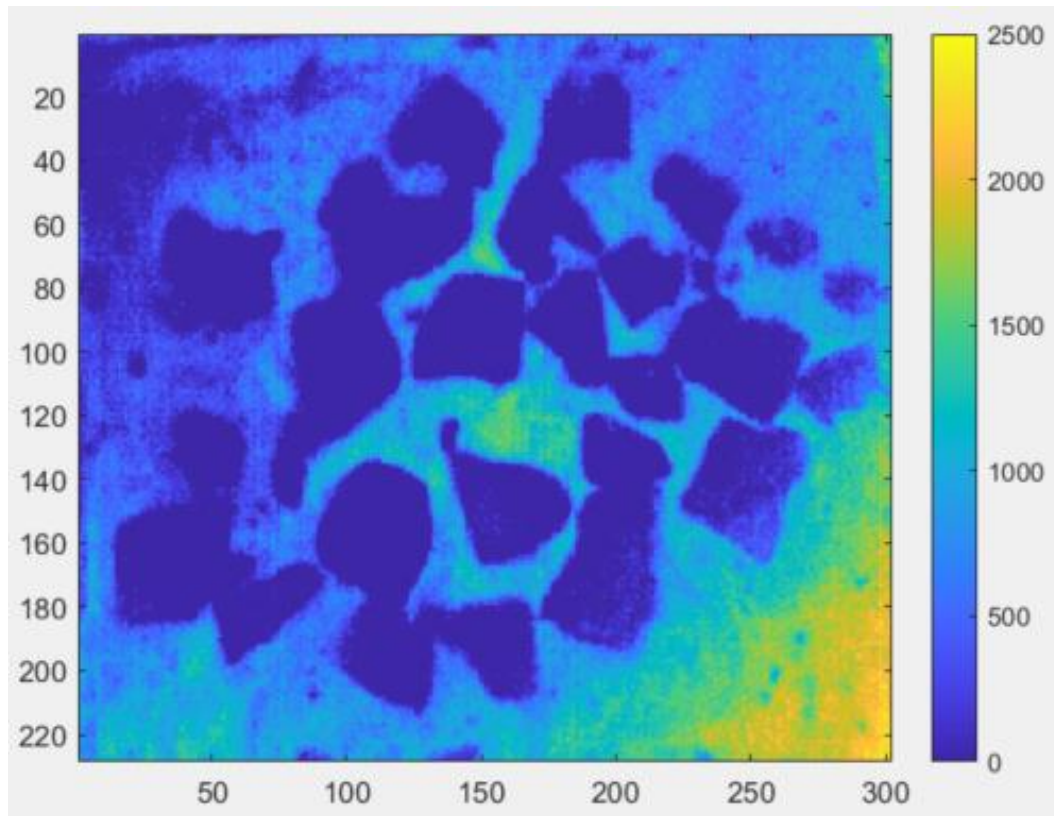


Figure 63. Oil thickness (color scale in micrometers) inside the iced square.

The project team applied the same process for the 1m x 1m square for 5,000 mL of oil (Figure 64). In this case the ice and oil were static, and a high contrast was observed on the thermal image. A physical measurement of oil thickness was collected from the area shown as a yellow circle in the right panel of Figure 64. The estimated thickness from the tube sampler was 3,400 μm . The physical measurement from this sample was the first measurement less than the targeted thickness (5,000 μm). It appears that the amount of oil was sufficient to fill the entire area of the square evenly. This can be seen on the thermal image where there is an evenly distributed layer of oil across the square compared to those with lower volumes.

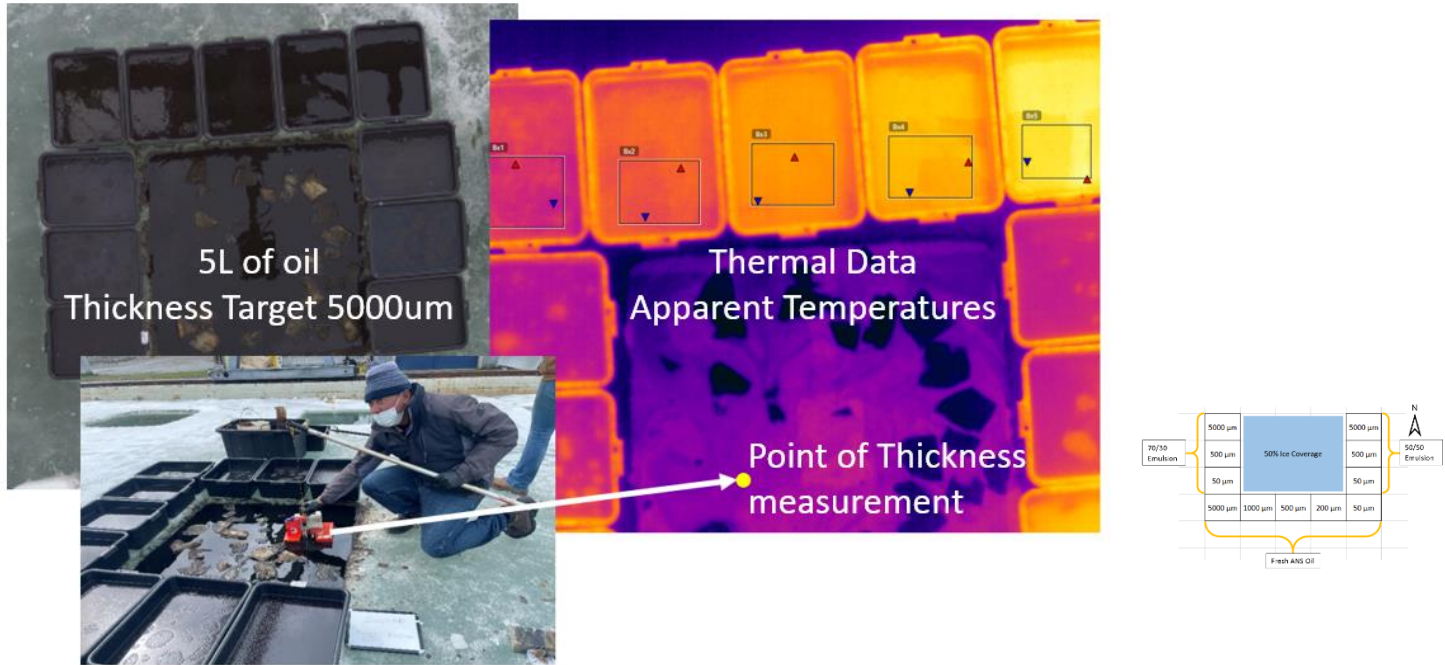


Figure 64. Physical measurement of oil thickness for the oil/ice thickness algorithm.

When the 3,400 μm thickness was used to calibrate the rest of the pixels, the calculated volume of 3,128 mL underestimated the oil volume by 1,872 mL (38%). This underestimate could be related to the radiometric limitation of the sensor for thicknesses $>1,000 \mu\text{m}$. Additionally, the uneven distribution of the oil could contribute to this underestimate. Furthermore, overcast conditions limited the contrast of the thermal image. This highlights the importance of characterizing effect of environmental conditions.

3.6.2 Method 2. Using Totes Containing Known Oil Thicknesses

The project team collected thermal images over the 1m x 1m square containing 1 L of non-emulsified oil and five totes. The five totes contained oil with thicknesses of 100 μm , 200 μm , 500 μm , 1,000 μm , and 5,000 μm and were arranged around the periphery of the 1m x 1m square (Figure 65) using the A-Frame experimental set up. For comparison, the same thicknesses were used for Method 1.

UAS Characterization of Oil in Ice – Volume I: Laboratory Results

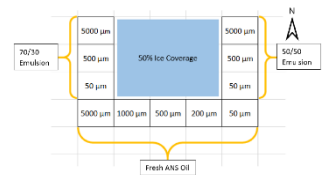
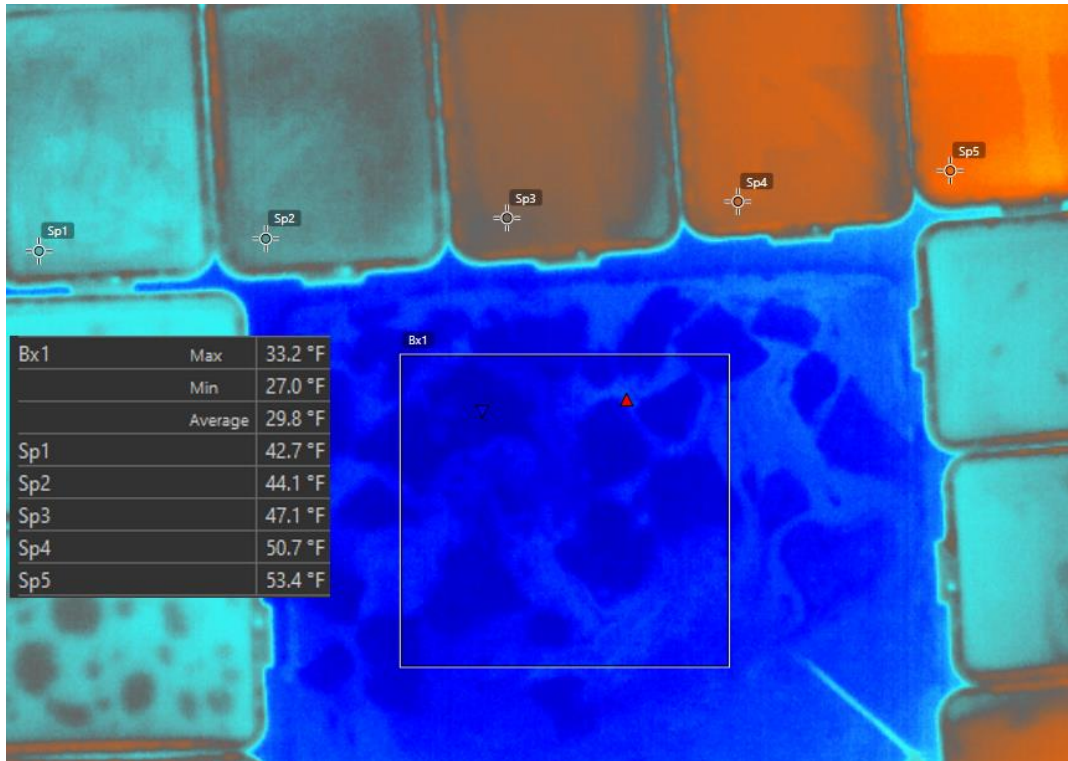


Figure 65. Thermal image over a 1m x 1m square with 1,000 mL of oil. Non-emulsified oil with layers of thicknesses of 100 μm, 200 μm, 500 μm, 1,000 μm, and 5,000 μm (respectively from left to right).

Figure 66 shows a plot of the apparent temperatures and known thicknesses from the totes. The best fit is given by the logarithmic equation:

$$A_T = 2.90 \ln(O_T) + 29.3 \text{ (Equation 4)}$$

where O_T is the oil thickness, and A_T is the apparent temperature captured by the thermal sensor.



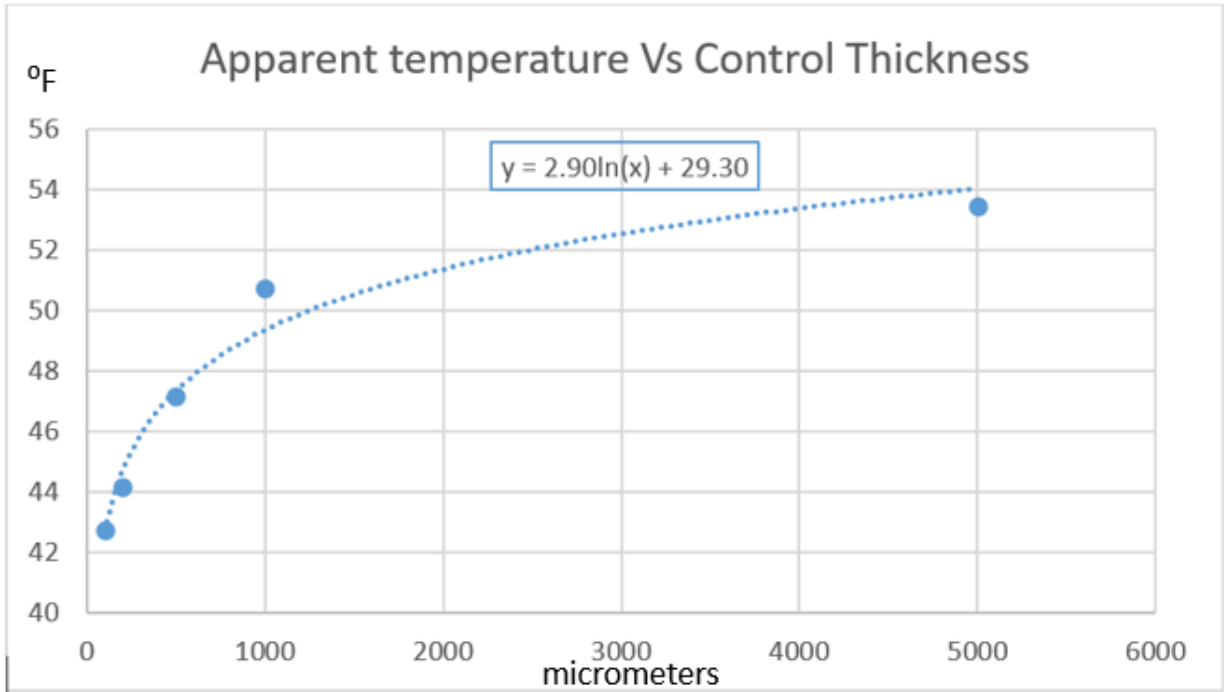


Figure 66. Apparent temperature change vs thickness.

The apparent temperatures of the pixels on the thermal image were adjusted for the percent ice cover (50%) using Equation 2. Then, Equation 4 is used to transform all the ice cover-adjusted apparent temperatures to thicknesses (Figure 67).

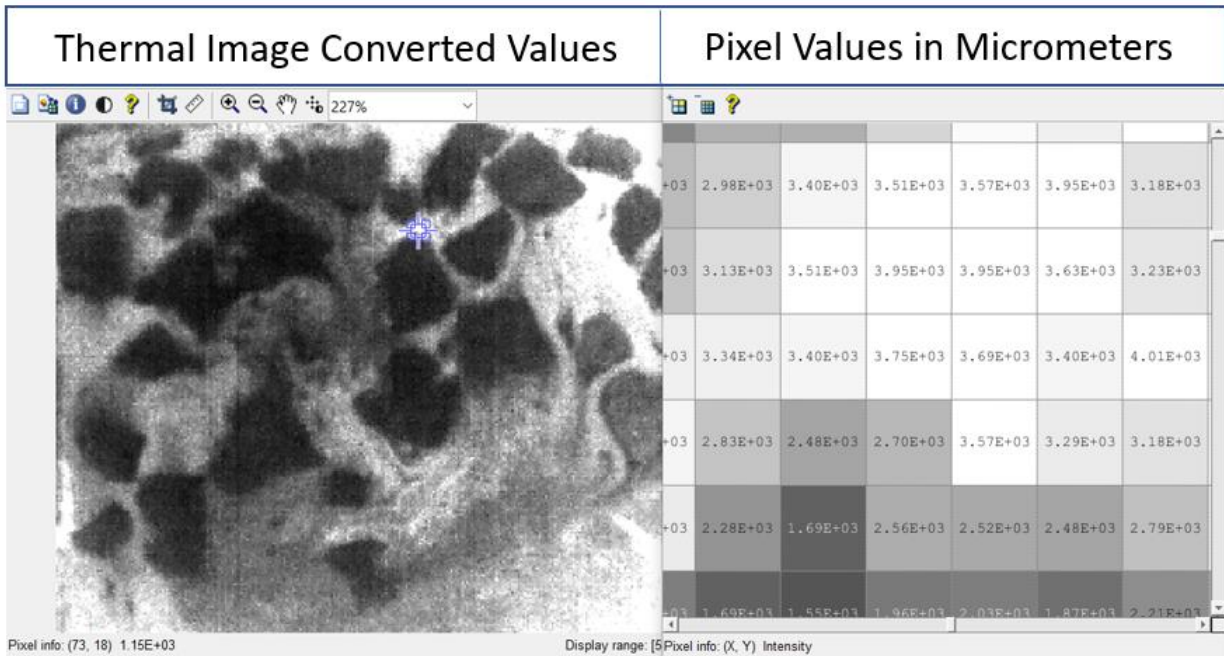


Figure 67. Calculated oil thicknesses from adjusted values of apparent temperatures.

UAS Characterization of Oil in Ice – Volume I: Laboratory Results

Using calibration Method 2, the oil thickness was estimated as 3,900 μm (for the nominal 1,000 μm thickness) on the same area where the Method 1 calculated thicknesses of 1,120 μm . The total volume of oil inside the 1m x 1m square was computed by multiplying the thickness of the oil by the area of the pixels (equivalent to 3.1 mm x 3.1 mm). The resulting volume in Method 2 was 2,721 mL as compared to the 940 mL estimated from Method 1.

The thicknesses of oil in this example are in the domain where the sensor starts to be saturated (e.g., \sim 1,000 μm). Additionally, the curve (fitting equation) was obtained by a limited number of known thickness samples also adds to the error of this method.

3.6.3 Comparing Methods 1 and 2

Multispectral and thermal sensors were able to identify floating oil in ice infested water in these experiments, and determined minimum and maximum detection limits. However, deriving volumes of floating oil directly from remote sensing of oil in ice is very difficult. The uncertainties in volume estimates in ice-water increase drastically compared to volume estimates in temperate waters because of the: 1) heterogeneity of the oil on the surface, 2) variability of the environmental conditions, and 3) limits of sensors to detect variances in oil thicknesses particularly at maximum detection limits when ice is present.

Relying on a physical measurement of the oil thickness produces results with less uncertainty than attempting to resolve thicknesses and volumes solely by using remote sensing without *in situ* measurements. Comparing the two methods for 1,000 mL of oil, Method 1 (in which an *in situ* physical thickness measurement was used to extrapolate thickness measurements) had an overestimate of 134 mL, while Method 2 had an overestimate of 1,721 mL.

While the task of discerning between thin oil and actionable oil could be relatively easily achieved, the task for quantifying oil volumes remains challenging and requires further work.

4 CONCLUSIONS

The project team developed an approach to extract oil thickness information from multispectral and thermal imagery for ice covered water. The conclusions of this experiment can be summarized as follows:

- Multispectral imagery can be used to distinguish between emulsified and non-emulsified oil.

This can be achieved with high altitude remote sensing and may include satellites and aircraft that can cover large areas. While the distinction of oil emulsions and floating crude oil is relatively straightforward in cases where *in situ* sampling is permissible, hazardous conditions, such as those in the Arctic, may not allow for protracted sampling campaigns. The ability to detect the presence of oil emulsions will help an FOSC assess the recoverability of oil.

- The use of NIR, RedEdge, and Red bands from the multispectral offers the best false composite combination of channels to distinguish between emulsified and non-emulsified oil.

Post experiment data analysis revealed this was the most suitable band combination to detect floating oil emulsions in icy waters and distinguish them from non-emulsified oil. It may be possible to develop



UAS Characterization of Oil in Ice – Volume I: Laboratory Results

automated systems dedicated to the monitoring of oil spills using these multispectral channels for satellite, aerial platforms, and UAS.

- Visual, infrared, and multispectral imagery can be used to discern between clean ice and ice covered by oil.

It is challenging to estimate the thermal equilibrium between ice, water, and oil based on a single linear thermal measurement. However, through the incorporation of measurements from diverse sensors (e.g., multispectral) and in-situ measurements, these challenges may be mitigated. The ability to detect whether icy environments have been contaminated by oil is important to the sensitive Arctic environments.

- Non-linear thermal imagery can be used to segmentate and classify areas of ice cover.

Images collected from aerial and satellite platforms are time-sensitive during oil spills, when results are needed in 6 to 12-hour planning cycles. The inability to rapidly map and mask ice cover may result in inaccurate thickness “heat” maps, especially when implementing automatic or semi-automatic classification (which is standard practice). Improved workflow processing for thermal imagery may be rapid enough to improve the accuracy of such “heat” maps.

- Thermal measurements of various oil thicknesses under specific illumination conditions can be used to derive thicknesses of oil in different ice cover areas.

While challenging, the use of thermal sensors for oil spills in icy waters may be extended beyond the mapping of oil extent by using specific “calibration” methods to estimate oil thicknesses using thermal sensors. This important development will improve estimates of oil recoverability, aid in the coordination of response operations (e.g., *in situ* burning), and damage assessment for Arctic spills.

- At night, emulsified oil reflects infrared energy more strongly than non-emulsified oil.

The water molecules in the 30:70 emulsion produced a radiation inversion (i.e., thermal crossover) as the sunlight disappeared at night indicating that highly emulsified oil may have a greater apparent temperature when light levels are low to non-existent in the Arctic.

The CRREL experiments provide a foundation for further research to implement a processing routine that can be applied to field operations to detect different densities of ice cover and oil thickness for a range of environmental conditions. The findings will be applicable not only for UAS platforms, but for any platform capable of holding these sensors (e.g., higher altitude airplanes, satellites).

4.1 Differences between Analyzing Oil Thickness in Temperate and Arctic Waters

Comparison of the CRREL results to those obtained using 1m x 1m squares at Ohmsett illustrates some of the differences in oil thickness determination between temperate and Arctic conditions. Figure 68 shows an aerial view of 1m x 1m squares at Ohmsett (2018) and CRREL (2021). At Ohmsett, the variables were the thickness of oil (either emulsified or non-emulsified), while at CRREL they were the thickness of the oil and percent ice cover. To better simulate *in situ* conditions offshore, Ohmsett staff placed a black tarp on the bottom of the tank. At CRREL, the natural reflectance of ice is white, resulting in intense brightness (even though the water inside the tank was turbid). The reflectance from the ice was intense enough at CRREL to



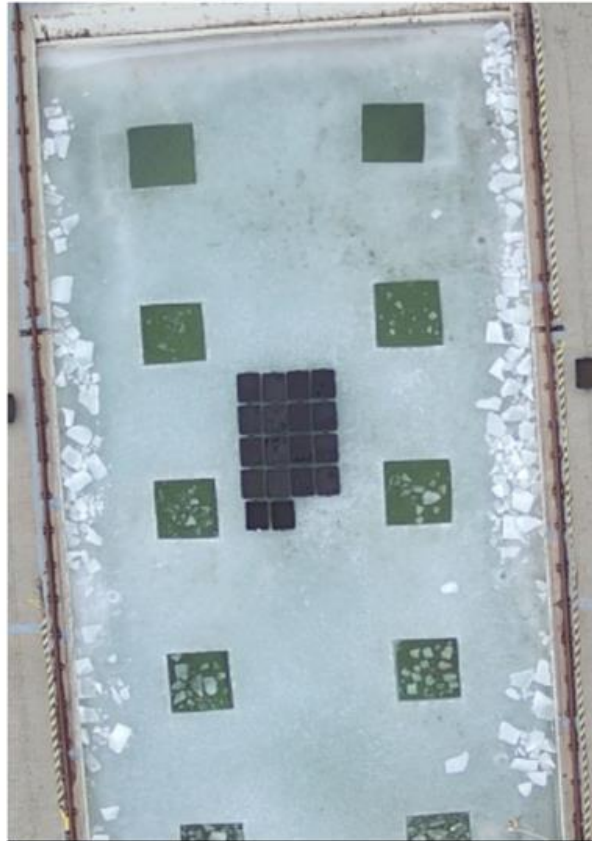
UAS Characterization of Oil in Ice – Volume I: Laboratory Results

brighten the water inside the squares. In order to overcome the complication of the bright ice reflectivity, an array of totes containing known oil thicknesses of emulsified and non-emulsified oil was placed nearby.

1x1m squares at Ohmsett



1x1m squares at CRREL



	200 μ m	200 μ m	5000 μ m	5000 μ m
fresh ANS	↓		↓	↓
50/50 Emulsion		↓		
Fresh ANS			↓	↓
50/50 Emulsion				↓

10 μ m 50 μ m 100 μ m 200 μ m 500 μ m 1000 μ m 2000 μ m

No Oil	10 μ m	50 μ m	100 μ m	200 μ m	500 μ m	1000 μ m	2000 μ m	5000 μ m
No Oil	↓	↓	↓	↓	↓	↓	↓	↓

N ↙

Figure 68. Ohmsett (left) vs. CRREL (right) experimental conditions.

When no ice is present, the full scale of the thermal contrast (radiometric resolution) of the water and the oil can be used to distinguish variation in apparent temperatures, and thus, oil thickness. When ice is present, the thermal sensor has another element to image, and the high ice reflectance negatively impacts the multispectral imaging. Additionally, in Arctic conditions, the scale of apparent temperatures reduces the ability to distinguish between oil and water (oil thickness). For example, if water is 10 °C (50 °F) and oil, warmed by the sun, is 11.1 °C (52 °F), the full radiometric resolution of the camera distinguishes a range of 1.1 °C (2 °F) in apparent temperature. If ice covers 50% of the area (≤ 0 °C (32 °F)), it will cool the water and the oil, reducing the temperature difference between them. In addition, the full radiometric resolution will cover a wider span of temperatures (i.e., ice to water and oil), leaving a much lower range to resolve differences of apparent temperature between the oil and water. Hence, there is a smaller range of apparent temperatures with which to identify changes in oil thickness.

UAS and Commercially Off-the-Shelf (COTS) multispectral sensors are readily available, although severe Arctic conditions may necessitate use of heated hulls and other cold temperature adaptations to flying. Through these experiments, we have demonstrated that this technology has the potential to acquire quality data in icy waters to: 1) detect the presence of oil, 2) estimate the surface oil thickness, and 3) discern between non-emulsified and emulsified oil. This work shows the potential for COTS-accessible tools and



technology to be further developed and improved for transitioning into more routine operations in the years to come.

While the project demonstrated the potential of the remote sensing technology for oil characterization in ice infested waters, one of the limitations in applying these results immediately to the Arctic is the limited conditions tested. Different thicknesses of oil, different configurations of ice covered areas, different types of oil, multiple combinations of oil and emulsions, and actual sea state conditions (e.g., wind, wave action, turbulence), as well as the study of false positives are necessary. Moving beyond the controlled test setting of CRREL and into the field will further advance our understanding of the capabilities and limitations of these sensors. For example, snow, illumination, ice type and extent, daily variation in temperature, ocean color, and wave type will likely affect sensor effectiveness.

Deploying a large UAS with all the integrated sensors was possible at CRREL. However, performing this operation in the field could be challenging with the current technology available. Logistical and technological barriers would have to be overcome. For example, landing and taking off with a large UAS (i.e., the Alta-X is 2.3 m (7.5 ft) wide) from a controlled area and a moving vessel under more extreme weather conditions is not the same. Other types of UAS, cameras and sensors need to be evaluated for their suitability in Arctic conditions. There are a number of options for UAS rigged with dual thermal and visual sensors. Operations without multispectral sensors may also be necessary depending on the size and type of drone used.

4.2 Use of UAS for Arctic Oil Spill Response

UAS is already used for oil spill response monitoring and assessment in temperate waters (e.g., shoreline, offshore) by Oil Spill Removal Organizations (OSROs) and researchers (Garcia-Pineda et al., 2019).

There are three types of UAS that could be used for the Arctic oil spill application: rotary copters, fixed wing, or Vertical Takeoff and Landing (VTOL). Each has unique characteristics that will impact technical aspects of its operation in Arctic conditions (e.g., flight time, coverage, maneuverability, practicality for deployment, retrieval from land and moving platforms). A rotary copter was used at CRREL. These platforms can hover/monitor in fixed positions, as the UAS pilot collects real-time views of targets. Currently, rotary copters are used almost exclusively during spills because fix-wings and VTOLs are difficult to use from moving vessels. However, rotary copters have a limited capacity to cover larger areas compared to a fixed wing and VTOLs, and carry small payloads which limits the weight of the sensors used. [N.B., The rotary copter used at CRREL was large and therefore is not suitable for takeoff and landing on moving platforms. It would be ideal for surveying from shorelines or land. Its flight time could reach 45 minutes if equipped with all of the sensors required (i.e., thermal, multispectral, visual, HD video real-time transmission). It offers the capacity to cover large areas providing the full catalog of data acquisition.]

The CRREL findings suggest that a mid-size rotary copter deployed from a U.S. Coast Guard vessel on the middle of the shoulder season (fall, when the ice is forming) could conduct tactical monitoring operations (high resolution digital video for real time tactical positioning) with a high definition (HD) visual camera. Information regarding detection of actionable oil to conduct response operations (e.g., booming, skimming, dispersants applications) would require an HD calibrated thermal sensor. A multispectral sensor would be needed for damage assessment in addition to thermal and visual sensors.



Further research should determine the effect of ice, oil, and water movement and mixing process on the analysis and interpretation of the sensor data. Future field work should explore flight altitude and maximum horizontal distance for flying. For example, flying at a maximum allowable altitude of 122 m (400 ft) during oil spills in temperate water produces a general spatial resolution of ~2 cm per sensor. Similarly, maximum horizontal flight distance will be limited by FAA rules related to Flying Within Line of Sight, which translates in an approximate radius of 1 mile using a large UAS like the Alta-X during daylight with good visibility. Smaller UAS will have a shorter range to comply with this requirement. This range may be even smaller in Arctic conditions (e.g., low light or visibility). At CRREL, the minimum detection limit of the thermal sensor for the oil was between 50 μm and 100 μm . The multispectral sensor started differentiating emulsions between 10 μm and 50 μm . Detection limits must be determined as a function of field conditions.

Balancing flight operations for area coverage, flight time, altitudes, transect distances, and spatial resolution is a cornerstone of planning flight missions depending on the objectives and must be evaluated in future work to develop the most efficient practices for tactical operations of sensor-equipped UAS during Arctic oil spills.

5 RECOMMENDATIONS

- Determine the effect of different types of oil products (e.g., diesel, Heavy Fuel Oils) and ice types (e.g., function of ice age/thickness, frazil ice, margin ice) on the estimate of oil thickness by visual, multispectral and thermal imagery.
- Conduct experiments in the Great Lakes and Alaska during ice season to further characterize uncertainties, strengths, and limitations with varying environmental parameters. Furthermore, determine calibration protocols, workflow, data processing and ascertain the usefulness of multispectral and thermal imaging under field conditions and in both freshwater and marine environments
- Future work is needed to determine how Arctic waters at different temperatures would affect the detection of oil. An experiment should be performed where water temperature is changed and monitored with smaller incremental changes in oil thickness to better understand detection on cold waters.
- Work with NOAA ORR to develop easy-to-interpret work products (e.g., oiling maps) that can be produced in response operational timeframes to support response, and in longer timeframes to support assessments.
- Determine method for estimating uncertainty bounds for oil thickness, so the NOAA SSC and FOSC will have this information during response.
- Work with NOAA ORR ERD to determine how UAS imagery can be processed and used in oil spill modeling to improve spill response.
- Determine the best method of calibration (e.g., one point vs. multipoint) of the thermal sensor for various Arctic spill conditions and data needs (e.g., skimmer deployment, Natural Resource Damage Assessment).
- Develop UAS specifications for cold weather operations in marine and freshwater (Great Lakes) environments.
- As this series of experiments was limited in ROV use, conduct further oil-in-ice detection experimentation using ROVs and autonomous underwater vehicles with various sensor capabilities.



5 REFERENCES CITED

Asanuma, I., Muneyama, K., & Sasaki, Y. (1986). Satellite thermal observation of oil slicks on the Persian Gulf. *Remote Sensing of Environment*, 19, 171–186.

Bonn Agreement Oil Appearance Code. Bonn Agreement Aerial Operations Handbook. Part 3, Annex A, The Bonn Agreement Oil Appearance Code. <https://www.bonnagreement.org/publications>

Cai, G., Wu, J., Xue, Y., Wan, W., & Huang, X. (2007). Oil spill detection from thermal anomaly using ASTER data in Yinggehai of Hainan, China. *IEEE International Geoscience Remote Sensing Symposium* (pp. 898–900) (Jul, 23-28, 2007, Barcelona)

Cross, A. M. (1992). Monitoring marine oil pollution using AVHRR data: Observations off the coast of Kuwait and Saudi Arabia during January 1991. *International Journal of Remote Sensing*, 13, 781–788.

Garcia-Pineda, O., Staples, G., Jones, C. E., Hu, C., Holt, B., Kourafalou, V., Graettinger, G., DiPinto, L., Ramirez, E., Streett, D., Cho, J., Swayze, G. A., Sun, S., Garcia, D., & Haces-Garcia, F. (2019). Classification of oil spill by thicknesses using multiple remote sensors. *Remote Sensing of Environment*, 236, [111421]. <https://doi.org/10.1016/j.rse.2019.111421>

Garcia, Oscar. (2019). System and Algorithm Development to Estimate Oil Thickness and Emulsification. (Bureau of Safety and Environmental Enforcement Oil Spill Response Research Project # E17PC00021). <https://www.bsee.gov/sites/bsee.gov/files/research-reports/1098aa.pdf>

Graettinger, G. (2018). Deepwater Horizon Lessons Learned Studies: Detection of Oil Thickness and Emulsion Mixtures using Remote Sensing Platforms. Report For US Department of the Interior Bureau of Safety and Environmental Enforcement (BSEE). <https://www.bsee.gov/sites/bsee.gov/files/research-reports//1079aa1.pdf>

Innman, A., Easson, G., Asper, V. L., & Diercks, A. R. (2010). The effectiveness of using MODIS products to map sea surface oil. *Proceedings of the IEEE, OCEANS 2010*, Seattle, WA.

Solberg, A. H. S. (2012). Remote sensing of ocean oil spill pollution. *Proceedings of the IEEE*. 100. (pp. 2931–2945).

Leifer, I; William J. Lehr, Debra Simecek-Beatty, Eliza Bradley, Roger Clark, Philip Dennison, Yongxiang Hu, Scott Matheson, Cathleen E. Jones, Benjamin Holt, Molly Reif, Dar A. Roberts, Jan Svejksky, Gregg Swayze, Jennifer Wozencraft. (2012). State of the art satellite and airborne marine oil spill remote sensing: Application to the BP Deepwater Horizon oil spill, *Remote Sensing of Environment*, Volume 124, 2012, Pages 185-209, ISSN 0034-4257, <https://doi.org/10.1016/j.rse.2012.03.024>. (<https://www.sciencedirect.com/science/article/pii/S0034425712001563>)

Lu, Y., W. Zhan, and C. Hu (2016). Detecting and quantifying oil slick thickness by thermal remote sensing: A ground-based experiment. *Remote Sensing of Environment*, 181, 207-217, doi:10.1016/j.rse.2016.04.007.



UAS Characterization of Oil in Ice – Volume I: Laboratory Results

National Research Council (2016). Responding to Oil Spills in the U.S. Arctic Marine Environment. <https://www.nap.edu/catalog/18625/responding-to-oil-spills-in-the-us-arctic-marine-environment>

NOAA-OWOIA (2016), Open Water Oil Identification Job Aid for Aerial Observation, <https://response.restoration.noaa.gov/oil-and-chemical-spills/oil-spills/resources/open-water-oil-identification-job-aid.html>

Panetta, P., Argo, T., Du, H., Donglai, Gong, L.N. Ferris, and Jeanna Kidwell. (2017) Development of acoustic methods to measure oil droplet size and slick thickness on ROV and AUV platforms, Report For US Department of the Interior Bureau of Safety and Environmental Enforcement (BSEE), 2017.

Salisbury, J., D'Aria, D., & Sabins, F. (1993). Thermal infrared remote sensing of crude oil slicks. Remote Sensing of Environment, 45, 225–231.

Tseng, W. Y., & Chiu, L. S. (1994). AVHRR observations of Persian Gulf oil spills. Geoscience and remote sensing symposium. Proc. IGARSS '94. 2. (pp. 779–782).

